JOURNAL OF GEOPHYSICAL RESEARCH, VOL. 107, NO. D21, 4586, doi:10.1029/2001JD001114, 2002

CHASER: A global chemical model of the troposphere
2. Model results and evaluation

Kengo Sudo and Masaaki Takahashi
Center for Climate System Research, University of Tokyo, Tokyo, Japan

Hajime Akimoto
Institute for Global Change Research, Kanagawa, Japan

Received 10 July 2001; revised 22 January 2002; accepted 8 February 2002; published 12 November 2002.

[1] We present results from a global three-dimensional chemical model for the troposphere, named Chemical AGCM for Study of Atmospheric Environment and Radiative Forcing (CHASER). This model has been developed to simulate the tropospheric photochemistry involving the O_3-HO_x-NO_x-CH_4-CO photochemical system and oxidation of nonmethane hydrocarbons (NMHCs), based on an atmospheric general circulation model (AGCM). In this paper, we present results from a climatological run of the model, and evaluate them with observational data. The simulation was conducted at the model horizontal resolution of T21 (5.6° × 5.6°) with 32 vertical layers from the surface to about 40 km altitude. The model reproduces well the observed vertical profiles of CO and NMHCs as ethane, propane, and acetone in almost all cases. The simulated seasonal cycle of surface CO in the biomass-burning region (South America) shows a good agreement with observation. In the case of nitric oxide (NO), the model generally reproduces the observed vertical profiles well, though it appears to somewhat underestimate NO in the upper troposphere in the low latitudes. Although the model overestimates nitric acid (HNO_3) in some cases like other model studies, the calculated HNO_3 is generally within the range of observations. Peroxyacetyl nitrate (PAN) appears to be generally simulated well, but overestimated by the model in some remote regions. In the simulation of O_3, the vertical profiles and seasonal variations observed in polluted and remote sites are well reproduced. The ozone distributions calculated in the biomass-burning-related regions as South America, Africa, and the South Atlantic show good agreements with observations. However, in the midlatitudes, the model tends to overestimate O_3 in the upper troposphere in winter-springtime, maybe indicating the need of improving the model's horizontal resolution. The model calculates a net chemical ozone production of 397 TgO_3/yr in the global troposphere (4895 TgO_3/yr production and 4498 TgO_3/yr destruction). The estimated net O_3 flux from the stratosphere is 593 TgO_3/yr, well within the range suggested by recent studies. The calculated global OH concentration leads to a global mean CH_4 lifetime of 7.9 years in this simulation. *INDEX TERMS:* 0365 Atmospheric Composition and Structure: Troposphere—composition and chemistry; 0368 Atmospheric Composition and Structure: Troposphere—constituent transport and chemistry; 3337 Meteorology and Atmospheric Dynamics: Numerical modeling and data assimilation; 3319 Meteorology and Atmospheric Dynamics: General circulation

Citation: Sudo, K., M. Takahashi, and H. Akimoto, CHASER: A global chemical model of the troposphere, 2, Model results and evaluation, *J. Geophys. Res.*, *107*(D21), 4586, doi:10.1029/2001JD001114, 2002.

1. Introduction

[2] In a companion paper [*Sudo et al.*, 2002], we have described a global chemical model of the troposphere, named Chemical AGCM for Study of Atmospheric Environment and Radiative forcing (CHASER). In this paper, we present and evaluate results from the model. The CHASER model, developed in the framework of Center for Climate System Research/National Institute for Environment Studies (CCSR/NIES) atmospheric general circulation model (AGCM) [*Numaguti*, 1993; *Numaguti et al.*, 1995], is aimed to study the tropospheric photochemistry and its influences on climate. Dynamical processes such as tracer transport, vertical diffusion, surface emissions, and deposition are simulated in the flow of the AGCM calculation. The chemistry component of CHASER calculates chemical transformations using variables of the AGCM (e.g., temperature, pressure, humidity) with a time step of 10 min (the dynamical and physical components are evaluated with a time step of 30 min in this model version). CHASER is

0148-0227/02/2001JD001114$09.00

Table 1. NASA GTE Campaign Regions and Dates[a]

Campaign	Dates	Region Name	Latitudes	Longitudes
ABLE-3A	7 July to 17 Aug. 1988	Alaska	55°N–75°N	190°E–205°E
ABLE-3B	6 July to 15 Aug. 1990	Ontario	45°N–60°N	270°E–280°E
		US-E-Coast	35°N–45°N	280°E–290°E
		Labrador	50°N–55°N	300°E–315°E
PEM-WEST-A	16 Sept. to 21 Oct. 1991	Hawaii	15°N–35°N	180°E–210°E
		Japan	25°N–40°N	135°E–150°E
		China-Coast	20°N–30°N	115°E–130°E
PEM-WEST-B	7 Feb. to 14 March 1994	Japan	25°N–40°N	135°E–150°E
		China-Coast	20°N–30°N	115°E–130°E
		Philippine Sea	5°N–20°N	135°E–150°E
PEM-Tropics-A	15 Aug. to 5 Oct. 1996	Hawaii	10°N–30°N	190°E–210°E
		Tahiti	20°S–0	200°E–230°E
		Fiji	30°S–10°S	170°E–190°E
PEM-Tropics-B	6 March to 18 April 1999	Hawaii	10°N–30°N	190°E–210°E
		Tahiti	20°S–0	200°E–230°E
		Easter-Island	40°S–20°S	240°E–260E
		Fiji	30°S–10°S	170°E–190°E
TRACE-A	21 Sept. to 26 Oct. 1992	S-Africa	25°S–5°S	15°E–35°E
		W-Africa-Coast	25°S–5°S	0°E–10°E
		S-Atlantic	20°S–0	340°E–350°E
		E-Brazil	15°S–5°S	310°E–320°E

[a] Only campaigns and regions used for the evaluation are listed.

basically driven on-line by climatological meteorology generated by the AGCM. For simulations of a specific time period, analyzed data of wind velocities, temperature, and specific humidity as from the European Center for Medium-Range Weather Forecasts (ECMWF) are optionally used as a constraint to the AGCM. For the simulation considered in this paper, the model was time-integrated without any constraint to the AGCM (climatological run). We have adopted the horizontal resolution of T21 (approximately 5.6° longitude × 5.6° latitude) for computational efficiency, with 32 layers in the vertical from the surface to about 40 km altitude for this simulation.

[3] The model considers natural and anthropogenic emission sources of 10 chemical compounds such as nitrogen oxides (NO_x), carbon monoxide (CO), and nonmethane hydrocarbons (NMHCs). The chemical component of the model simulates the basic chemical transformations of ozone (O_3), HO_x (= OH + HO_2), NO_x, CO, methane (CH_4) and the oxidation of NMHCs through 88 chemical and 25 photolytic reactions with 47 chemical species. The chemical scheme considers oxidation of 8 NMHCs species; ethane (C_2H_6), ethene (C_2H_4), propane (C_3H_8), propene (C_3H_6), acetone (CH_3COCH_3), isoprene (C_5H_8), terpenes ($C_{10}H_{16}$), and other NMHCs (a lumped species). It should be noted that this version of CHASER does not consider any heterogeneous (multiphase) reactions which may affect the levels of NO_x, HO_x, and some peroxy radicals.

[4] To validate the model capability to simulate the tropospheric photochemistry, it is necessary to evaluate the model results of ozone and species related to the ozone production and destruction (i.e., peroxy radicals, NO_x, CO, NMHCs, and reservoir species). Additionally, we need to carefully evaluate aldehydes and peroxyacetylnitrate (PAN) simulated by the model, to check the simplified chemical schemes for NMHCs adopted in the model (especially of the condensed isoprene and terpenes oxidation schemes, see *Sudo et al.* [2002]). We used several observational data sets for the model evaluation. The data set of *Emmons et al.* [2000], a compilation made from the NASA Global Tropospheric Experiment (GTE) aircraft campaigns, is mainly used to evaluate the vertical distributions of calculated chemical species. This data set is also used for evaluation of the IMAGES model [*Müller and Brasseur*, 1995] and the MOZART model [*Hauglustaine et al.*, 1998; *Emmons et al.*, 2000]. Information about the NASA GTE observations is briefly summarized in Table 1. For comparison with the GTE data, model results of individual species are averaged over the regions and dates as listed in Table 1. It should be noted that data from campaign observations like the NASA GTE are not climatological, and that there may be some differences in meteorological conditions between the campaign observations and the climatological simulations by the model. In the evaluation of ozone and surface CO, we made use of climatological data [e.g., *Logan*, 1999; *Novelli et al.*, 1992, 1994] in addition to the NASA GTE data.

[5] In this study, global tropospheric budget is calculated for some species such as CO (Table 2) and O_3 (Table 5). The budget is calculated for the region below the tropopause

Table 2. Global Budget of Tropospheric CO Calculated by CHASER[a]

	Global	NH	SH
Sources	2801		
Surface emission	1227		
Chemical production	1574	868	706
CH_2O + hν	952		
CH_2O + OH	417		
Others[b]	205		
Sinks	−2801		
STE[c]	−191		
Dry deposition	−133	−105	−28
Chemical loss (CO + OH)	−2610	−1585	−1025
Chemical lifetime, days	50	47	54
Burden, TgCO	333	193	140

[a] Values (in TgCO/yr) are calculated for the region below the tropopause height in the model. NH, Northern Hemisphere; SH, Southern Hemisphere.

[b] Mainly from isoprene and terpene oxidation.

[c] Stratosphere-troposphere exchange (CO flux to the stratosphere).

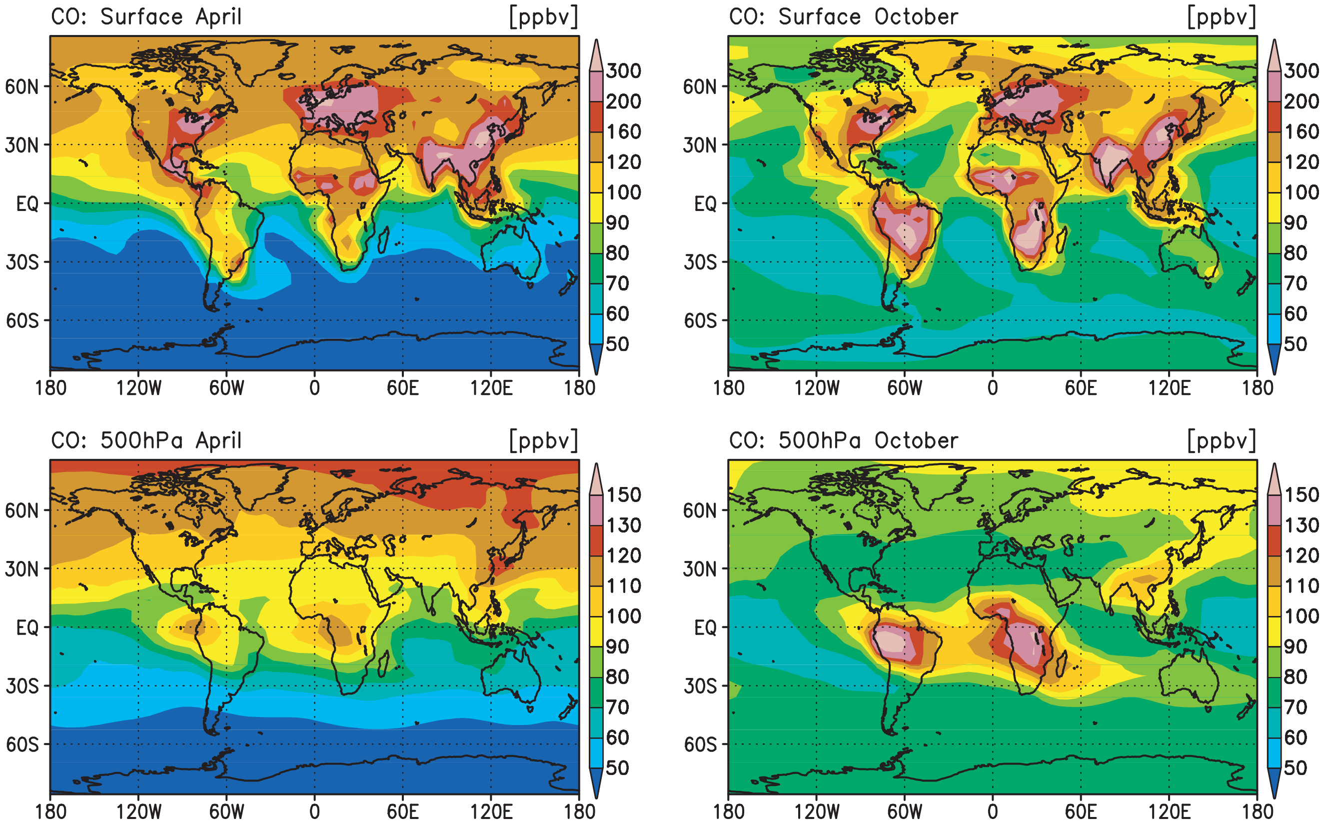

Figure 1. Calculated CO distributions (ppbv) at the surface and 500 hPa for April (left) and October (right).

height determined from the vertical temperature gradient (−2 K/km) in the model. Each budget shows global annual averages of values (source and sink, etc.) calculated at each time step (30 min in this study) in the model.

[6] We present the results and evaluation of CO and NMHCs in section 2, and reactive nitrogen oxides (NO_y) such as NO, HNO_3, PAN in section 3. The results of HO_x and related species (formaldehyde CH_2O, acetone, and peroxides) are evaluated in section 4. Finally, we present and evaluate the simulated ozone and the global tropospheric ozone budget calculated by the model in section 5.

2. CO and NMHCs

[7] Carbon monoxide (CO) and nonmethane hydrocarbons (NMHCs) play important roles in tropospheric chemistry, reacting with OH (controlling OH concentration) and significantly enhancing the ozone production. In this section, CO and NMHCs species (mainly of ethane and propane) simulated by CHASER are evaluated.

2.1. CO

[8] Figure 1 shows the calculated CO distributions at the surface and 500 hPa altitude for April and October. The CO mixing ratios calculated for April are generally higher than 100 ppbv in the Northern Hemisphere at both the surface and 500 hPa, with showing steep concentration gradients in the midlatitudes. At 500 hPa, two CO peaks are found in the tropics over South America and South Africa, reflecting vertical transport of CO from the surface and the CO production from oxidation of NMHCs species emitted by vegetation. The surface CO mixing ratios of 200–350 ppbv are predicted for both April and October in the industrial regions as the eastern United States, Europe, and eastern Asia. In October, high concentrations of CO (∼300 ppbv) are also calculated at the surface in South America and South Africa, associated with biomass-burning emissions considered in the model. The effect of biomass-burning emissions on CO is clearly seen at 500 hPa. CO emitted or produced at the surface in South America and South Africa is vertically transported, resulting in high levels of CO (120–150 ppbv) at this altitude. Relatively high CO concentrations (∼100 ppbv) are also extending over the South Atlantic, and over the Indian Ocean toward Australia like a plume.

[9] Figure 2 compares the seasonal cycle of surface CO mixing ratios observed and calculated at several sites. The model generally well reproduces the observed CO seasonal variations. The seasonal variations of surface CO, characterized by spring-maximum, are associated with the seasonal cycle of OH radical, transport of CO due to large-scale wind field and convection, and biomass burning (especially for the Southern Hemisphere). At Cuiaba located in the biomass-burning region in South America, the seasonal cycle of surface CO has a peak in September (500–600 ppbv), much affected by biomass-burning emissions. In the model, the seasonal variation of biomass-burning emissions is imposed by using hot spot (fire distribution) data derived from satellites [see *Sudo et al.*, 2002]. The model appears to reproduce the observed

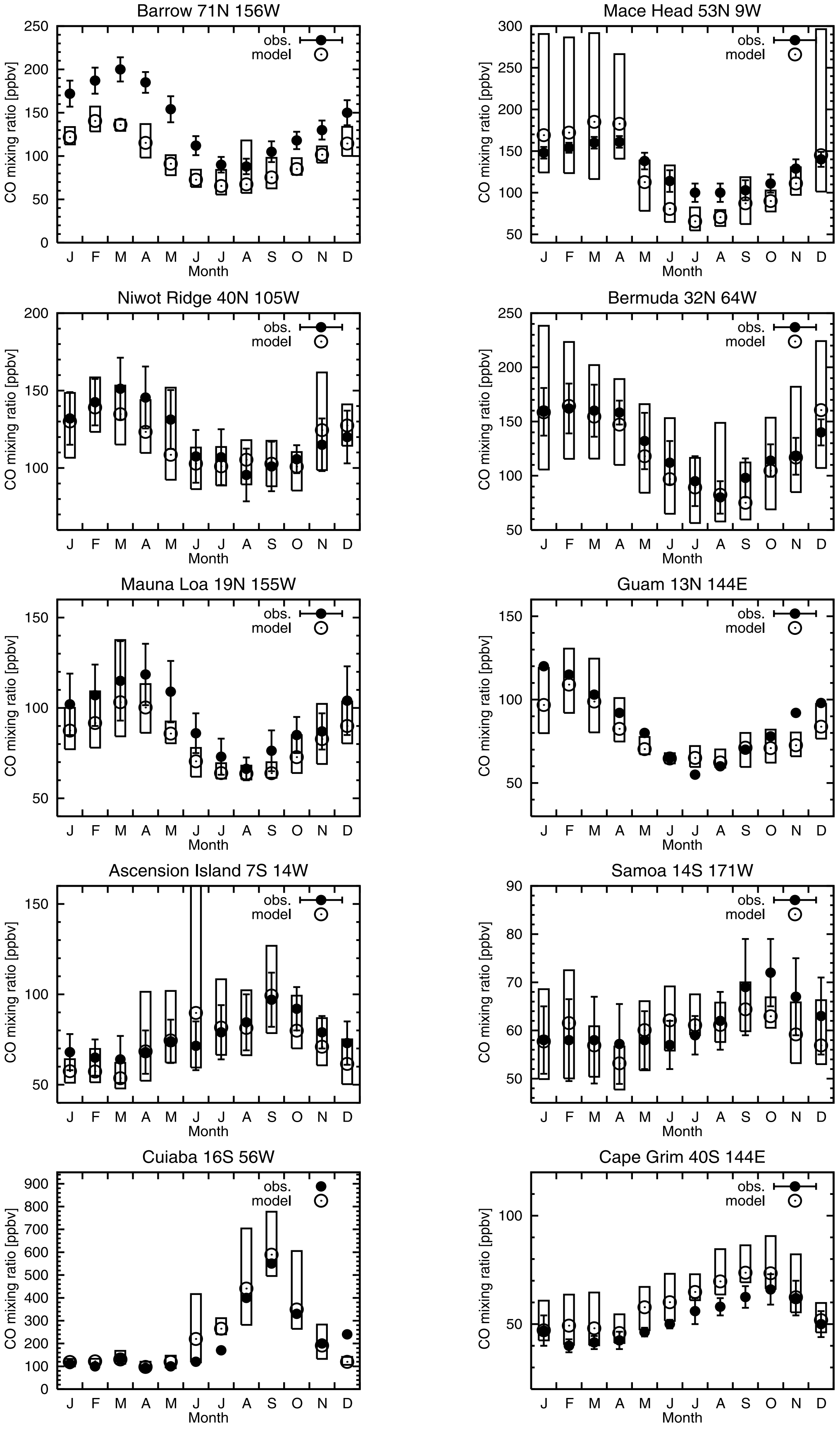

Figure 2. Observed (filled circles) and calculated (open circles) surface CO mixing ratios (ppbv) at several sites. Boxes indicate the range of the day-to-day variability calculated by the model. Measurements are taken from *Novelli et al.* [1992, 1994], and *Kirchhoff et al.* [1989] (for Cuiaba).

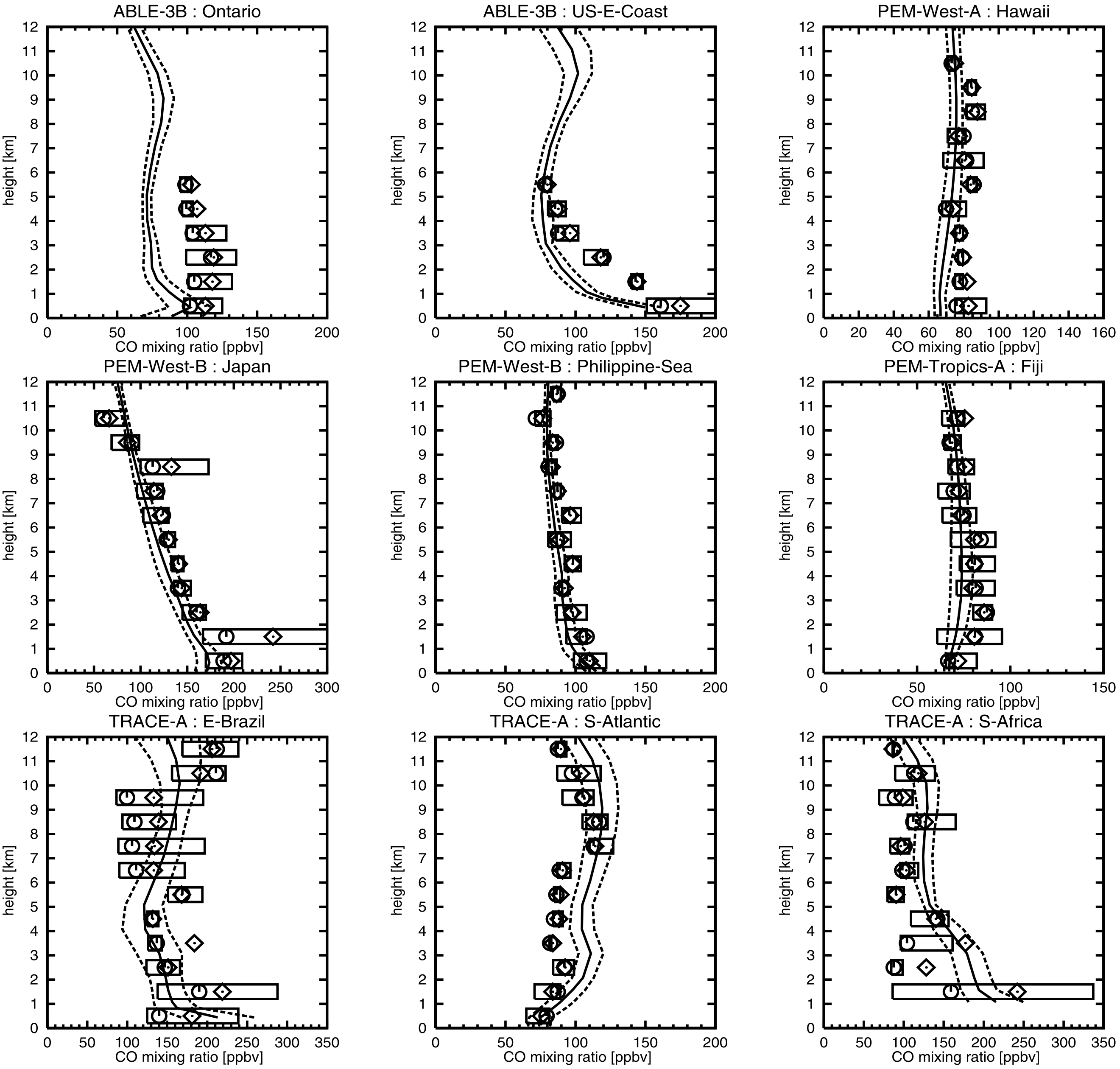

Figure 3. CO vertical profiles observed and calculated over the regions of GTE campaigns (listed in Table 1). Solid lines and dashed lines show temporal mean and ±1σ of the model calculation, respectively. The observations show mean (diamonds), median (circles), and inner 50% of the data (boxes).

seasonal cycle of surface CO at Cuiaba well, indicating the validity of the seasonal variation of biomass-burning emissions considered in the model. A CO maximum in spring is seen at Ascension (over the tropical Atlantic) associated with biomass burning in South America and Africa, which is also captured by the model. The seasonal cycle of CO observed and simulated at Mauna Loa (spring peak) is much associated with the transport from eastern Asia (Asian outflow) as suggested by the simulation of atmospheric ^{222}Rn [*Sudo et al.*, 2002]. At Barrow, the model underestimates the observed CO mixing ratios through a year, maybe indicating an underestimation of the CO surface emission in the high latitudes considered in the model.

[10] A comparison between the calculated and the observed vertical profiles of CO over the GTE regions listed in Table 1 is shown in Figure 3. The observed CO vertical profiles are generally well reproduced by the model. In remote regions like Hawaii, Philippine Sea, and Fiji, CO distributions are relatively uniform in the vertical with a range of 70–100 ppbv, whereas they are more variable in the source regions of biomass burning (E-Brazil and S-Africa) in the range of 100–200 ppbv. The model well captures the CO profiles observed over the Japan region during PEM-West-B, reproducing the CO increase in the lower troposphere (150–200 ppbv) due to industrial CO emissions. In the S-Atlantic region, CO levels are high in the free troposphere, especially in the upper troposphere (>8

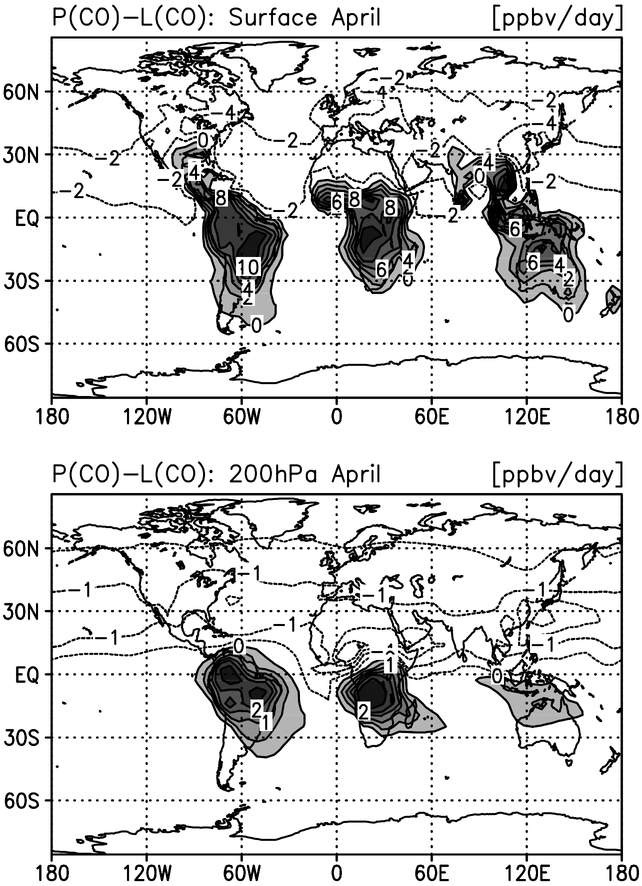

Figure 4. Net CO production rates (ppbv/d) calculated at the surface and 200 hPa altitude for April. Only positive areas are shaded.

km), much associated with transport from South Africa and South America as suggested by *Thompson et al.* [1996].

[11] Table 2 shows the global annual budget of tropospheric CO calculated by CHASER. The budget is calculated for the region below the tropopause height determined from the vertical temperature gradient (−2 K/km) in the model. CO has indirect sources from oxidation of CH_4 and NMHCs, as well as direct sources from surface emission (taken to be 1227 TgCO/yr in this simulation). The global chemical production of CO is estimated at 1574 TgCO/yr, showing a significant contribution from degradation of formaldehyde (CH_2O) and a contribution of ~13% from degradation of NMHCs. Note that the CO production from CH_2O includes oxidation processes of both CH_4 and NMHCs. The reaction with OH radical is the only chemical sink for CO and is estimated at 2610 TgCO/yr in the global troposphere by the model. The chemical lifetime of CO due to this reaction is estimated at about 1.7 months in annual average by the model, with longer lifetime (54 days) in the Southern Hemisphere than that in the Northern Hemisphere (47 days), reflecting the distribution of OH radical. This estimated global lifetime of CO, 1.7 months, is slightly shorter than the value of 2.0 months estimated by *Müller and Brasseur* [1995] and *Hauglustaine et al.* [1998]. The global CO burden is calculated as 333 TgCO (58% in NH, 42% in SH), in good agreement with recent model studies [e.g., *Müller and Brasseur*, 1995; *Hauglustaine et al.*, 1998]. The distributions of net CO chemical production P(CO)-L(CO) calculated for April are shown in Figure 4. At the surface, high positive production rates of 6–10 ppbv/d are calculated in South America, South Africa, etc., associated with biogenic emissions of NMHCs as isoprene and terpenes. Relatively high CO production rates (1–2 ppbv/d) are also calculated at 200 hPa over South America and South Africa, reflecting convective transport of NMHCs species from the surface. In other regions, CO is slowly destroyed by OH at rates of −0.5 to −2 ppbv/d.

2.2. NMHCs

[12] Distributions of NMHC species are spatially and temporally variable compared to CO, because of their relatively short lifetimes (ranging from several hours to weeks). Figure 5 shows the observed and the calculated seasonal cycles of surface C_2H_6 and C_3H_8. At the European site (Waldhof), the model captures the observed seasonal cycles of both C_2H_6 and C_3H_8. At Mauna Loa, the model appears to reproduce the observed C_2H_6 mixing ratios, though it slightly underestimates C_3H_8. The levels of C_2H_6 are much higher than C_3H_8 in Mauna Loa as C_2H_6 has a longer lifetime (2–3 weeks) compared to C_3H_8 (several days). The C_3H_8/C_2H_6 ratios are much less than 0.1 at Mauna Loa and 0.3–0.5 at Waldhof, indicating that the air at Mauna Loa is photochemically aged well (more than 5 days from a source region) [*Gregory et al.*, 1996] compared to Waldhof. At both sites, the calculated concentration and the temporal variability are high in winter and spring as well as CO. High temporal variabilities in winter-spring as seen in the calculated CO and NMHCs are also visible in the simulation of ^{222}Rn at the surface [*Sudo et al.*, 2002].

[13] In Figure 6, the calculated and the observed seasonal cycles of surface C_2H_4 and C_3H_6 are shown for two European sites. Alkenes such as C_2H_4, C_3H_6 are destroyed by the reaction with OH radical with a lifetime of ~1 day, and also by the reaction with O_3 with a lifetime of a day or several days. The model captures the observed seasonal variations of C_2H_4 and C_3H_6, reproducing well the winter maxima as with C_2H_6 and C_3H_8.

[14] The observed and the calculated vertical profiles of C_2H_6 and C_3H_8 are compared in Figure 7 and Figure 8, respectively. In the US-E-Coast region (ABLE-3B), the model does not capture the observed levels of C_2H_6 (1–2 ppbv) and C_3H_8 (0.7–0.8 ppbv) in the lower troposphere, probably indicating an underestimation of surface emissions around this region. In the Japan and the China-Coast regions (PEM-West-B), C_2H_6 and C_3H_8 levels are higher near the surface (C_2H_6 ~ 2 ppbv, C_3H_8 ~ 0.8 ppbv), associated with considerable emission sources around these regions. In these regions, the model appears to underestimate C_3H_8 near the surface, though it reproduces the profiles of C_2H_6 observed there well. In the tropical regions (Hawaii, PEM-West-A; Philippine Sea, PEM-West-B; PEM-Tropics-A, B), the model generally well reproduces the observed profiles of C_2H_6 and C_3H_8. In these tropical remote regions, C_2H_6 distributions are relatively uniform in the vertical ranging from 200 to 400 pptv, while C_3H_8 is more variable and shows relatively low mixing ratios (5–100 pptv) due to its short chemical lifetime. C_2H_6 in the Fiji region is well

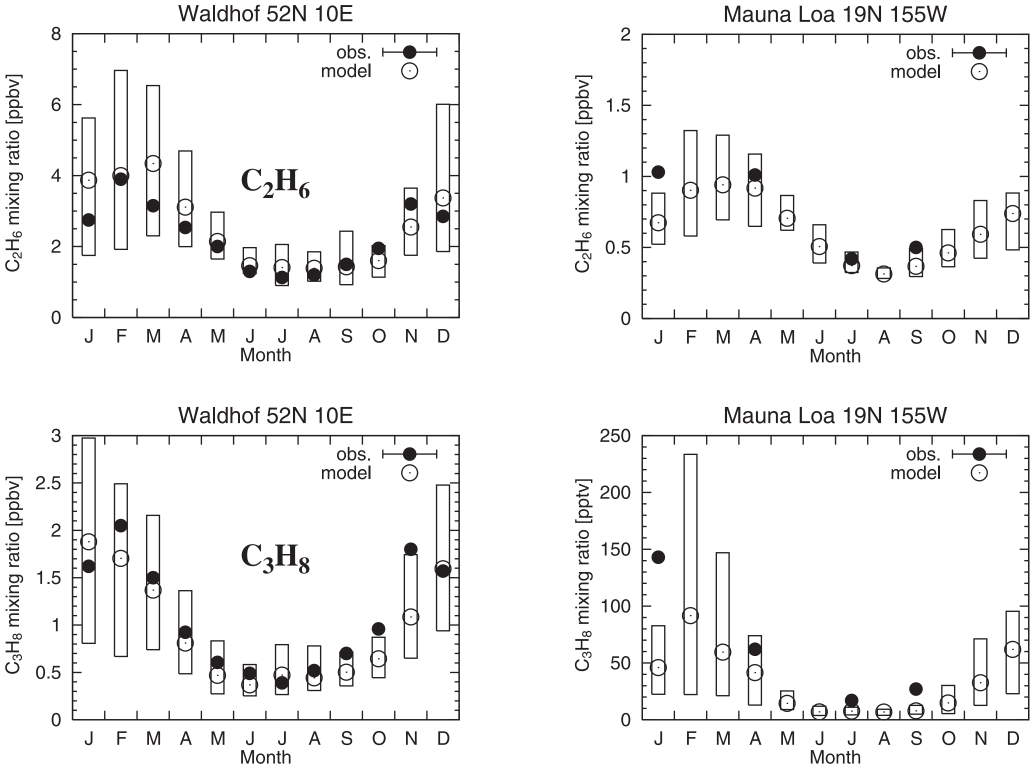

Figure 5. Observed (filled circles) and calculated (open circles) surface C_2H_6 (upper) and C_3H_8 (lower) mixing ratios (ppbv). Boxes indicate the range of the day-to-day variability calculated by the model. Measurements are taken from *Solberg et al.* [1996] and *Greenberg et al.* [1996] (for Mauna Loa).

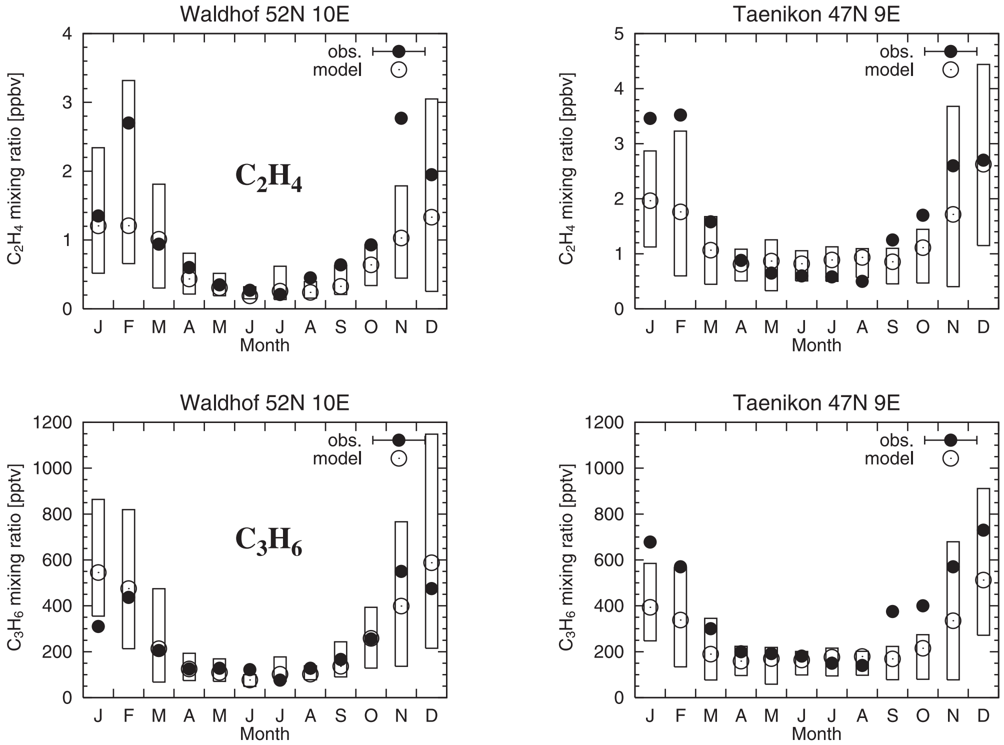

Figure 6. Observed (filled circles) and calculated (open circles) surface C_2H_4 (upper) and C_3H_6 (lower) mixing ratios (ppbv). Boxes indicate the range of the day-to-day variability calculated by the model. Measurements are taken from *Solberg et al.* [1996].

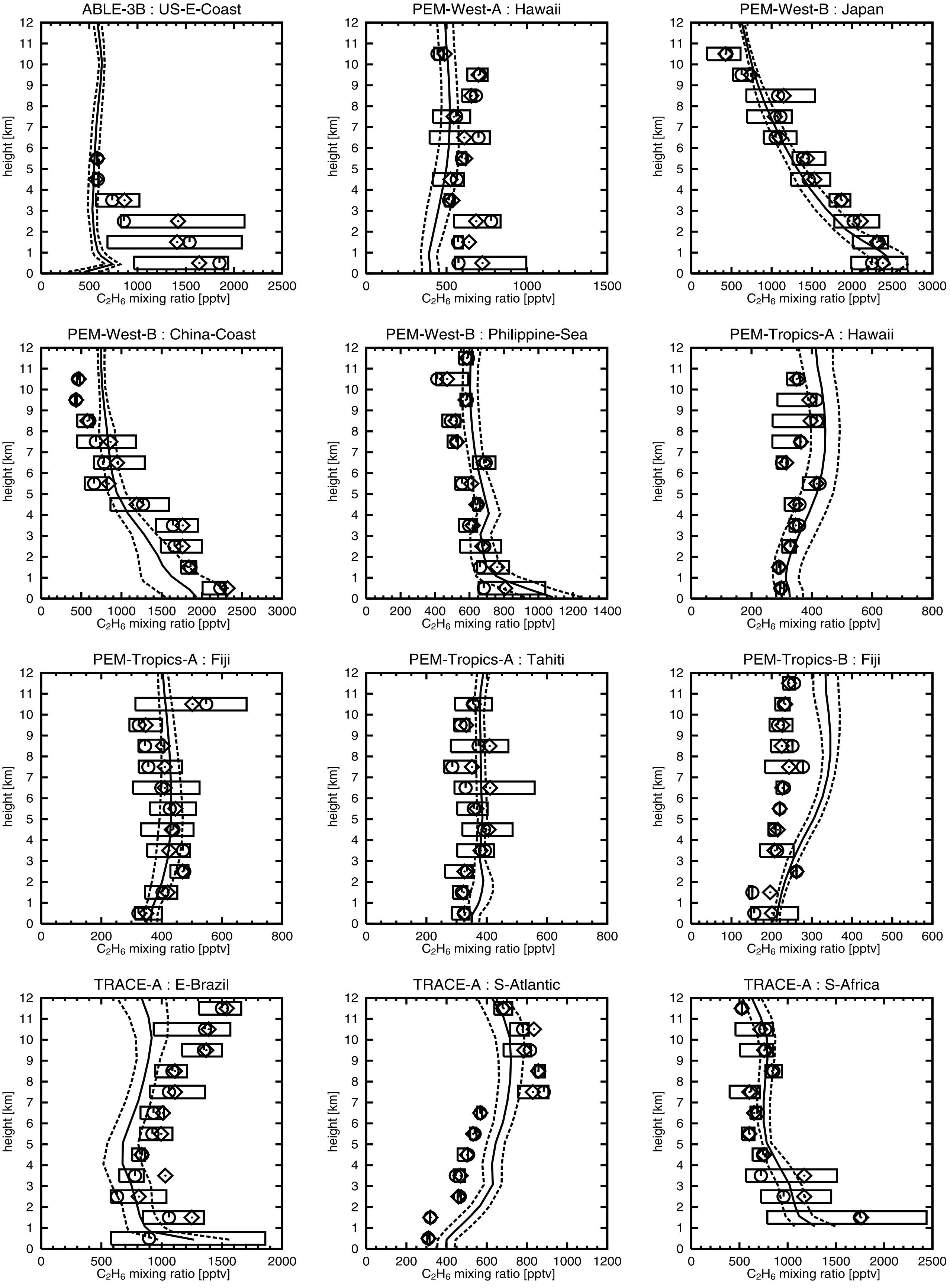

Figure 7. C_2H_6 vertical profiles observed and calculated over the regions of GTE campaigns (listed in Table 1). Solid lines and dashed lines show temporal mean and ±1σ of the model calculation, respectively. The observations show mean (diamonds), median (circles), and inner 50% of the data (boxes).

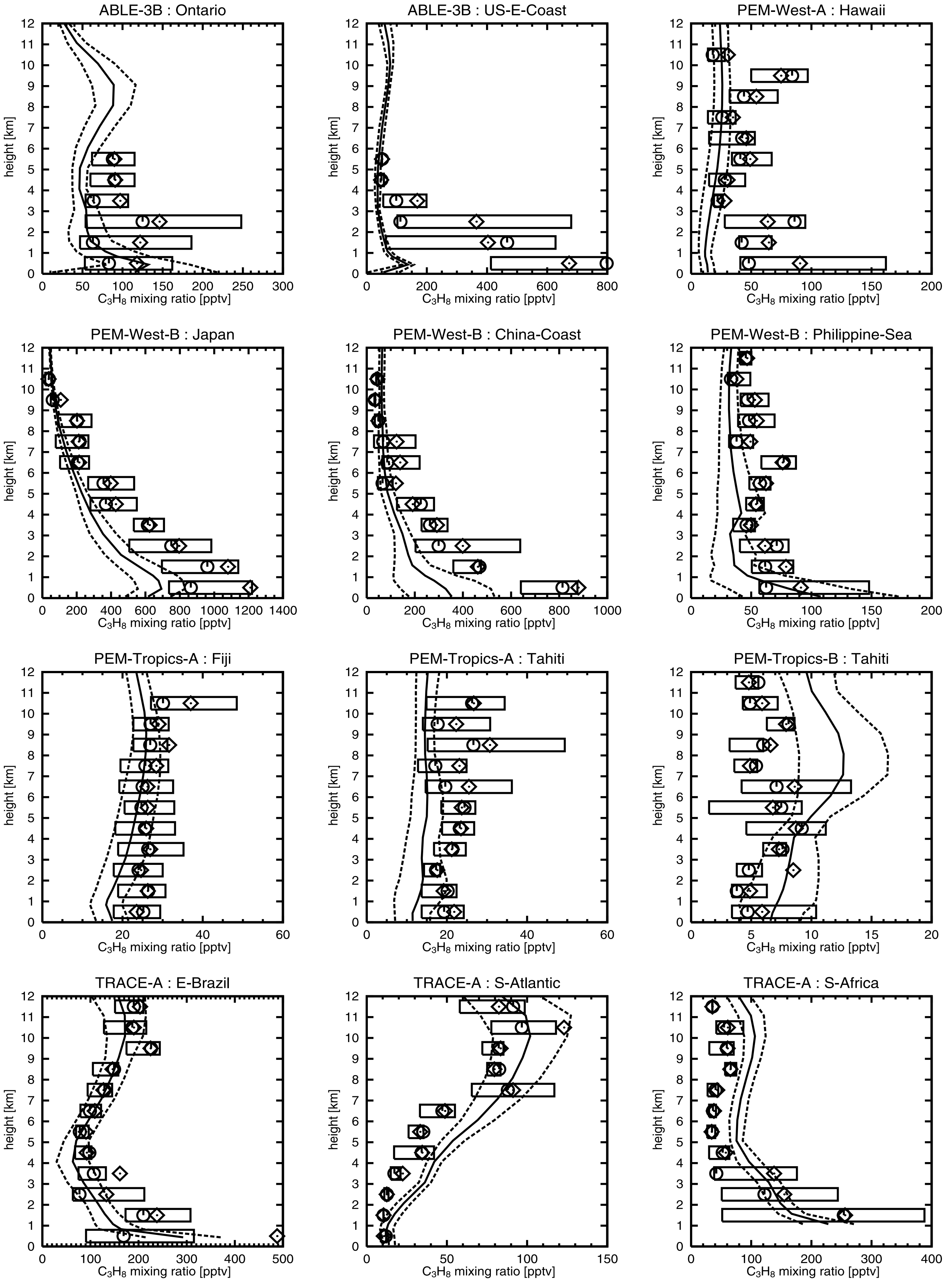

Figure 8. C_3H_8 vertical profiles observed and calculated over the regions of GTE campaigns (listed in Table 1). Solid lines and dashed lines show temporal mean and ±1σ of the model calculation, respectively. The observations show mean (diamonds), median (circles), and inner 50% of the data (boxes).

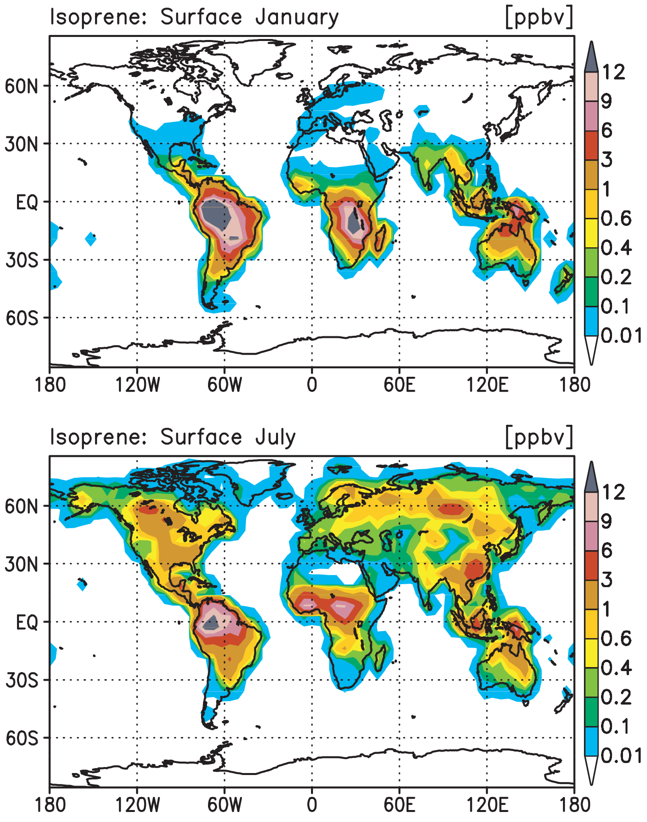

Figure 9. Calculated isoprene distributions (ppbv) at the surface for January and July.

simulated by the model in PEM-Tropics-A (August–October), but overestimated in the middle-upper troposphere in PEM-Tropics-B (March–April). Similarly, C_3H_8 in the Tahiti region is underestimated in PEM-Tropics-A, whereas it is overestimated in PEM-Tropics-B. In the biomass-burning regions (TRACE-A), the model appears to successfully simulate the vertical distributions of both C_2H_6 and C_3H_8. In the E-Brazil region, the model well captures the observed positive vertical gradient in the middle-upper troposphere associated with convective transport in this region (as revealed by *Fishman et al.* [1996]). In the S-Atlantic region, levels of C_2H_6 and C_3H_8 are higher (C_2H_6 $\sim$ 800 pptv, C_3H_8 $\sim$ 100 ppbv) in the upper troposphere as for CO (Figure 3). The observed increase in C_2H_6 and C_3H_8 with altitude over the S-Atlantic region is well reproduced by the model, though the discontinuous jumping at $\sim$7 km is not represented clearly.

[15] As isoprene and terpenes rapidly react with OH, O_3, and NO_3, they have much shorter lifetimes (hours), and the calculated distributions of these two NMHCs species are limited near source regions (i.e., vegetation) in the continental boundary layer. Figure 9 shows the distributions of isoprene calculated at the surface for January and July (24-hour average). The 24-hour averaged isoprene mixing ratios calculated in the boundary layer range from 1 to 8 ppbv in the tropical rain forests like the Amazon, in agreement with *Zimmerman et al.* [1988]. In July, the calculated mixing ratios of isoprene are 0.5–2 ppbv intemperate (deciduous) forests in the Northern Hemisphere, in agreement with measurements [e.g., *Martin et al.*, 1991; *Montzka et al.*, 1995]. Similarly, the terpenes distribution calculated near the surface has peaks in the tropical rain forests (1–2 ppbv), and shows high levels (0.2–1.5 ppbv) in cold-deciduous, needle-leaved forests in the northern high latitudes in July (not shown). In the model, the chemical lifetimes of isoprene and terpenes are estimated at 1.9 hour and 1.0 hour, respectively, in the annual and global average. The isoprene and terpenes mixing ratios calculated over the ocean are very low (generally equal to zero), due to their short chemical lifetimes.

3. Nitrogen Species

[16] Nitrogen oxides NO_x (= NO + NO_2) have a critical importance for ozone production and the HO_2/OH ratio in the troposphere. We must carefully evaluate the model results of NO_x and its reservoir species. Figure 10 shows the simulated NO_x distributions at the surface and 500 hPa altitude for January and July. As NO_x is converted to HNO_3 by the reaction with OH on a timescale of a day near the surface, the NO_x distribution is highly limited near the continental source regions, especially in summer. Surface NO_x levels over the ocean are in the range of 10–80 pptv in winter and generally lower than 20 pptv near the surface. In July, the model calculates the NO_x mixing ratios of 3 ppbv over the eastern United States, somewhat higher than the simulation of *Horowitz et al.* [1998]. In January, the high NO_x concentrations of 5–10 ppbv are calculated in the eastern United States and Europe, reflecting a longer lifetime of NO_x. We should note here that the heterogeneous reaction of N_2O_5 on aerosols which consequently converts NO_x to HNO_3 is not considered in this model version. It is possible that the model overestimates the NO_x concentrations around these industrial (polluted) regions, as *Dentener and Crutzen* [1993] and other model simulations [e.g., *Müller and Brasseur*, 1995; *Wang et al.*, 1998a; *Wang et al.*, 1998b] suggest that the hydrolysis of N_2O_5 in aerosols reduces NO_x levels in the polluted regions. On the contrary, some studies [e.g., *Hauglustaine et al.*, 1996; *Aumont et al.*, 1999; *Velders and Granier*, 2001] show that the heterogeneous conversion of HNO_3 to NO (i.e., NO_x) on aerosols such as black carbon (soot) has significant effects on NO_x in the polluted areas. At 500 hPa, NO_x peaks (60–100 pptv) are calculated over Africa and the Atlantic in January, associated with biomass burning in North Africa and with the lightning NO_x production. High NO_x concentration ($\sim$60 pptv) calculated over the Atlantic is also owing in the model to export from Africa and the in-situ NO_x recycling from HNO_3 and PAN. In the model, the positive net production of NO_x of 5–20 pptv/d is found in 6–12 km altitudes over the Atlantic, indicating the recycling process of NO_x. The calculation also shows a NO_x minimum (10–30 pptv) over South America (Brazil), reflecting rapid removal of HNO_3 by wet scavenging over this region during this season, and formation of PAN by the oxidation of biogenic NMHCs (mainly isoprene and terpenes). However, this NO_x minimum can be caused also by the overestimation of PAN formation by the chemical scheme of the model as described in the following. In July, the model predicts high NO_x concentrations (>60 pptv) over continents in the Northern Hemisphere centered around the south-

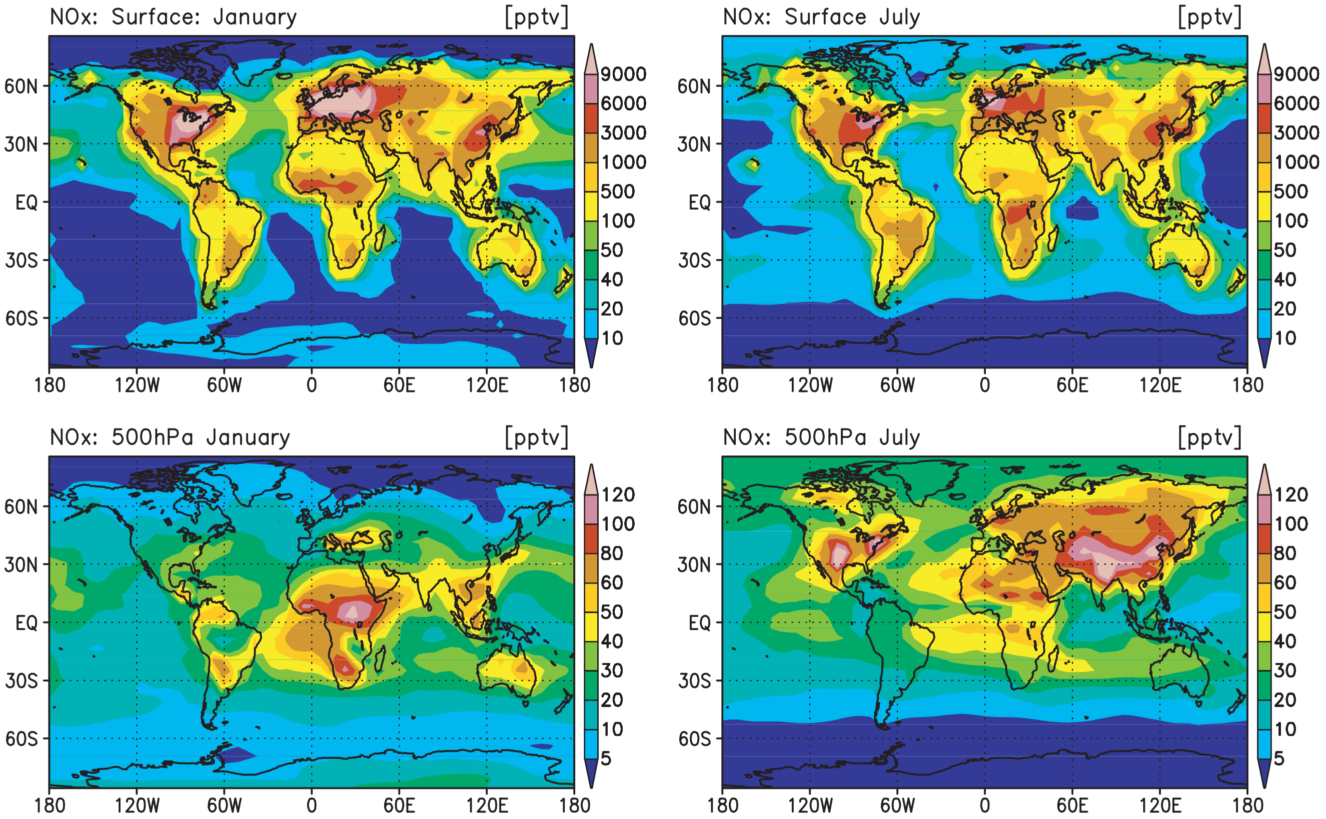

Figure 10. Calculated NO_x distributions (pptv) at the surface and 500 hPa for January (left) and July (right).

eastern United States and eastern Asia (100–150 pptv). These are attributed to convective transport of NO_x from the surface and to the lightning NO_x production, though the effect of the lightning NO_x may be less visible at this altitude.

[17] The observed and calculated vertical profiles of NO over the GTE regions listed in Table 1 are shown in Figure 11. Since the data includes only measurements in daytime (solar zenith angle <90°), the model results show average value of NO in daytime. In all cases, distributions of NO increase with altitude in the upper troposphere, due to the transport of stratospheric NO_x and HNO_3, the lightning NO_x production and the transport of surface emissions in convectively active regions, and increase in the lifetime of NO_x. The model simulates NO profiles well consistent with those observed during ABLE-3A (Alaska) and ABLE-3B (Ontario, US-E-Coast), calculating a rapid increase in the upper troposphere (>6 km) affected by stratospheric NO_x and HNO_3. The NO distributions over the polluted regions show “C-shaped” profiles. The model well simulates the observed “C-shaped” NO profile in the China-Coast region (PEM-West-B), but overestimating NO near the surface in the Japan region. The overestimation of NO in the Japan region is probably caused by the overestimation of HNO_3 in this region during PEM-West-B (see below, Figure 13). In the tropical regions (Philippine Sea, Fiji, and Tahiti), the model well reproduces the observed profiles below 8 km, though showing under estimations above 8 km. The under estimations of NO in the upper troposphere over Fiji and Tahiti (PEM-Tropics-A) may indicate the underestimation of lightning NO_x or biomass-burning emission of NO_x in Australia. In the source regions of biomass burning (TRACE-A: E-Brazil, S-Africa), the observations show “C-shaped” NO profiles, showing increase in the upper troposphere. The model appears to underestimate NO levels in the upper troposphere (higher than 10 km) in these two regions, with calculating NO profiles close to the observations in the lower-middle troposphere (below 10 km). Although this discrepancy is apparently caused by the underestimation of the flux of stratospheric NO_x, it can be attributed to the underestimation of lightning NO_x in the upper troposphere or the overestimation of PAN in the upper troposphere (the PAN/NO_x ratio is overestimated by a factor of 2–3 in the upper troposphere over these two regions, Figure 16), or possibly to the recycling of NO_x from HNO_3 on aerosols as tested by *Wang et al.* [1998b]. In the S-Atlantic region, both the observation and the calculation show a monotonic increase of NO with altitude, with the model slightly underestimating NO in the upper troposphere. The increase in the upper troposphere over S-Atlantic is related in the model to the gas-phase recycling of NO_x from HNO_3 and PAN, as well as the transport of NO_x from the source regions (South America and Africa). In the model, positive net production of NO_x (5–30 pptv/d) is calculated above 7 km over the Atlantic in September–October, indicating the recycling from HNO_3 and PAN exported from South America and Africa.

[18] Figure 12 shows the calculated distributions of HNO_3 at the surface and 500 hPa altitude for January and July. Peaks of HNO_3 mixing ratio (higher than 2 ppbv) are

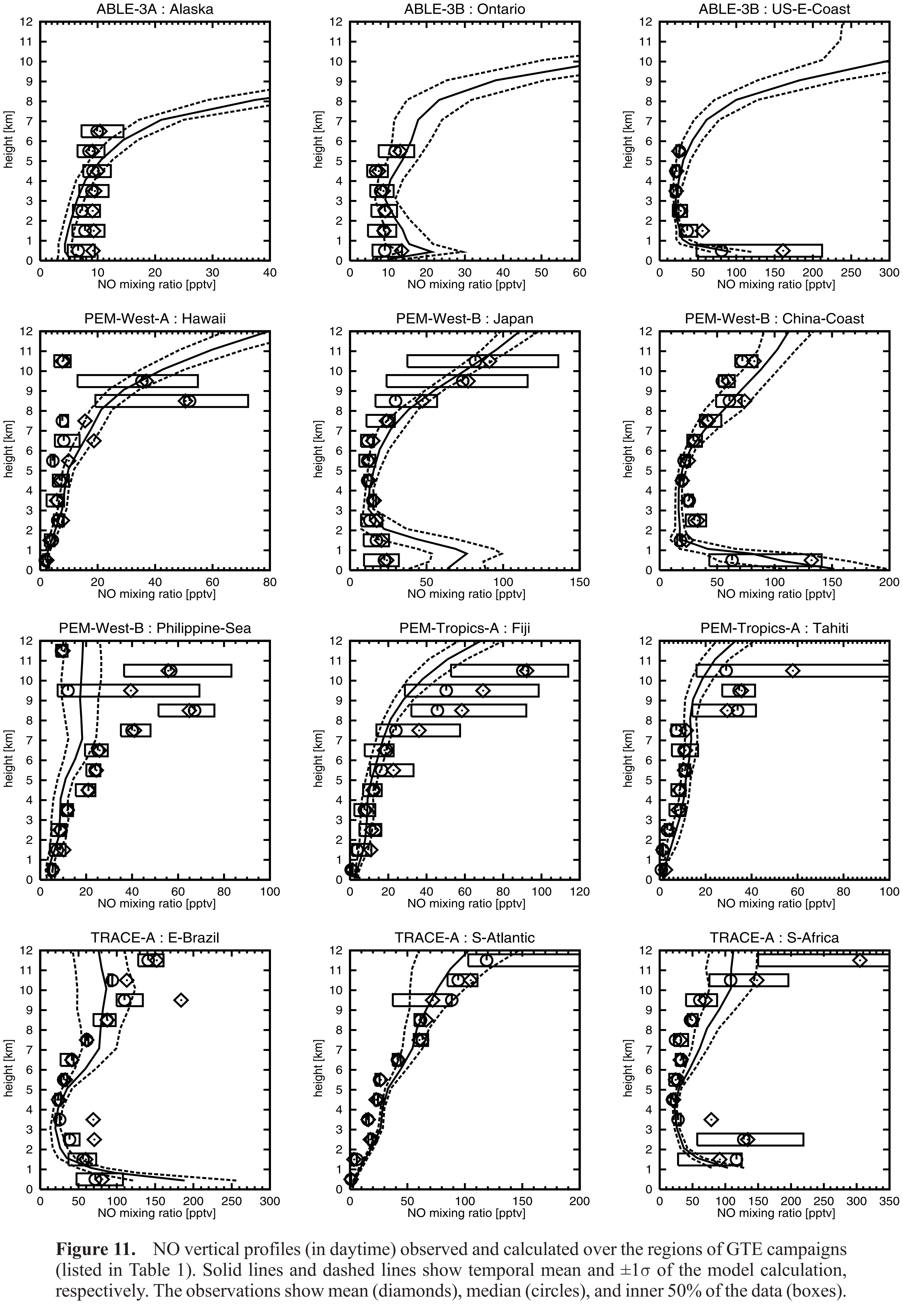

Figure 11. NO vertical profiles (in daytime) observed and calculated over the regions of GTE campaigns (listed in Table 1). Solid lines and dashed lines show temporal mean and ±1σ of the model calculation, respectively. The observations show mean (diamonds), median (circles), and inner 50% of the data (boxes).

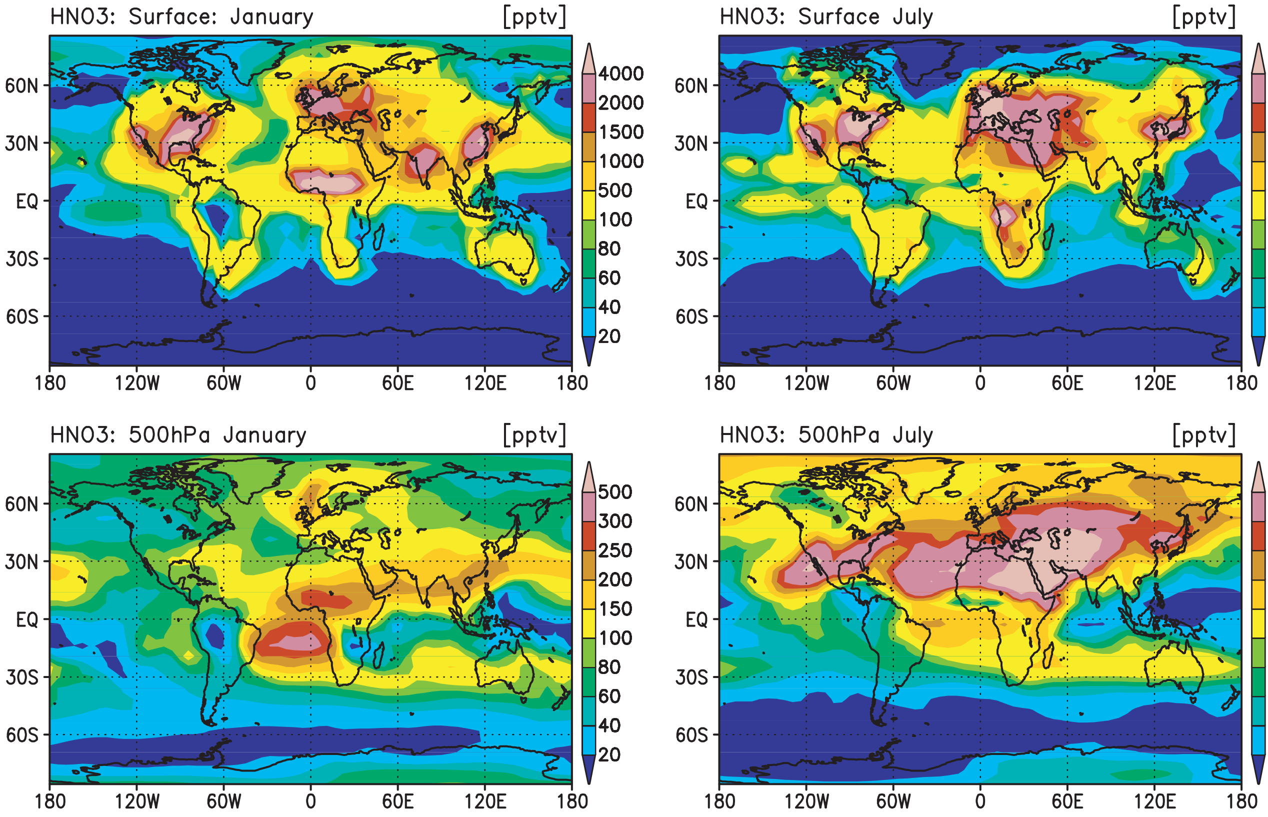

Figure 12. Calculated HNO_3 distributions (pptv) at the surface and 500 hPa for January (left) and July (right).

calculated at the surface in the polluted areas as the eastern United States (also including California), Europe, India, China, and the biomass-burning regions in both seasons. In July, the calculated HNO_3 mixing ratios in the eastern United States reach the range of 2–5 ppbv, higher than the measurements reported by *Parrish et al.* [1993] (1–2 ppbv). It should be noted again that the present model version of CHASER does not consider the conversion of N_2O_5 to HNO_3 on aerosols and inclusion of that conversion process in the model would increase HNO_3 levels especially near the surface. We should also note that the model does not account for the conversion of HNO_3 to NO_x on aerosols (like soot) [e.g., *Hauglustaine et al.*, 1996; *Aumont et al.*, 1999; *Velders and Granier*, 2001] and particulate nitrates (NO_3^-) [e.g., *Singh et al.*, 1996] which would reduce gas-phase HNO_3. At 500 hPa, a clear maximum of HNO_3 (200–400 pptv) is calculated over the South Atlantic in January, due to the export from South America and Africa, and to sparse precipitation over this region. Low HNO_3 levels are calculated over South America (less than 40 pptv) at both the surface and 500 hPa in January. In the model, these low HNO_3 levels appear to be associated with convective precipitation during this season, and also with low NO_x levels due to strong PAN formation in the oxidation process of NMHCs emitted from vegetation. In July, a maximum of HNO_3 in the range of 400–500 pptv are calculated over the Eurasian Continent and the southern United States, associated with the lightning NO_x production and the convective transport of surface NO_x emission. A significant outflow of HNO_3 is visible over the eastern North Pacific including Hawaii from the western United States. This outflow, however, seems to be somewhat over estimated. HNO_3 and HNO_3/NO_x calculated at Mauna Loa are 1.5–2 times higher than the measurements by the Mauna Loa Observatory Photochemistry Experiment (MLOPEX) 1 and 2 [*Ridley and Robinson*, 1992; *Atlas and Ridley*, 1996].

[19] A comparison between the calculated and the observed vertical profiles of HNO_3 over the GTE regions listed in Table 1 is shown in Figure 13. In ABLE-3B (July–August), the calculated HNO_3 profiles show increase in the upper troposphere, reflecting the effect of stratospheric HNO_3. The model overestimates observed HNO_3 in the middle-lower troposphere during ABLE-3B. In PEM-West-B (February), the model overestimates the profiles observed in the Japan region especially below 5 km, with calculating relatively consistent profiles over China-Coast and Philippine Sea. The overestimation over the Japan region may be attributed to the existence of aerosol nitrates (NO_3^-) as revealed by *Singh et al.* [1996] which the model does not account for. In the Tahiti region (PEM-Tropics-A, August–September), the model calculates a peak of HNO_3 at 1–2 km associated with the outflow of HNO_3 produced from biomass burning NO_x in South America, whereas the observation shows an increase of HNO_3 in 2–6 km. In TRACE-A (September–October), an overestimation is found in 1–4 km over the S-Atlantic region as previous model simulations [e.g., *Wang et al.*, 1998b; *Lawrence et al.*, 1999]. The model results show that the calculated peak at about 2 km is much associated with the transport from Africa and hence the overestimation over the S-Atlantic

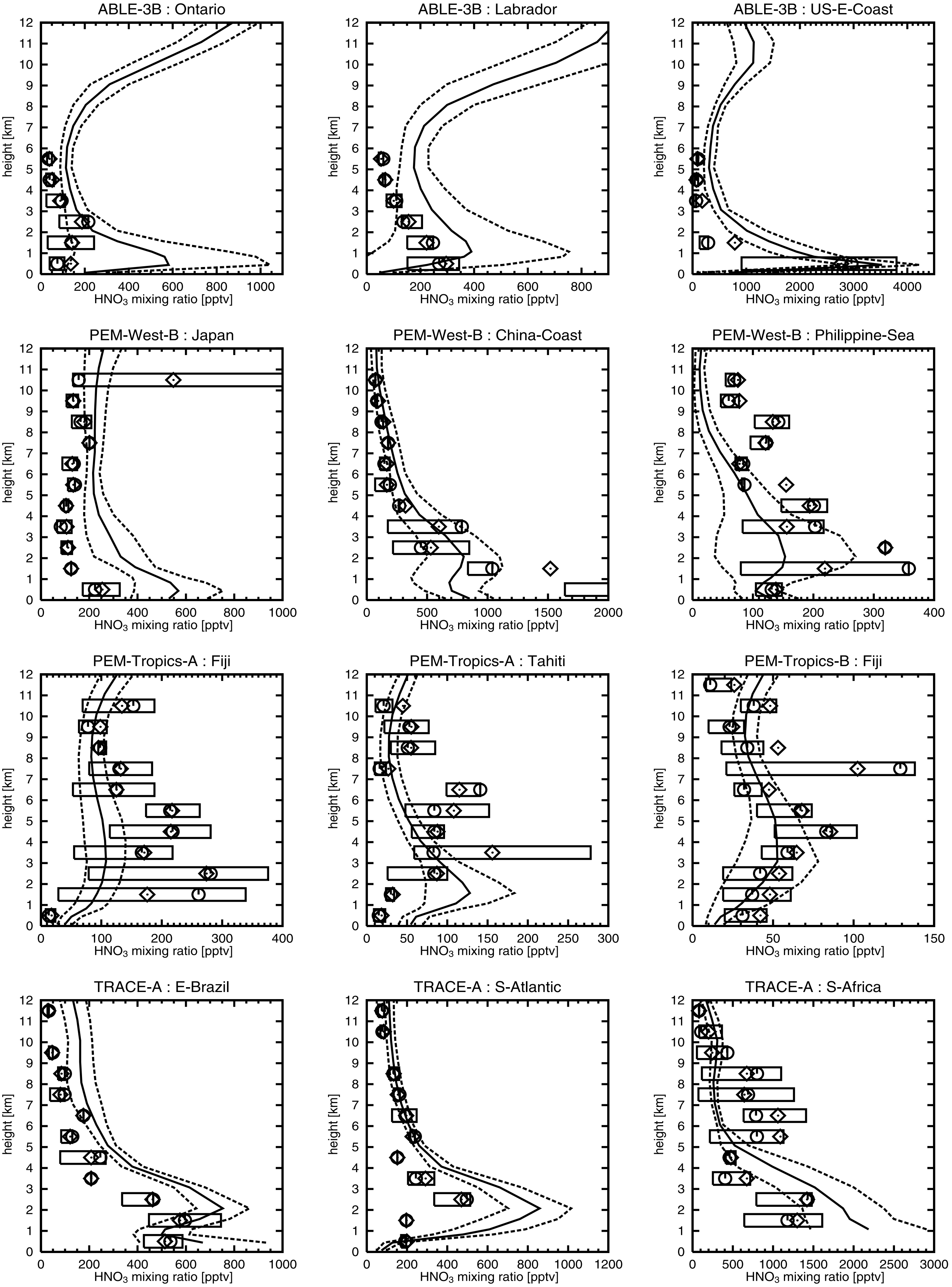

Figure 13. HNO$_3$ vertical profiles observed and calculated over the regions of GTE campaigns (listed in Table 1). Solid lines and dashed lines show temporal mean and ±1σ of the model calculation, respectively. The observations show mean (diamonds), median (circles), and inner 50% of the data (boxes).

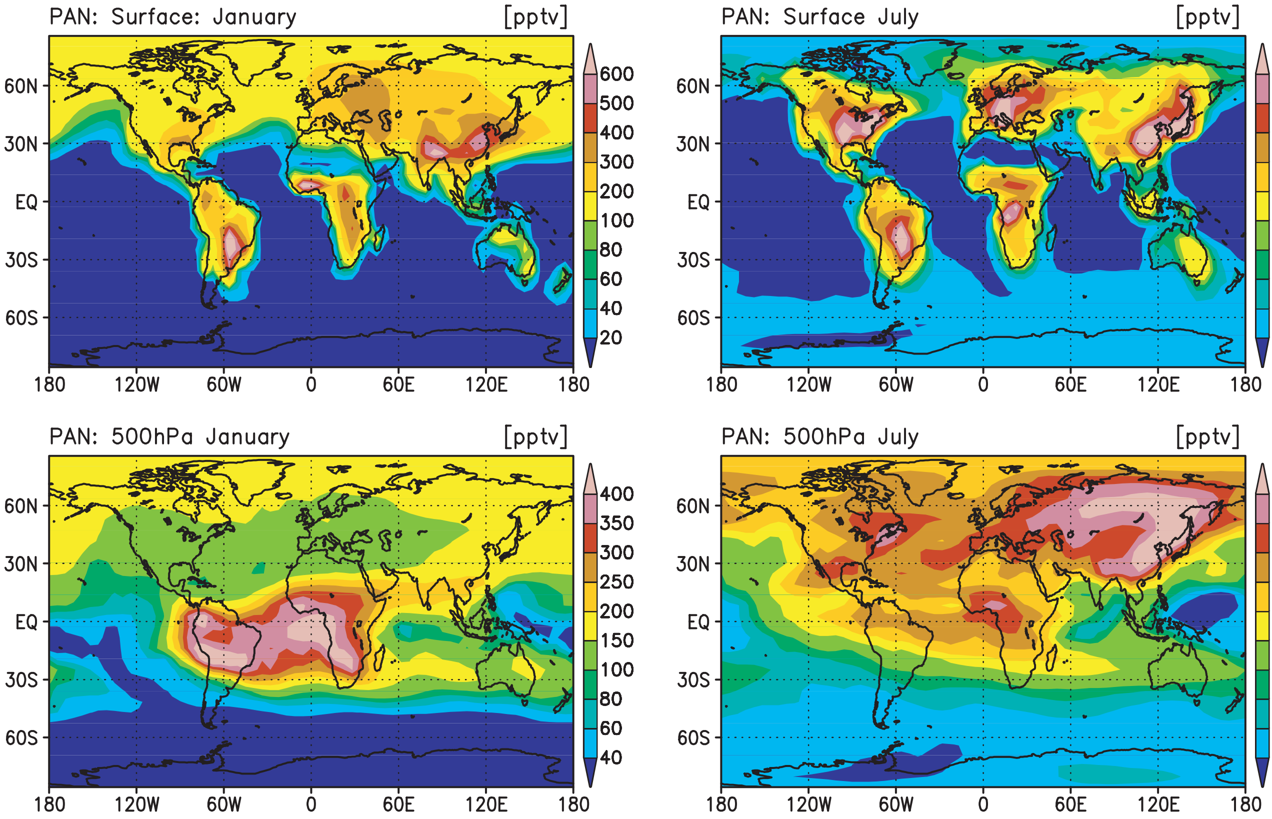

Figure 14. Calculated PAN distributions (pptv) at the surface and 500 hPa for January (left) and July (right).

(1–4 km) region is probably caused by the overestimation of HNO_3 in Africa as can be seen in the S-Africa region (Figure 13). The conversion of HNO_3 to NO on soot [e.g., *Hauglustaine et al.*, 1996; *Aumont et al.*, 1999; *Velders and Granier*, 2001] can be one of the possible reasons for this discrepancy. Consequently, our model results of HNO_3 and NO_x indicate the necessity of consideration of particulate nitrates and heterogeneous reactions on aerosols affecting the HNO_3/NO_x ratio.

[20] Peroxyacetyl nitrate (PAN) is also an important nitrogen species that acts as a source for NO_x in the remote atmosphere [*Fan et al.*, 1994; *Moxim et al.*, 1996]. PAN is formed by the reaction of NO_2 with peroxyacetyl radical and decomposes principally by thermolysis (slightly by photolysis). As peroxyacetyl radical is produced from the oxidation of NMHCs (ethane, propane, propene, acetone, isoprene, and terpenes in the model), we can validate the simplified scheme for NMHCs oxidation adopted in the model by evaluating the simulation of PAN. Figure 14 shows the calculated PAN distributions at the surface and 500 hPa for January and July. At the surface in January, high levels of PAN (300–600 pptv) are calculated in South America and Africa associated with biogenic emissions of NMHCs over these regions. The model calculates the PAN concentrations of 100–200 pptv in the mid-high latitudes with a maximum (400–600 pptv) around India and China. In July, high concentrations of PAN (above 500 pptv) are predicted at the surface in the polluted areas (United States, Europe, eastern Asia including Japan). The model results for the eastern United States in summer are consistent with the observation of *Parrish et al.* [1993] (0.5–1.5 ppbv). At 500 hPa in January, the model calculates high levels of PAN (300–450 pptv) over South America, Africa, and the South Atlantic, associated with NMHCs emissions by vegetation and lightning NO_x over South America and Africa. The calculated high concentrations of PAN over the Atlantic contribute to the positive net production (recycling) of NO_x (5–20 pptv/d) calculated in the middle-upper troposphere over the Atlantic during this season as described above. In July, high concentrations of PAN (above 300 pptv) are calculated over continents in the Northern Hemisphere with a maximum (above 400pptv) over the eastern Eurasian Continent, due to the lightning NO_x production and surface emissions of NO_x and NMHCs.

[21] Figure 15 shows the calculated and the observed vertical profiles of PAN over the GTE regions. In ABLE-3A (July–August), the model well reproduces the increase of PAN with height observed in Alaska, calculating PAN mixing ratios of 300–400 pptv in the upper troposphere. The calculated PAN profiles over the Ontario and the US-E regions (ABLE-3B) are fairly consistent with the observations. PAN profiles observed during PEM-West-B are well simulated. In the Japan and the China-Coast regions, PAN levels increase near the surface (400–800 pptv), reflecting the abundance of NMHCs (e.g., Figures 7 and 8) and NO_x (Figure 11). For Fiji and Tahiti (PEM-Tropics-A), both the observation and the model show a peak of PAN (80–150 pptv) in 4–8 km, associated with the transport of PAN from South America, Africa, and Australia. The model, however, overestimates the PAN profiles in 4–10 km over Fiji and

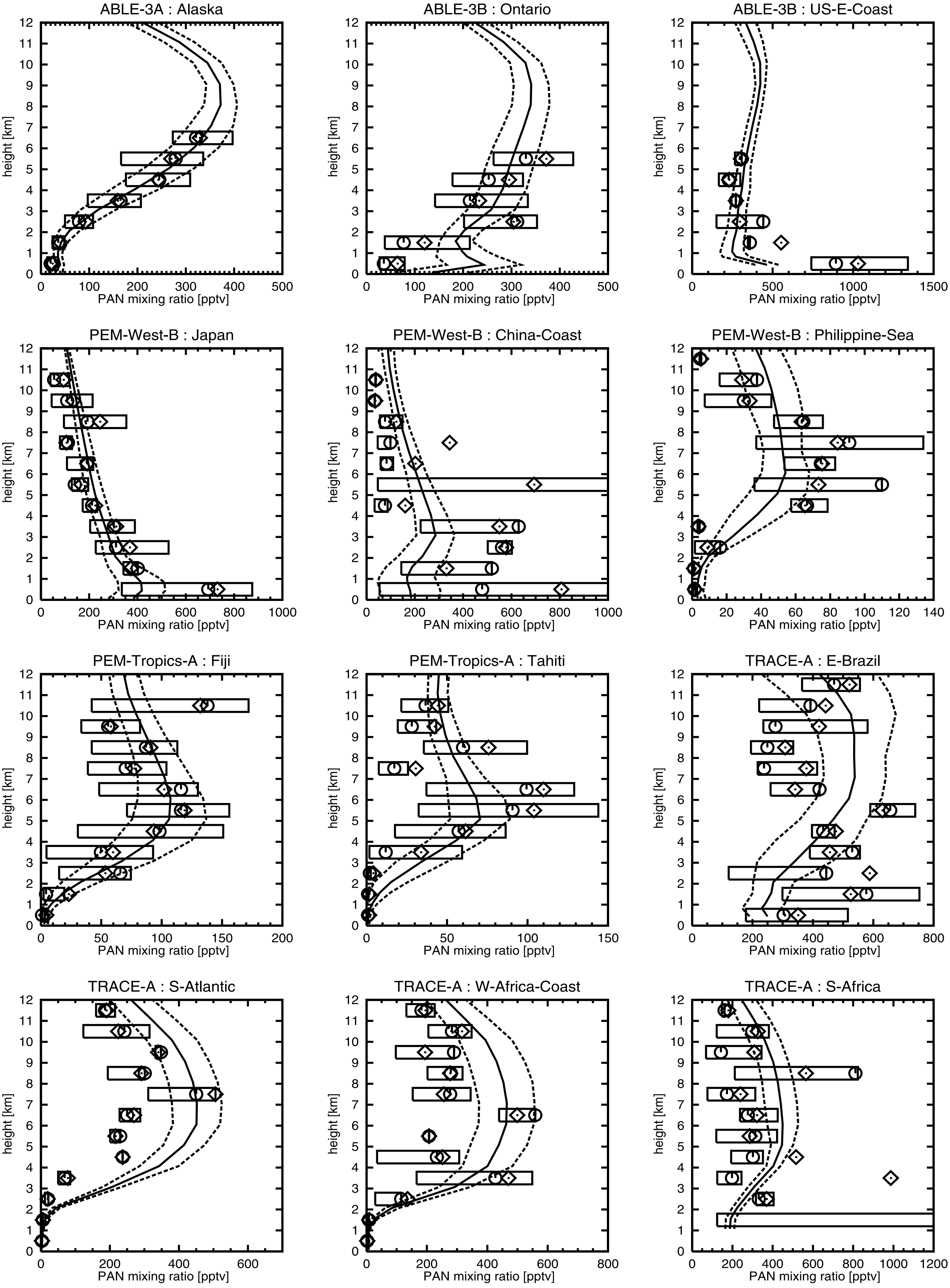

Figure 15. PAN vertical profiles observed and calculated over the regions of GTE campaigns (listed in Table 1). Solid lines and dashed lines show temporal mean and ±1σ of the model calculation, respectively. The observations show mean (diamonds), median (circles), and inner 50% of the data (boxes).

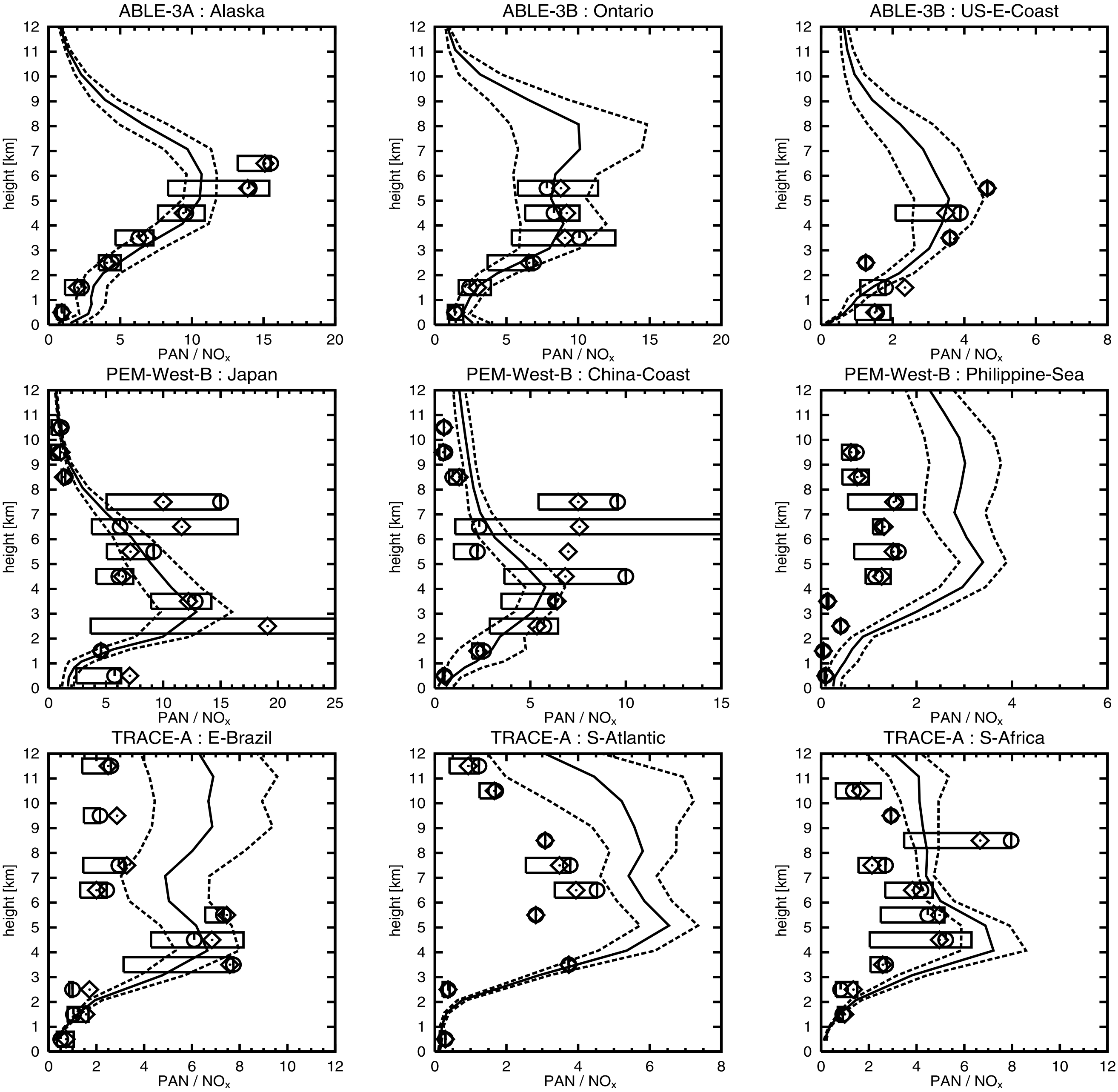

Figure 16. PAN/NO$_x$ ratio vertical profiles observed and calculated over the regions of GTE campaigns (listed in Table 1). Solid lines and dashed lines show temporal mean and ±1σ of the model calculation, respectively. The observations show mean (diamonds), median (circles), and inner 50% of the data (boxes).

Tahiti observed during PEM-Tropics-B (March–April) by a factor of 2–3 (not shown), maybe indicating that the condensed isoprene and terpenes oxidation scheme [*Pöschl et al.*, 2000; see *Sudo et al.*, 2002] or the lumped NMHCs species (ONMV; see *Sudo et al.* [2002]) in the model produces too much peroxyacetyl radical and hence too much PAN. In the biomass-burning regions (TRACE-A), the model appears to reproduce the observed profiles of PAN, simulating the rapid decrease in PAN below 3 km (nearly zero) over the S-Atlantic region and the W-Africa-Coast region, and the increase in the middle troposphere (300–500 pptv). The model, however, tends to overestimate PAN levels in the middle-upper troposphere, indicating too strong PAN formation again. Figure 16 shows the calculated and the observed vertical profiles of PAN/NO$_x$ ratio over the GTE regions. The ratio is calculated in each time step in the model. The model generally reproduces the observed PAN/NO$_x$ ratios well, calculating a peak in the middle troposphere for individual cases. Over the Japan region (PEM-West-B), the model calculates a peak of the ratio reaching 10–15 in 2–5 km, while the calculated peak over the China-Coast region is ~6. An overestimation of the PAN/NO$_x$ ratio in the Philippine Sea region is associated with the underestimation of NO$_x$ in this region (Figure 11). For the regions of TRACE-A, the model overestimates the PAN/NO$_x$ ratio in the upper troposphere by a factor of 2–3, due

Table 3. Global Budget of NO_y Species Calculated by CHASER[a]

	Global
Sources	43.8
Surface emission	38.3
Lightning NO_x	5.0
Aircraft NO_x	0.55
Sinks	−42.4
Wet deposition	
HNO_3	−26.1
HNO_4	−0.77
Dry deposition	
HNO_3	−10.2
HNO_4	−0.04
NO_x	−2.87
PANs[b]	−1.64
ISON[c]	−0.78

[a] Values are in TgN/yr. $NO_y = NO + NO_2 + NO_3 + 2N_2O_5 + HNO_3 + HNO_4$ + PAN + MPAN + ISON + NALD in the model (NALD = nitroxy acetaldehyde).

[b] PAN (peroxyacetyl nitrate) + MPAN (higher peroxyacetyl nitrates).

[c] Isoprene nitrates.

to the underestimation of NO_x and the overestimation of PAN in these regions as described above.

[22] We also compared the seasonal cycle of PAN calculated at the surface with the observational data for several sites [*Bottenheim et al.*, 1994; *Houweling et al.*, 1998; *Ridley et al.*, 1998] (not shown). We found that the model overestimates PAN at Mauna Loa by a factor of 2, compared to the data of the MLOPEX [*Ridley et al.*, 1998]. For other sites, the calculated seasonal variations of PAN are consistent with observations.

[23] As for the overestimation of PAN by the model in some instances, there are two possible reasons. One is the overestimation of peroxyacetyl radical (CH_3COO_2) by the simplified chemical mechanism for NMHCs used in the model, as mentioned above. The other is heterogeneous loss of some peroxy radicals (RO_2) including CH_3COO_2 which is not taken into account in the model. RO_2 radicals produced by oxidation of unsaturated hydrocarbons such as isoprene possibly undergo uptake by aerosols [*Jacob*, 2000]. As RO_2 radicals formed by isoprene and terpenes oxidation are precursors of CH_3COO_2 radical, inclusion of uptake of such RO_2 radicals by aerosols would reduce PAN formation in the model.

[24] The budget of total nitrogen species (NO_y) calculated by CHASER is shown in Table 3. In this simulation, the NO_y sources amount to 43.8 TgN/yr (87.4%, surface emission; 11.4%, lightning; 1.2%, aircraft). They are balanced primarily with the wet and dry deposition of HNO_3 (∼83% of the source) in the model. The calculated global wet deposition of HNO_3 reaches a maximum in August–September. About 87% of the global deposition loss of HNO_3 is calculated in the Northern Hemisphere (13% in the Southern Hemisphere). A slight imbalance between the total source and the total sink for NO_y (1.4 TgN/yr) can be attributed to the transport to the stratosphere.

4. HO_x and Related Species

[25] OH radical plays a central role in the oxidation of chemical compounds (the oxidizing power of the atmosphere) and the production and destruction of ozone. OH is converted to HO_2 by the reactions with O_3, peroxides, and CO, and reversely HO_2 is converted to OH by the reactions with O_3 and NO on a timescale of minutes. HO_x (= OH + HO_2) is produced by the reaction of $O(^1D)$ with water vapor (H_2O) [*Levy*, 1971] and also by the oxidation of CH_4 and NMHCs. Decomposition of peroxides can be also a HO_x source in the upper troposphere [e.g., *Jaeglé et al.*, 1997; *Folkins et al.*, 1998; *Cohan et al.*, 1999]. The sinks for HO_x are the reactions of OH with CH_4, NMHCs, and HO_2, and the reactions of HO_2 with peroxy radicals to form peroxides (e.g., H_2O_2, CH_3OOH).

4.1. HO_x

[26] Figure 17 shows the zonal mean concentrations (molecules cm^{-3}) of OH calculated for January and July. In January, the calculated OH distribution shows a maximum (∼2.0 × 10^6 molecules cm^{-3}) in 10°S–30°S, reflecting the distributions of O_3, water vapor (H_2O), and UV radiation. This OH maximum is calculated at 2–4 km altitude, indicating the significant OH destruction by NMHCs and CO near the surface. We also conducted a

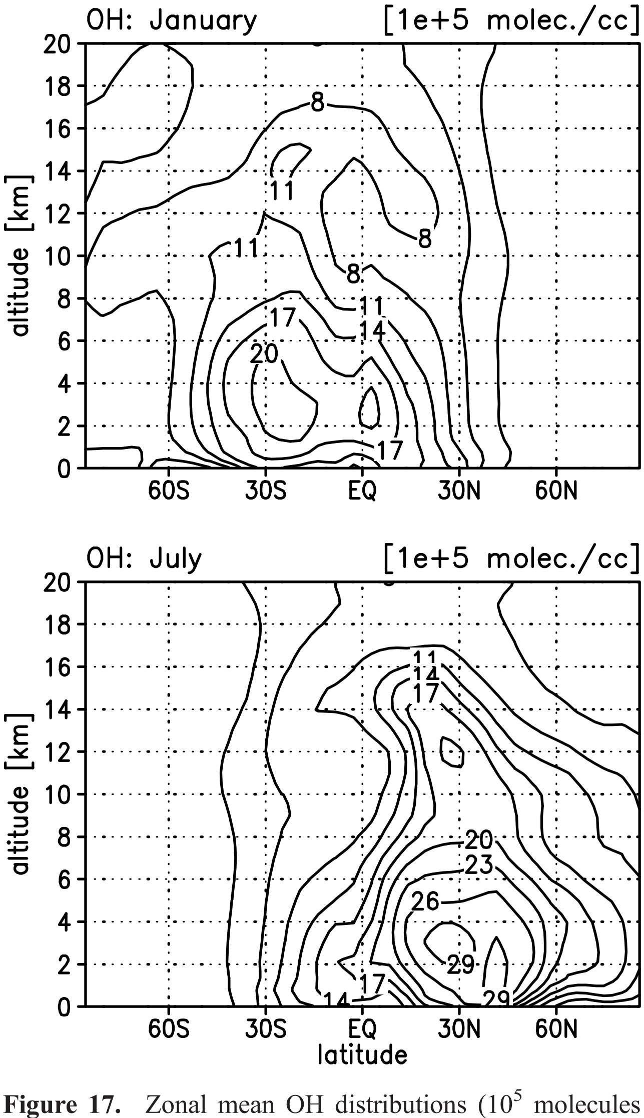

Figure 17. Zonal mean OH distributions (10^5 molecules cm^{-3}) calculated for January and July. Contour interval is 3 (10^5 molecules cm^{-3}).

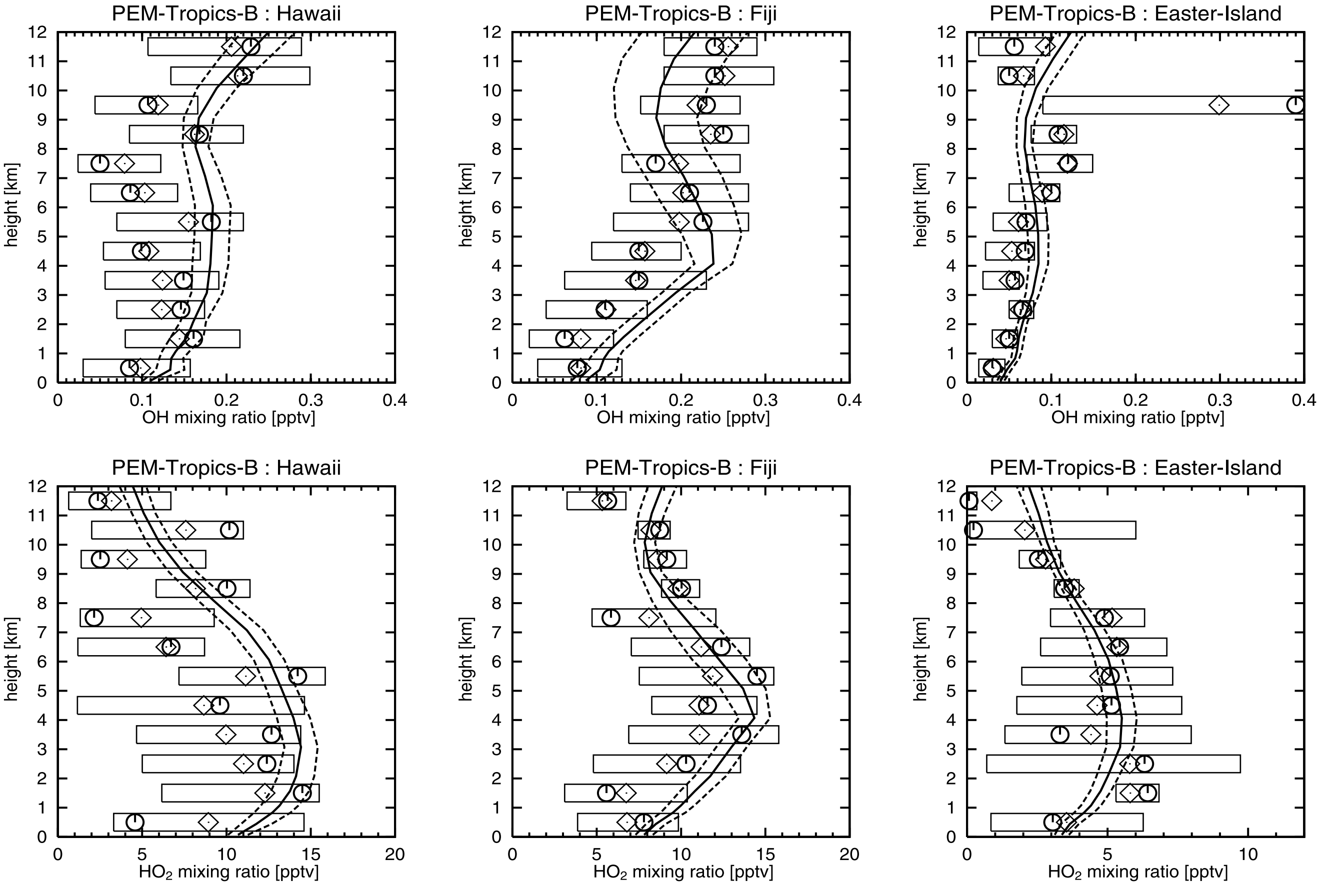

Figure 18. OH (upper) and HO_2 (lower) vertical profiles observed and calculated over the regions of GTE campaigns (listed in Table 1). The model results show mixing ratios of OH and HO_2 in the daytime average for Hawaii and Fiji, and in the 24-hour average for Easter-Island. Solid lines and dashed lines show temporal mean and $\pm 1\sigma$ of the model calculation, respectively. The observations show mean (diamonds), median (circles), and inner 50% of the data (boxes).

simulation without NMHCs chemistry. The simulation suggests that inclusion of NMHCs in the model reduces OH concentrations by a factor of 30–60% near the surface over land, as indicated by previous studies [e.g., *Wang et al.*, 1998c; *Roelofs and Lelieveld*, 2000]. In July, high concentrations of OH ($2.5-3.0 \times 10^6$ molecules cm^{-3}) are calculated in the northern midlatitudes in spite of the OH depletion by CO and NMHCs, as a result of high NO_x levels and enhanced O_3 over continents [*Thompson*, 1992]. Although the zonal mean OH distributions calculated for January and July are similar to those calculated by previous studies [e.g., *Müller and Brasseur*, 1995; *Wang et al.*, 1998b; *Hauglustaine et al.*, 1998], the maximum values of OH concentrations calculated in this simulation appear to be somewhat (10–30%) higher than them, probably indicating the differences in O_3 and NO_x levels. The tropospheric OH distribution presented here results in a global annual average of 1.10×10^6 molecules cm^{-3} (below 200 hPa), in good agreement with the global OH field (1.16×10^6 molecules cm^{-3}) simulated by *Spivakovsky et al.* [2000]. The annual and zonal mean HO_2/OH ratios calculated in the low-mid latitudes (45°S–45°N) are in the range of 50–100, and 100–600 in the high latitudes in both hemispheres below 200 hPa, much associated with the distribution of CO, O_3, and NO (not shown).

[27] Data available for evaluation of OH and HO_2 are quite limited because of the difficulty of measuring them. We made use of the data obtained during the NASA GTE campaign (PEM-Tropics-B) for evaluation of the HO_x distribution. The PEM-Tropics-B mission provided the first extensive measurements of the OH radical in the tropical troposphere. In Figure 18, the OH and HO_2 vertical profiles observed and calculated for the three distinct regions of PEM-Tropics-B (Hawaii, Fiji, Easter-Island) are shown. The model results are again averaged over the regions in Table 1 and dates during the PEM-Tropics-B expedition (6 March to 18 April). Since most of the GTE flights were taken place in daytime, we display the calculated mixing ratios of OH and HO_2 in the daytime average except for the Easter-Island region where the mission includes nighttime flights after sunset (We compare the 24-hour averaged model results for the Easter-Island region). In this comparison, we must note again that values measured by a flight campaign are fragmentary with respect to time and space for individual altitudes, and there may be discrepancies in representation of time and space between measurements and model calculations especially for short-lived radicals such as OH and HO_2. The comparison appears to show that the calculated HO_x species are generally consistent with the measurements. Daytime mixing ratios of OH and HO_2 are

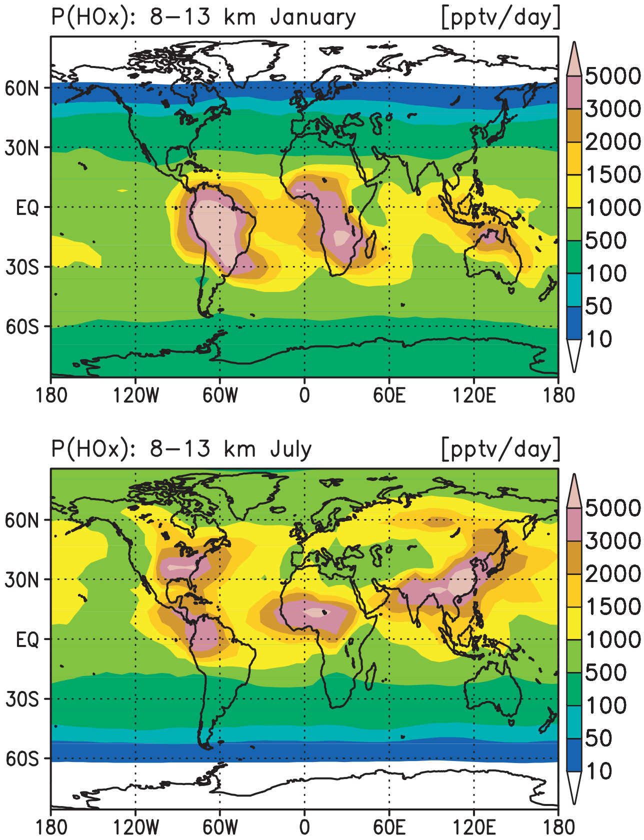

Figure 19. Distributions of the HO_x production term $P(HO_x)$ (pptv/d) in the upper troposphere (averaged over 8–13 km altitude) calculated for January and July.

in the ranges of 0.5–0.3 pptv and 5–15 pptv, respectively. The HO_2/OH ratio decreases in the upper troposphere, due to the increase in O_3 and NO. In the Fiji region, OH mixing ratios in the upper troposphere are considered to be underestimated by ~20%. Similar OH underestimation by the model is found for the other tropical regions of PEM-Tropics-B (Tahiti, Christmas Island). This discrepancy is attributed to the underestimation of NO and the slight overestimation of CO in the tropical upper troposphere (not shown). The calculated profiles of water vapor, ozone, acetone, CH_2O (see Figure 21) and CH_3OOH (Figure 27) over Fiji are quite consistent with the measurements during the PEM-Tropics-B, and the HO_x production rate calculated in the upper troposphere (8–12 km) over Fiji ranges from 500 to 2000 pptv/d, in good agreement with the box model calculation for the flight 10 around Fiji during the PEM-Tropics-B experiment [*Mari et al.*, 2002].

[28] The global OH field calculated by the model is also evaluated by comparing lifetime of CH_4 (methane) and CH_3CCl_3 (methylchloroform) in the model with measurements. *Prinn et al.* [1995] derived a global lifetime of 4.9 ± 0.3 years for CH_3CCl_3 below 200 hPa regarding OH oxidation, and obtained a global methane lifetime of 8.9 ± 0.6 years, based on observed CH_3CCl_3 concentrations. In this simulation, the calculated global OH concentrations (below 200 hPa) lead to a global CH_3CCl_3 lifetime of 4.7 years (4.1 years in the Northern Hemisphere, 5.4 years in the Southern Hemisphere), in agreement with the CH_3CCl_3 lifetime suggested by *Prinn et al.* [1995] (4.9 ± 0.3 years). The calculated global methane lifetime is 7.9 years, somewhat shorter than the estimation by *Prinn et al.* [1995].

[29] In Figure 19, we show the 24-hour average distributions of HO_x production rate (pptv/d) calculated in the upper troposphere (8–13 km) for January and July. As can be expected, the HO_x production in the upper troposphere is anomalously high in regions of high NMHCs level in the low latitudes. The HO_x production is high (3000–6000 pptv/d) over the tropical rain forests associated with biogenic emissions of NMHCs, being also high in July over the eastern United States and eastern Asia (India, China) (above 3000 pptv/d). Over the ocean in the low latitudes, the calculated production rate is in the range of 500–1500 pptv/d off continents, and 1500–3000 pptv/d in the vicinity of continents (e.g., over the South Atlantic in January and over the western Pacific including Japan in July).

[30] The global HO_x production and the mean lifetime of HO_x calculated by the model below the tropopause are presented in Table 4. The model calculates a global HO_x production of 216 TgH/yr corresponding to 1.3 × 10^{38} molecules/yr (57% in the Northern Hemisphere), and a global mean lifetime of 4.5 min. The differences in the production and the lifetime between the Northern Hemisphere and the Southern Hemisphere are owing to differences in the abundance of O_3 and NMHCs.

[31] It should be noted here that this simulation does not consider heterogeneous loss of HO_x radicals (especially of HO_2) on aerosols and cloud particles as suggested by *Horowitz et al.* [1998] and *Jacob* [2000]. Uptake of HO_2 by aerosols can be expected to reduce the levels of HO_2 and hence HO_x in polluted locations and in clouds.

4.2. Formaldehyde and Acetone

[32] The primary source for HO_x is the photolysis of ozone followed by the reaction of $O(^1D)$ with water vapor (H_2O). In dry regions as in the upper troposphere, acetone (CH_3COCH_3) [*Singh et al.*, 1995; *Arnold et al.*, 1997; *McKeen et al.*, 1997; *Wennberg et al.*, 1998], and formaldehyde and other aldehydes produced in the oxidation of methane and NMHCs [*Müller and Brasseur*, 1999] become important HO_x sources. Figure 20 shows the calculated distributions of formaldehyde (CH_2O) and acetone in the upper troposphere (8–13 km average) for January and July. CH_2O decomposes by photolysis on a timescale of hours in summer and hence effectively produces HO_x. In Figure 20, high concentrations (100–400 pptv) of CH_2O are calculated over the regions where NMHCs are abundant (i.e., tropical rain forests, the eastern United States, eastern Asia), well correlated with the HO_x production in the upper troposphere in Figure 19. Acetone similarly produces HO_x in the upper troposphere by its photolysis. As the lifetime of acetone against photolysis and OH oxidation is much longer than CH_2O (calculated global mean lifetime of acetone is 27

Table 4. Chemical Production and Lifetime of HO_x Calculated by CHASER[a]

	Global	NH	SH
Chemical production, TgH/yr	216.0	124.0	92.0
Chemical lifetime, min	4.5	3.7	5.7

[a] TgH/yr corresponds to 6.02 × 10^{35} molecules/yr.

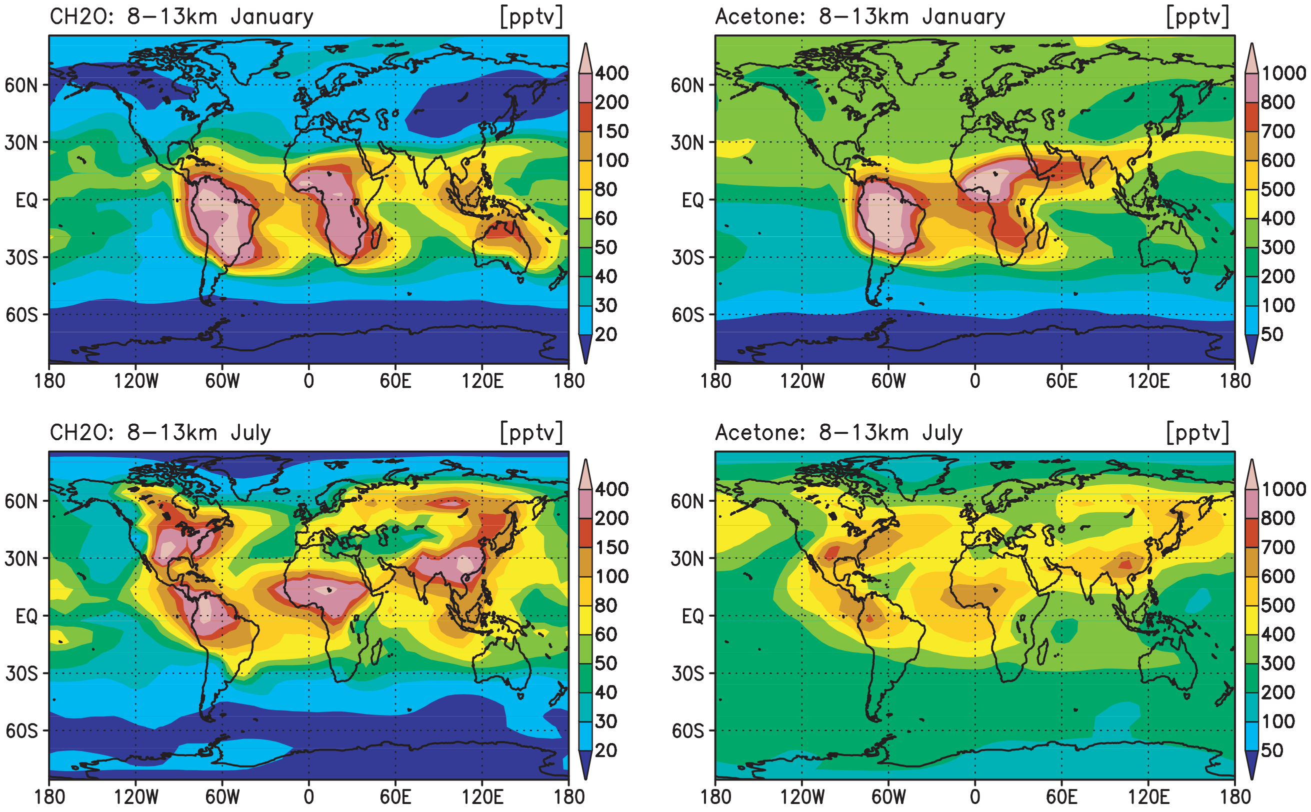

Figure 20. Calculated CH_2O (left) and acetone (right) distributions (pptv) in the upper troposphere (averaged over 8–13 km) for January and July.

days), acetone can be an important source for HO_x in remote regions as well as in source regions. The distributions of acetone (Figure 20) indicate the contribution of acetone to the HO_x production in the upper troposphere. In this simulation, the model includes acetone emission sources of 1.02 TgC/yr from industry, 7.17 TgC/yr from biomass burning, and 11.2 TgC/yr from vegetation. The model secondarily considers the acetone source from oxidation of NMHCs (propane C_3H_8 and terpenes in this simulation, see *Sudo et al.* [2002]). The calculated acetone in 8–13 km is high (700–1200 pptv) over South America and Africa including the South Atlantic in January, reflecting the emissions of acetone by vegetation and biomass burning, and the photochemical production of acetone by the oxidation of propane and terpenes. A long range transport of acetone from eastern Asia and North Africa to the North Pacific is visible in January associated with the long chemical lifetime of acetone in winter (>1 month). In July, the calculated distribution of acetone in the upper troposphere (8–13 km) is somewhat similar to that of CH_2O, showing peaks (>600 pptv) over the eastern United States, eastern Asia, and the tropical rain forests.

[33] Simulated vertical profiles of CH_2O and acetone are compared with the observations of the NASA GTE campaign in Figure 21 and Figure 22, respectively. In Figure 21, the model well simulates the CH_2O vertical profiles in the tropics observed during PEM-Tropics-B, though underestimating CH_2O in the upper troposphere over the Tahiti region. In these tropical regions, both the observation and the calculation show the CH_2O mixing ratios of 300–400 pptv near the surface and lower than 100 pptv in the upper troposphere (above 6 km). In the source regions of biomass burning (E-Brazil, S-Africa in TRACE-A), the model tends to overestimate CH_2O near the surface. In the west of African coast (W-Africa-Coast), CH_2O distribution is overestimated by the model at all altitudes, though the observed increase in the lower troposphere is simulated qualitatively. Our evaluation shows also a large overestimation of CH_2O in the South Atlantic region during the TRACE-A (not shown here). The overestimation of CH_2O over these regions may suggest that the chemical scheme for oxidation of isoprene, terpenes, and a lumped NMHCs species (ONMV, see *Sudo et al.* [2002]) adopted in the model produces too much CH_2O and hence too much HO_x. In Figure 22 showing acetone vertical profiles, the calculated vertical distributions of acetone are well within the range of the observations. Acetone mixing ratios are in the range of 500–1000 pptv near the source regions (Japan, China-Coast in PEM-West-B), and 300–500 pptv over the remote ocean as Philippine Sea (PEM-West-B) and the central Pacific (PEM-Tropics-B, not shown here). The simulated acetone mixing ratio reaches about 1500–2500 pptv in the source regions of biomass burning (E-Brazil and S-Africa). In the E-Brazil region, both the observation and the model show an increase in the upper troposphere, resulting from convective transport [*Fishman et al.*, 1996].

[34] To evaluate the seasonal variation of CH_2O and acetone calculated by the model, we display a comparison of seasonal cycle of CH_2O and acetone observed and calculated at the surface for an European site in Figure 23. The

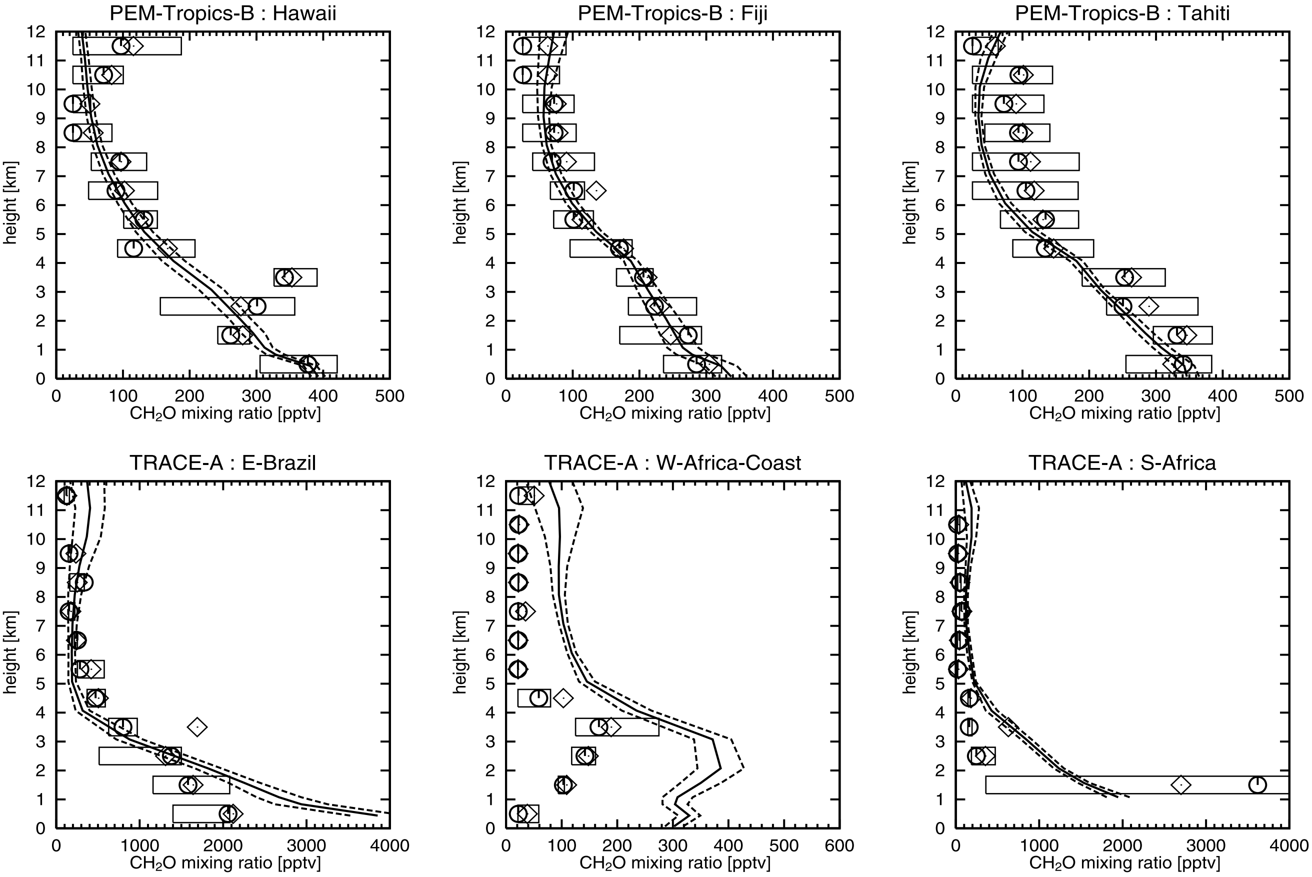

Figure 21. CH_2O vertical profiles observed and calculated over the regions of GTE campaigns (listed in Table 1). Solid lines and dashed lines show temporal mean and ±1σ of the model calculation, respectively. The observations show mean (diamonds), median (circles), and inner 50% of the data (boxes).

model appears to reproduce the observed seasonal variation of CH_2O, well simulating the enhancement of CH_2O (~1.5 ppbv) in summer due to production by the oxidation of methane and NMHCs. The simulated acetone at the surface is also consistent with the observation (1–1.5 ppbv), though the model somewhat underestimates acetone in summer.

4.3. Peroxides

[35] Peroxides are produced by the reactions of HO_2 with peroxy radicals and decompose by photolysis and OH reaction. Photolysis of peroxides transported to the upper troposphere are considered to be an important HO_x source [*Jaeglé et al.*, 1997; *Folkins et al.*, 1998; *Cohan et al.*, 1999]. Peroxides are, therefore, milestones for simulating the HO_x chemistry. We focus our attention here on H_2O_2 and CH_3OOH. Figure 24 shows the calculated distributions of H_2O_2 and CH_3OOH in the upper troposphere (8–13 km average) for January and July. H_2O_2 and CH_3OOH in the upper troposphere are much more abundant in the tropics (100–600 pptv) than in the extra-tropics (below 100 pptv). The distributions of both H_2O_2 and CH_3OOH show correlation to the distributions of HO_x production in Figure 19 as CH_2O and acetone, since H_2O_2 and CH_3OOH, formed by the HO_2 reactions, produce HO_x in the upper troposphere. The high levels of H_2O_2 and CH_3OOH calculated over South America and Africa (higher than 500 pptv) are owing to in-situ production of peroxides in the upper troposphere and convective transport of H_2O_2 and CH_3OOH overcoming wet deposition of them.

[36] Figure 25 shows the calculated zonal mean distributions of H_2O_2 and CH_3OOH in the annual average. Though H_2O_2 is removed by wet deposition more efficiently than CH_3OOH, the calculated H_2O_2 concentration is generally higher than CH_3OOH as suggested by measurements [e.g., *Talbot et al.*, 1996; *Heikes et al.*, 1996]. The distributions of both H_2O_2 and CH_3OOH show a peak near the surface (~1 km) in the tropics (H_2O_2 ~ 1.5 ppbv, CH_3OOH ~ 1.0 ppbv). Peaks of H_2O_2 and CH_3OOH are also calculated in the tropical upper troposphere. Although these peaks seem to be consistent with convective transport of H_2O_2 and CH_3OOH in the tropics, they may be overestimated by the model because the model probably overestimates the HO_2/HO ratio due to underestimation of NO in the tropical upper troposphere.

[37] In Figure 26, the observed and the calculated vertical profiles of H_2O_2 are compared. The model reproduces the observed H_2O_2 profiles in most cases. In the Japan region during PEM-West-B, the observation shows high variabilities of H_2O_2 (ranging from 100 to 900 pptv) below 9 km. The model also shows large standard deviations (±1σ) over this region. Over some regions as Fiji (PEM-Tropics-B), E-Brazil, S-Atlantic, and S-Africa (TRACE-A), the model

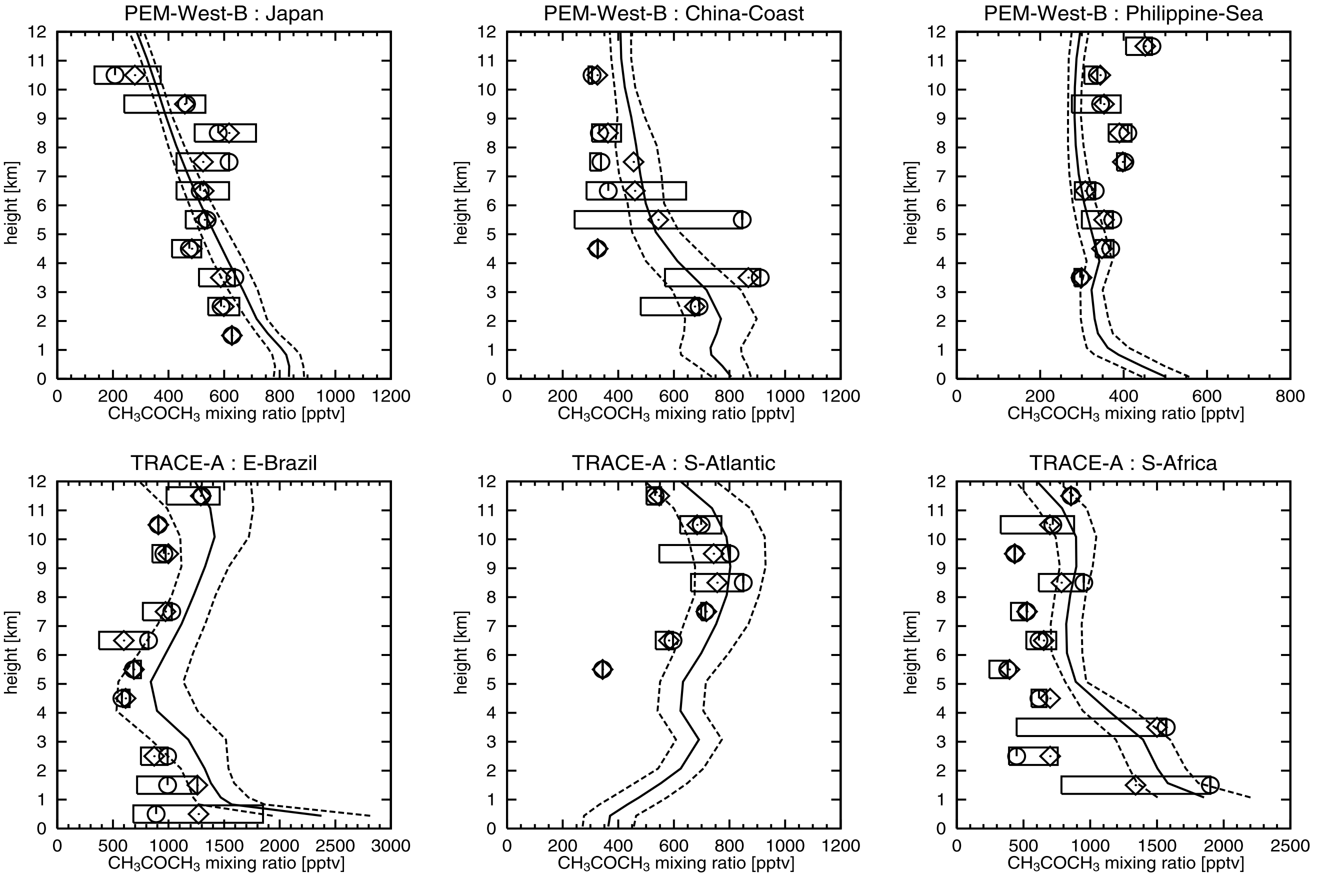

Figure 22. Acetone CH_3COCH_3 vertical profiles observed and calculated over the regions of GTE campaigns (listed in Table 1). Solid lines and dashed lines show temporal mean and $\pm 1\sigma$ of the model calculation, respectively. The observations show mean (diamonds), median (circles), and inner 50% of the data (boxes).

tends to overestimate H_2O_2 in the upper troposphere above 9 km, maybe coinciding with the underestimation of NO (i.e., overestimation of HO_2/OH) in the upper troposphere. In the S-Atlantic region, both the observation and the model show high level of H_2O_2 (~2000 pptv) in 1–4 km altitude, associated with the African outflow. Figure 27 is the same as Figure 26 but for CH_3OOH profiles. CH3OOH profiles are generally captured by the model as well as

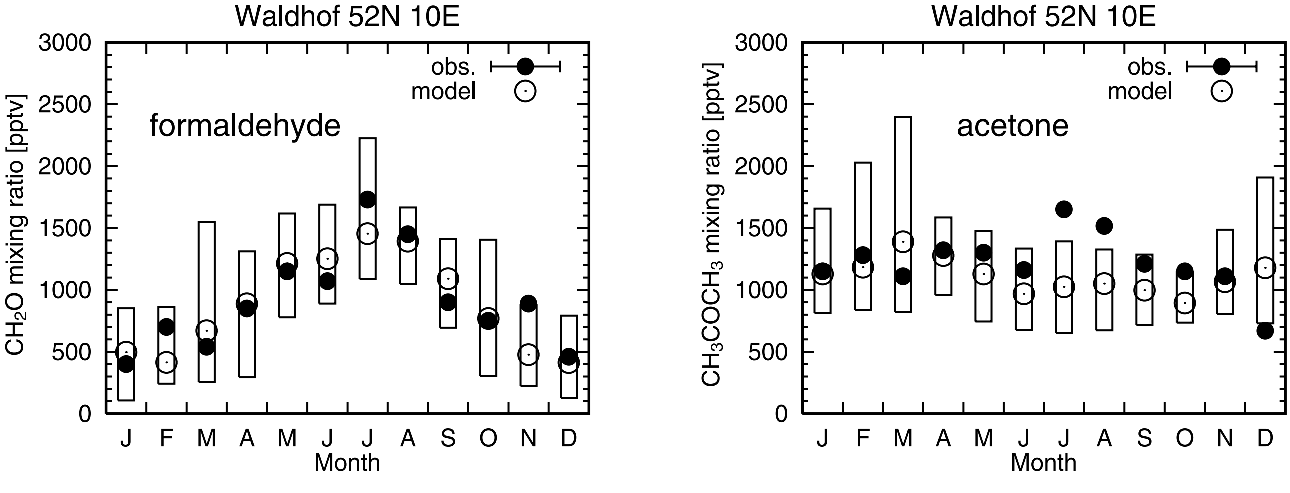

Figure 23. Observed (filled circles) and calculated (open circles) surface mixing ratios (pptv) of CH_2O (left) and acetone (right). Boxes indicate the range of the day-to-day variability calculated by the model. Measurements are taken from *Solberg et al.* [1996].

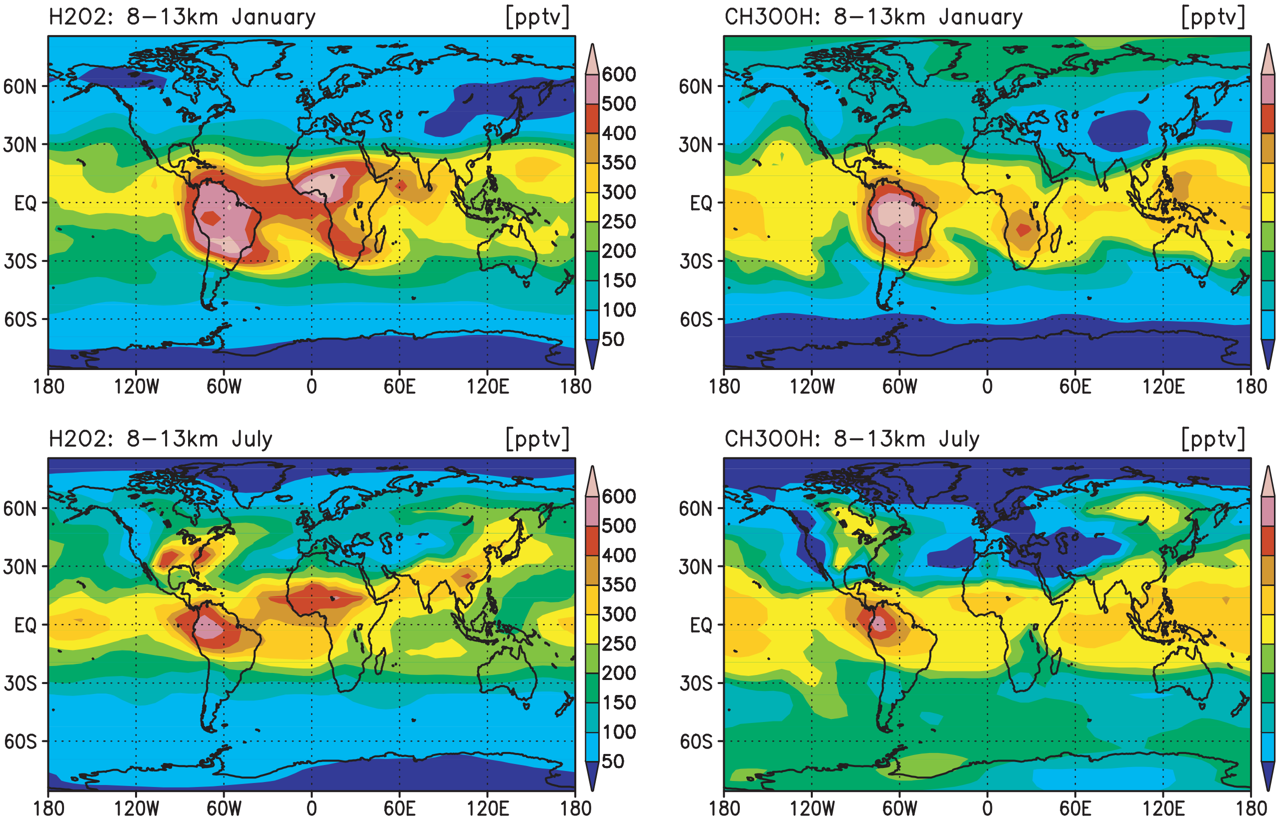

Figure 24. Calculated H_2O_2 (left) and CH_3OOH (right) distributions (pptv) in the upper troposphere (averaged over 8–13 km) for January and July.

H_2O_2. Over the China-Coast and the Philippine Sea regions, the model overestimates CH_3OOH in the middle-upper troposphere by a factor of ~2, with showing good agreement with the observations for H_2O_2 (Figure 26). This may indicate overestimation of methyl peroxy radical (CH_3O_2) and hence too strong formation of CH_3O_2 by the oxidation of NMHCs around these regions. In the tropical regions as Tahiti and Fiji (PEM-Tropics),the simulated profiles of CH_3OOH are well consistent with the observations, calculating mixing ratios of ~1 ppbv near the surface and 100–300 pptv in the upper troposphere. In the biomass-burning regions (TRACE-A), CH_3OOH in the upper troposphere is overestimated for the same reason as H_2O_2 (overestimation of HO_2 in the upper troposphere), though CH_3OOH in the lower-middle troposphere (500–1000 pptv) is well simulated.

5. Ozone

5.1. Distributions

[38] Figure 28 shows the surface O_3 distributions calculated for 4 different seasons. In January, high concentration of O_3 (50–60 ppbv) is calculated in India, owing to industrial emissions of O_3 precursors. High O_3 levels (~60 ppbv) are also seen in the biomass-burning region in North Africa. O_3 concentration in the midlatitudes ranges from 30 to 40 ppbv over the ocean in the Northern Hemisphere, as a result of longer chemical lifetime of O_3 in winter and transport from the stratosphere. The calculated stratospheric ozone distribution at the surface indicates a 40–50% contribution by stratospheric ozone to the surface O_3 abundance in the northern midlatitudes in January. In April, the O_3 chemistry is activated in the Northern Hemisphere. High O_3 levels (50–65 ppbv) are predicted in eastern Asia as India, China, and Japan, affected by intense UV radiation and surface emissions by industry and biomass burning. Ozone produced in eastern Asia and Japan is transported to the western Pacific. In July, O_3 is much abundant in the United States and in the central Eurasia including Europe, ranging from 50 to 70 ppbv. High O_3 level associated with biomass burning is seen in the western edge of Africa. The effect of biomass burning on the surface O_3 is clearly visible in October over South America and Africa (50–60 ppbv). The model calculates low concentrations of O_3 (10–15 ppbv) in Amazonia through a year, resulting from strong ozone destruction by biogenic NMHCs and from strong dry deposition (deposition velocities of ~1 cm s^{-1} in the model).

[39] Figure 29 compares the calculated seasonal cycle of surface O_3 with observations. The observations are mainly from *Oltmans and Levy* [1994]. The model well simulates the observed seasonal cycle of surface O_3 characterized by spring-maximum in the remote regions (Reykjavik, Mace Head, Bermuda, Mauna Loa, Samoa, Cape Grim) and summer-maximum in the polluted source regions (Höhenpeissenberg). The spring ozone peak at Bermuda is closely associated with the outflow from the United States in the model. Similarly, the peak in April at Mauna Loa is much related to the Asian outflow and to the transport of stratospheric ozone. For Cuiaba in the biomass-burning region in

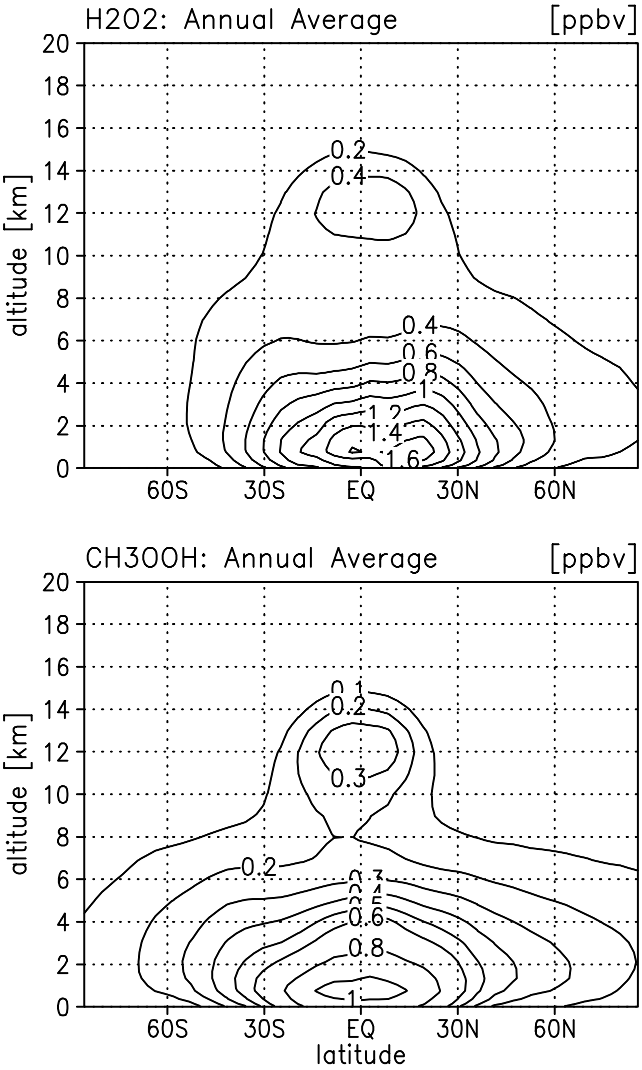

Figure 25. Zonal mean distributions (ppbv) of H_2O_2 and CH_3OOH in the annual average.

South America, the model well reproduces the observed seasonal cycle (September maximum) associated with biomass burning as well as CO (Figure 2). The simulated O_3 levels in Cuiaba are, however, somewhat higher than the observation through a year, maybe indicating the underestimation of O_3 deposition velocity, or the overestimation of soil NO_x emission around Cuiaba. Similar overestimation at this site is also found in a previous modeling study [*Roelofs and Lelieveld*, 2000]. For Samoa and Cape Grim, the model reproduces the observed seasonal variations associated with chemical lifetime of O_3 and transport from the stratosphere, though it slightly underestimates O_3 in June and July for Cape Grim.

[40] Figure 30 shows the zonal mean O_3 distributions calculated for January and July. In both seasons, the model calculates low O_3 levels (30–40 ppbv) in the tropics due to short chemical lifetime of O_3 and convective activity. In January, O_3 concentration is high in the middle-upper troposphere in the northern midlatitudes, associated with transport from the stratosphere. In July, the model calculates high O_3 concentrations in the Northern Hemisphere through much of the troposphere, reflecting intensive photochemical production of O_3 in summer. In the Southern Hemisphere, the model calculates low mixing ratios of ozone (10–20 ppbv) near the surface in January, and calculates higher ozone concentrations (25–35 ppbv) in July associated with transport from the stratosphere. In Figure 31, the seasonal variations of O_3 calculated at distinct altitudes are compared with the ozonesonde data compiled by *Logan* [1999]. The model generally well reproduces the observed seasonal cycles of O_3 at individual altitudes. At Resolute, the observed and the calculated O_3 at 200 hPa reach a peak (600–700 ppbv) in spring, associated with the stratospheric O_3 transport. Similar spring maximum is observed at 200 hPa over Höhenpeissenberg, underestimated by the model, though. O_3 seasonal variation at Höhenpeissenberg shows a summer maximum from 800 to 300 hPa, indicating considerable chemical production of O_3 over Europe in summer. At Kagoshima in the southern Japan, the model well captures the summertime minimum (rapid decrease in July and August) observed at 800 hPa. This minimum is associated with the shift in the air mass origin. The air mass at Kagoshima is maritime in summer and is continental in winter-spring, much influenced by the Asian outflow. At 300 and 200 hPa over Kagoshima, the model overestimates O_3 in winter by a factor of 2, indicating too much transport from the stratosphere. At 200 hPa over Hilo, the comparison similarly shows an overestimation of O_3 by the model in winter, though the observed spring maximum (60–70 ppbv) at 500 hPa is well captured by the model. In winter-spring, the model tends to overestimate O_3 in the upper troposphere in the low-mid latitudes, probably due to the relatively low horizontal resolution adopted in this simulation (T21, 5.6° × 5.6°). At Laverton in the Southern Hemisphere, the model captures the seasonal variation of ozone observed at 200 hPa, well reproducing the ozone peak (200–250 ppbv) in spring associated with the stratospheric ozone transport, though the model overestimates the observed ozone levels at 300 hPa.

[41] Additionally, we compare the calculated vertical profiles of O_3 with the observational data [*Logan*, 1999] in Figure 32. The calculated profiles are generally well consistent with the observations. At Hilo, the model overestimates O_3 in the upper troposphere especially in December–January–February (DJF) and March–April–May (MAM) as mentioned above. We note that both the observation and the model show high temporal variabilities (indicated by the standard deviations) in the upper troposphere at Hilo, in winter-spring (DJF and MAM). At Natal located in the eastern coast of Brazil, the model reproduces the increase in O_3 ($\sim$70 ppbv) in 800–300 hPa in September–October–November (SON) associated with biomass burning. The model, however, appears to slightly overestimate O_3 in the middle troposphere at Natal in MAM and JJA. At Samoa, the observed seasonal cycle of ozone profile showing maximum in spring (SON) is well simulated by the model. The model well captures also the decrease of O_3 observed in the tropical lower troposphere (Naha, Hilo, Natal, and Samoa) related to the trade wind inversion in the tropics [*Heikes et al.*, 1996; *Logan*, 1999].

[42] The calculated O_3 vertical profiles are also evaluated with the NASA GTE campaign data (Table 1) in Figure 33. In the Alaska (ABLE-3A), Ontario, and US-E-Coast regions,

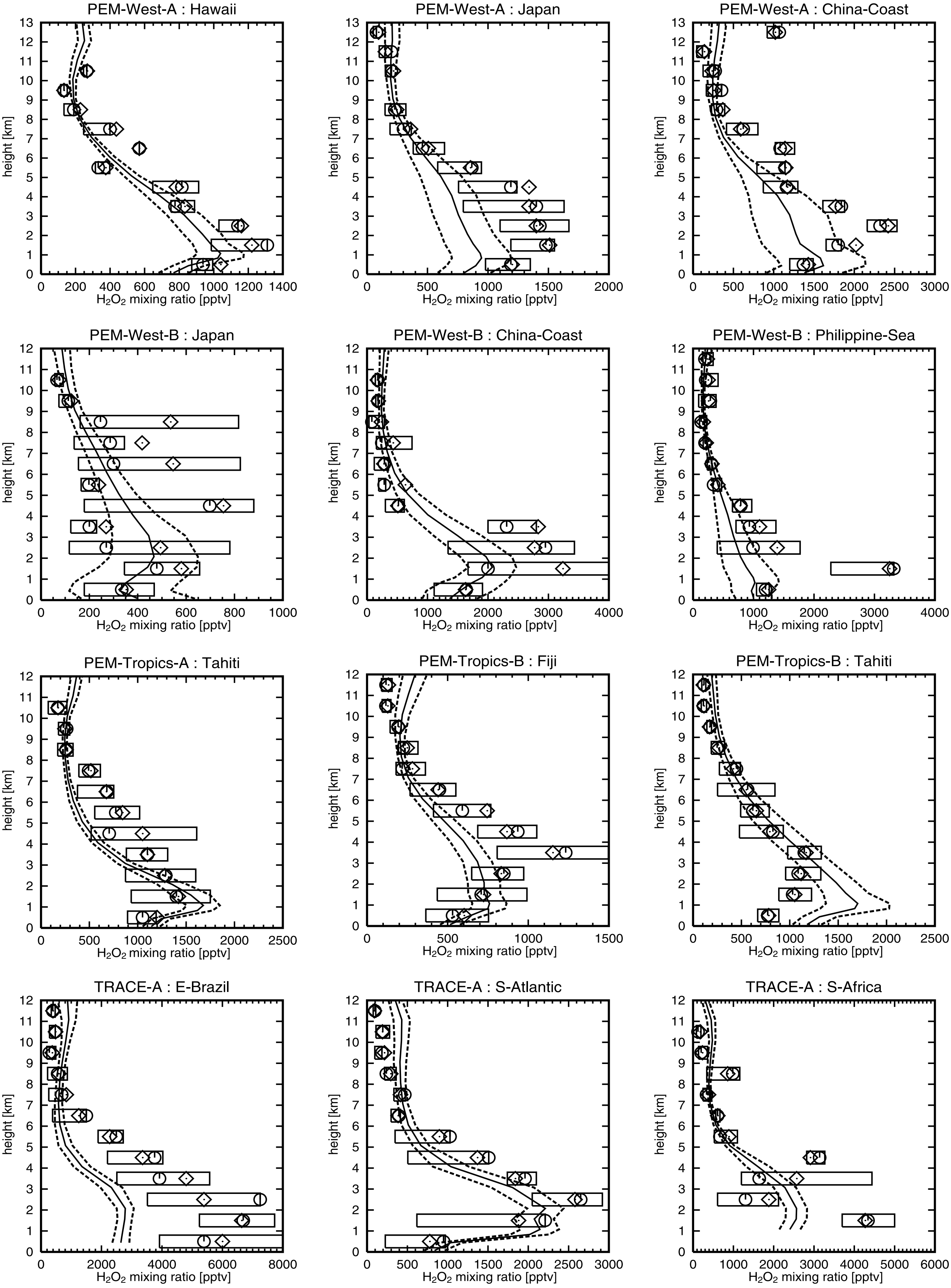

Figure 26. H_2O_2 vertical profiles observed and calculated over the regions of GTE campaigns (listed in Table 1). Solid lines and dashed lines show temporal mean and $\pm 1\sigma$ of the model calculation, respectively. The observations show mean (diamonds), median (circles), and inner 50% of the data (boxes).

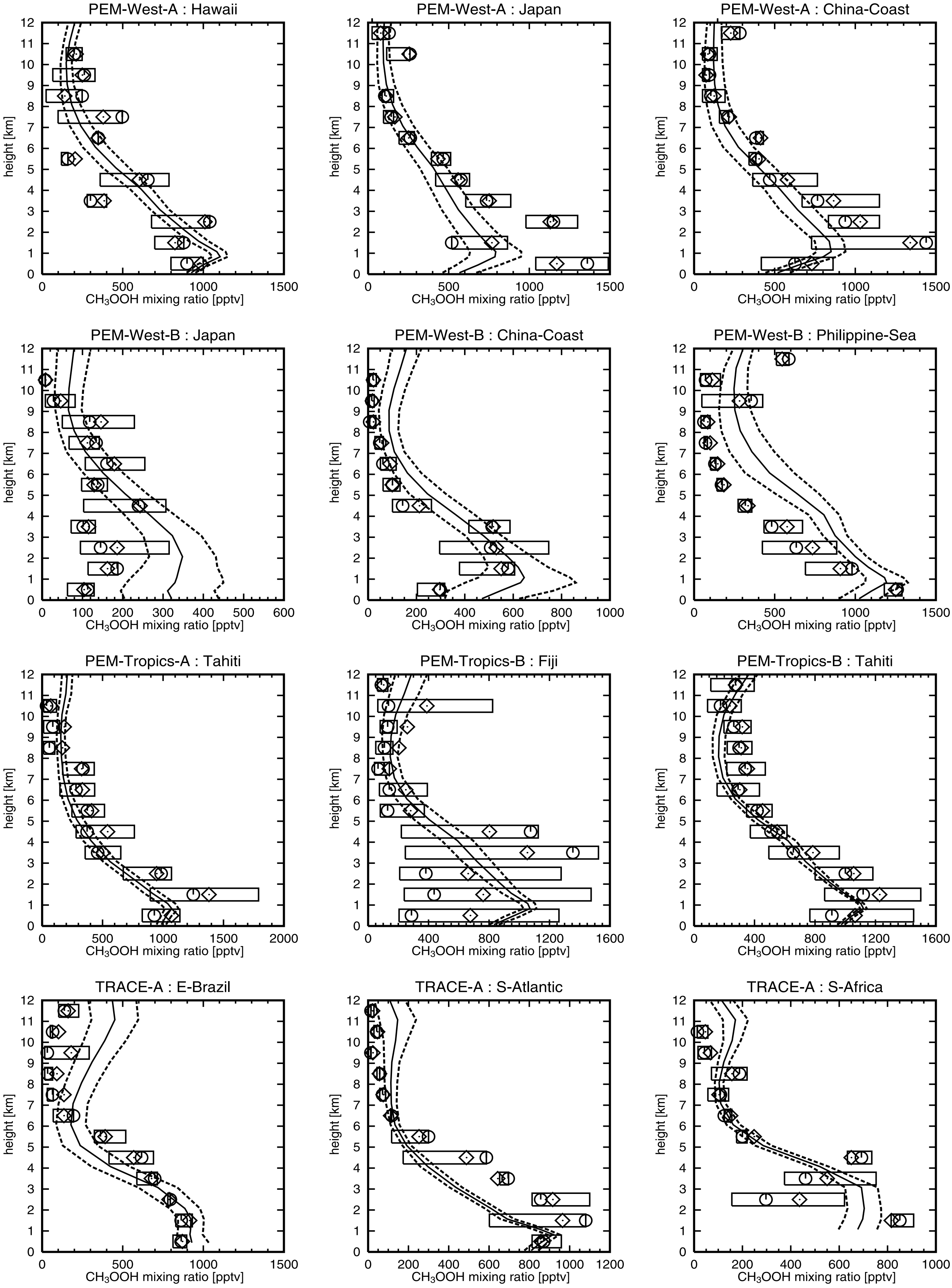

Figure 27. CH_3OOH vertical profiles observed and calculated over the regions of GTE campaigns (listed in Table 1). Solid lines and dashed lines show temporal mean and $\pm 1\sigma$ of the model calculation, respectively. The observations show mean (diamonds), median (circles), and inner 50% of the data (boxes).

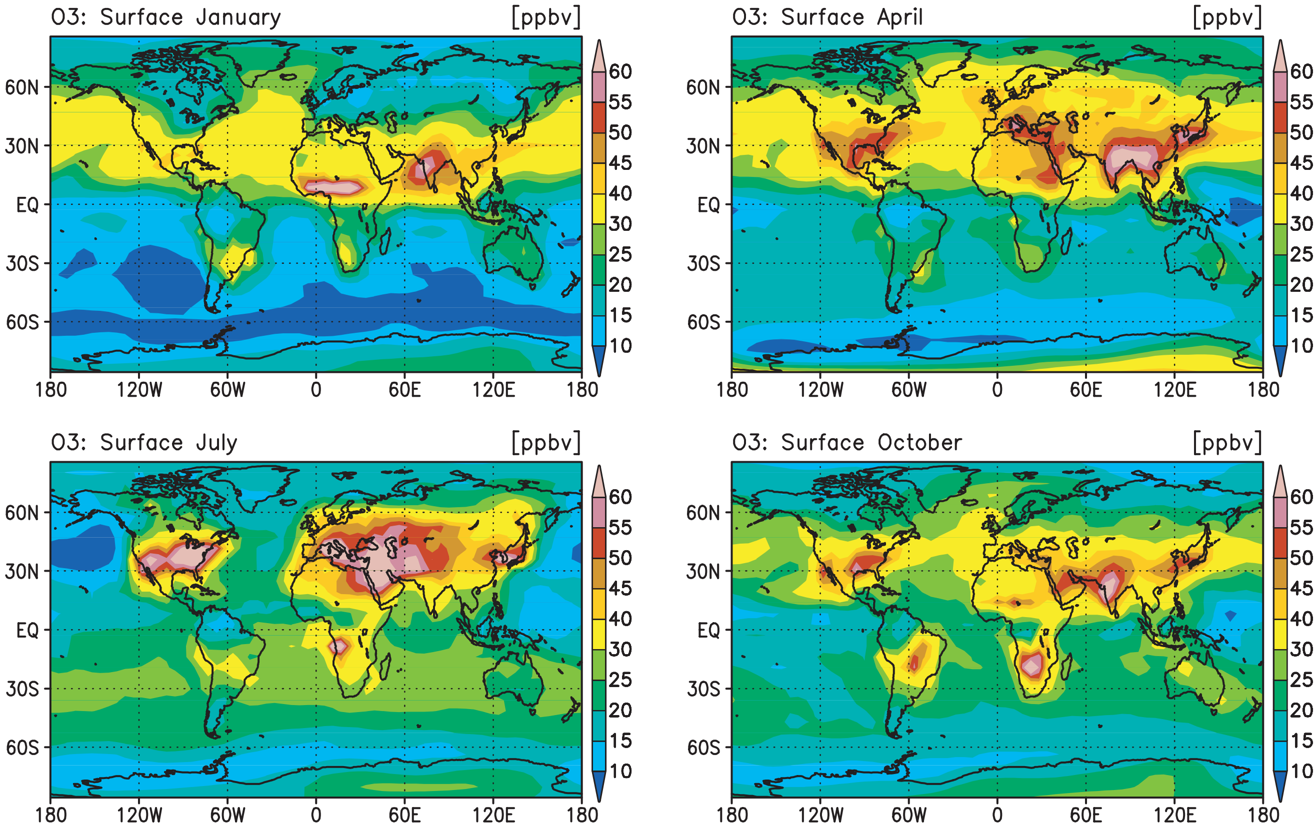

Figure 28. Calculated O_3 distributions (ppbv) at the surface for 4 distinct seasons.

the calculated profiles are well consistent with the campaign measurements. In the Japan region during PEM-West-B (February–March), a significant overestimation by the model is found in the middle-upper troposphere due to the overestimation of transport of stratospheric O_3 in the low-mid latitudes. A slight overestimation of ozone is also found in the middle troposphere over the China-Coast region (PEM-West-B). This overestimation by the model can be also attributed to the overestimation of the stratospheric ozone transport, since the photochemical production rates of ozone calculated for this region during PEM-West-B are well consistent with the box model calculation constrained by the observation (see Figure 36). In the tropical regions (PEM-Tropics-A), the model well simulates the observed profiles of O_3, capturing the rapid decrease in 0–3 km. For TRACE-A, the model reproduces the enhanced O_3 levels in the middle-upper troposphere due to biomass burning in South America and Africa. The model, however, underestimates the O_3 increase above 5 km over the E-Brazil region, probably caused by the underestimation of NO_x in the upper troposphere over this region (Figure 11). A rapid decrease in O_3 concentrations near the surface ($\sim$20 ppbv at the surface) is also well simulated by the model for the S-Atlantic region and the W-Africa-Coast region.

[43] Figure 34 shows the tropospheric column ozone (TCO) in Dobson units (DU) calculated for October. TCO calculated by the model shows the ozone column integrated from the surface to the physically defined tropopause in the model (defined as the lowest altitude at which the vertical temperature gradient is greater than −2 K/km). The model calculates TCO of 45–50 DU over the South Atlantic associated with biomass-burning emissions in South America and Africa as also seen in the comparison with the GTE campaign data (Figure 33, TRACE-A). *Fishman and Larsen* [1987] were the first attempt to derive the tropical tropospheric ozone distribution (in column total) by combining Stratospheric Aerosol and Gas Experiment (SAGE) stratospheric column ozone with total ozone mapping spectrometer (TOMS) total ozone measurements. Their study, though poor data sampling of SAGE, revealed an anomalous zonal pattern in tropospheric column ozone in the tropics (zonal wave number 1 pattern) with a peak in the south Atlantic and a minimum around the western Pacific (around 140°E to the date line). This characteristic pattern in the tropical ozone distribution is also captured by recent studies using more refined methods [*Kim et al.*, 1996; *Ziemke et al.*, 1998; *Thompson and Hudson*, 1999]. Their studies and most of recent studies generally conclude that the zonal wave number 1 structure in the tropical column ozone is likely to be related to either meteorological conditions in the tropics (e.g., Walker circulation) or photochemical production of ozone associated with biomass burning and biogenic emissions of ozone precursors [e.g., *Fishman et al.*, 1996; *Thompson et al.*, 1996]. The model appears to capture the zonal wave number 1 pattern in the tropical ozone distribution well, calculating a maximum (45–50 DU) over the South Atlantic with a minimum (15–20 DU) over the western Pacific in October, consistent with *Kim et al.* [1996], *Ziemke et al.* [1998], among others. The model simulation shows that the NO_x production due to lightning activity

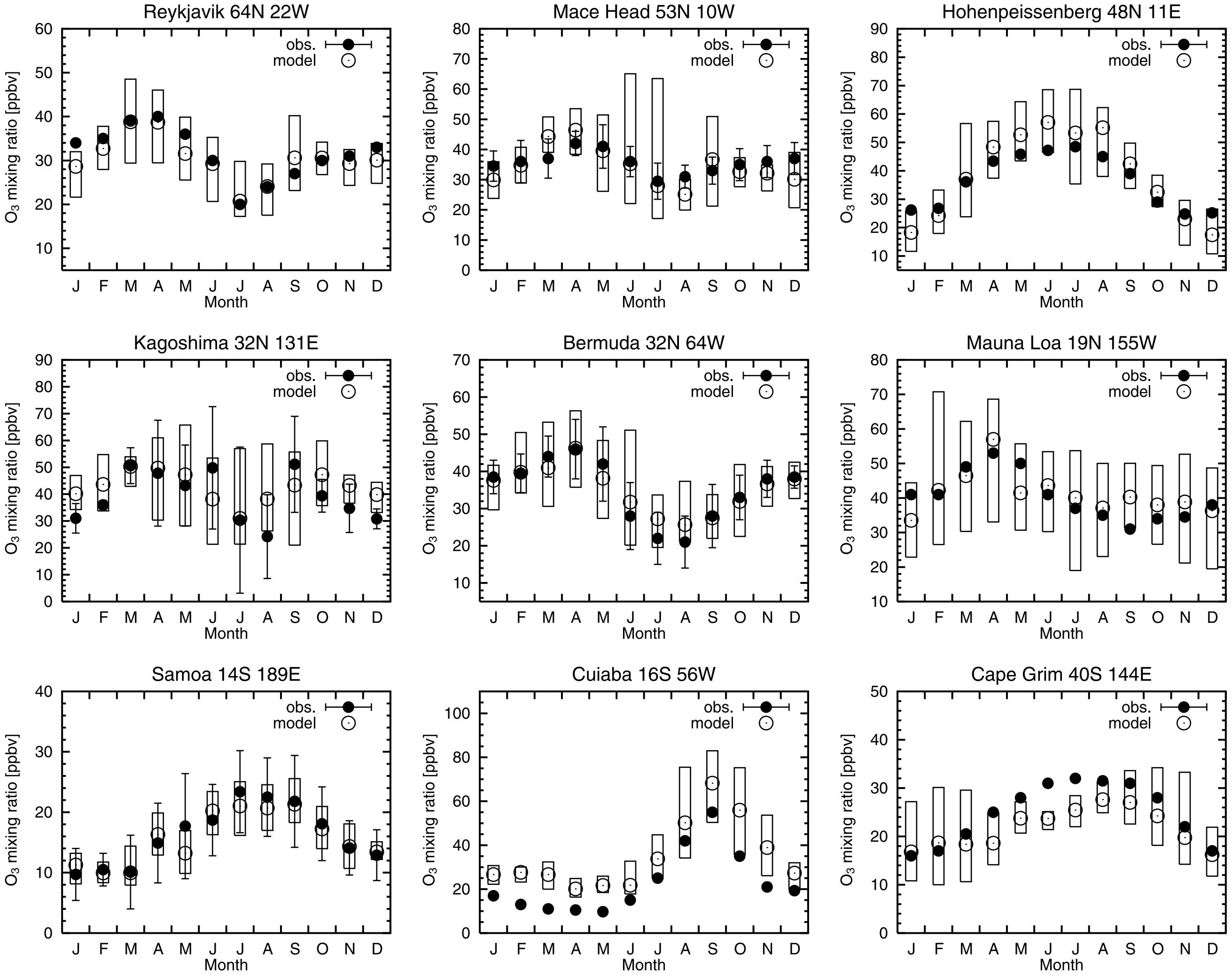

Reykjavik 64N 22W

Mace Head 53N 10W

Hohenpeissenberg 48N 11E

Kagoshima 32N 131E

Bermuda 32N 64W

Mauna Loa 19N 155W

Samoa 14S 189E

Cuiaba 16S 56W

Cape Grim 40S 144E

Figure 29. O_3 seasonal variations observed (solid circles) and calculated (open circles with boxes showing the range) at the surface for several sites. Measurements are from *Oltmans and Levy* [1994], *Kirchhoff et al.* [1989] (for Cuiaba), and *Logan* [1999] (for Kagoshima).

over South America and Africa is also a key factor of the simulated ozone enhancement over the South Atlantic and Africa in the biomass-burning season (September–October) as suggested by *Thompson et al.* [1996] and *Fishman et al.* [1996]. The CHASER model has been used in a simulation of the tropical tropospheric ozone changes during the 1997–1998 El Niño event [*Sudo and Takahashi*, 2001]. It reproduces the observed large-scale ozone changes in the tropics due to the changes in convection, wind circulation, and water vapor during the El Niño.

5.2. Budget

[44] There are two kinds of sources for tropospheric ozone. One is the transport of ozone associated with the stratosphere-troposphere exchange (STE), and the other is the in-situ photochemical production in the troposphere due to the reaction of NO with peroxy radicals and the subsequent photolysis of NO_2. Loss of tropospheric ozone is mainly by photochemical destruction due to the reaction of atomic oxygen (singlet) $O(^1D)$ with water vapor ($O(^1D) + H_2O$) and the subsequent reactions (i.e., $O_3 + OH$ and $O_3 + HO_2$), and by dry deposition at the surface. Transport of ozone to the stratosphere associated with the STE is also loss of tropospheric ozone.

[45] Figure 35 shows the distributions of the 24-hour averaged net chemical production $P(O_y)-L(O_y)$ calculated at the surface and in the upper troposphere (8–13 km average) for January and July. O_y is the conventionally defined odd oxygen family and indicates $O_3 + O(^1D) + NO_2 + 2NO_3 + 3N_2O_5$ + PAN + MPAN + $2HNO_3 + HNO_4$ + ISON + NALD in this simulation (ISON = isoprene nitrates, NALD = nitrooxy acetaldehyde, see *Sudo et al.* [2002]). The budget of O_y is almost identical to that of ozone. The model calculates intensive ozone production in the polluted areas at the surface for both seasons. In January, ozone production rates of 30–50 ppbv/d are calculated over North Africa, associated with biomass burning. The model predicts relatively strong ozone production (6–15 ppbv/d) in the southern United States and eastern Asia, and also calculates positive production (0–2 ppbv/d) in the northern high latitudes (45–60°N) in spite of reduced UV radiation. In July, the net ozone production at the surface is intensive

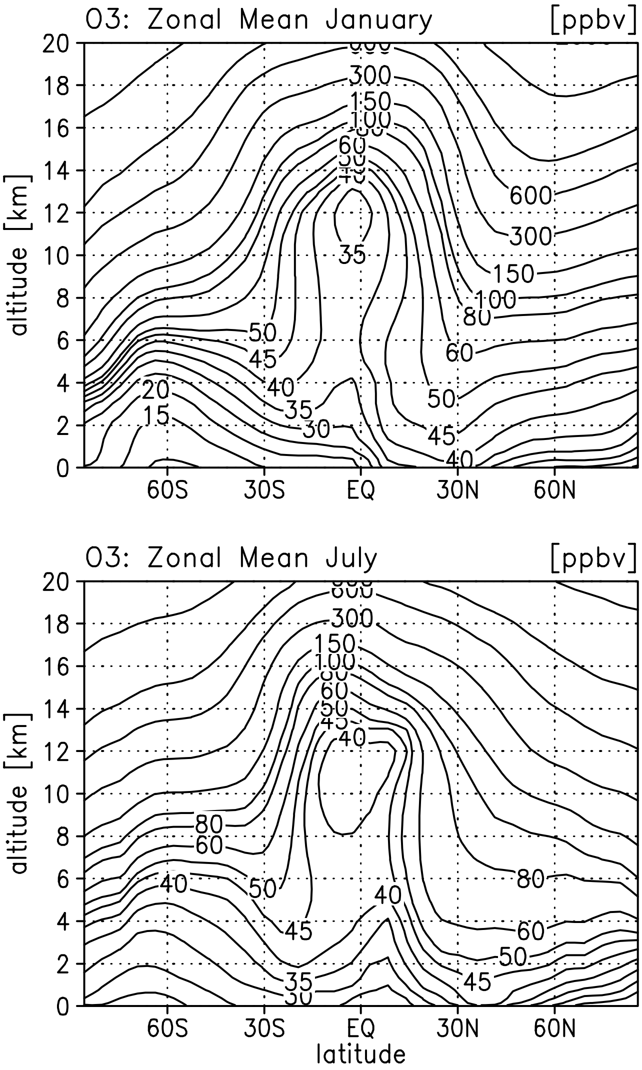

Figure 30. Zonally averaged ozone mixing ratios (ppbv) calculated for January and July.

in the eastern United States, Europe, and eastern Asia (30–70 ppbv/d) owing to industrial emissions of ozone precursors. The net ozone production over the ocean is generally negative (ozone destruction). In the upper troposphere, the model calculates positive net ozone production through much of the low-mid latitudes. In January, high ozone production rates (3–7 ppbv/d) are calculated over South America, Africa, and the northern Australia, due to lightning NO_x and convective transport of biogenic emissions of NMHCs. Strong ozone production (~8 ppbv/d) over North Africa is associated with convective transport of biomass-burning emissions. The net ozone production calculated for July also displays the effect of surface emissions, convective transport, and lightning NO_x on the ozone budget in the upper troposphere. Intensive ozone production (8–10 ppbv/d) is calculated over the southern United States and eastern Asia extending over the western Pacific including Japan (2–4 ppbv/d).

[46] Ozone production and loss rates have been calculated for several of the aircraft campaigns, using photochemical box (0-dimensional) models constrained by observations [e.g., *Crawford et al.*, 1996, 1997; *Schultz et al.*, 1999]. We compare the calculated ozone production rates with these observation-derived ozone production rates. Figure 36 shows the vertical profiles of the ozone chemical production $P(O_y)$ and the net chemical production $P(O_y)$-$L(O_y)$ derived from the GTE campaign measurements [*Crawford et al.*, 1996, 1997] and calculated by CHASER. The values show the 24-hour averaged ozone production and net production. In Hawaii (PEM-West-A), the calculated $P(O_y)$ ranges from 0.5 to 1.5 ppbv/d, well within the range of the constrained box model calculation (BMC, in the following). The calculated net ozone production $P(O_y)$-$L(O_y)$ is also consistent with the BMC, well reproducing the net ozone production (0–1.5 ppbv/d) above ~7 km. In the Japan region during PEM-West-A (September–October), the model well simulates the ozone production (1.5–3 ppbv/d) in the free troposphere, and also reproduces the decrease in the net production below 7 km (net ozone destruction) reflecting the shorter lifetime of ozone in the lower troposphere. The ozone production near the surface is, however, overestimated by a factor of 6. During the PEM-West-B expedition (February–March), the model calculates vertical profiles consistent with the BMC over the Japan region below8 km for both $P(O_y)$ and $P(O_y)$-$L(O_y)$. The model does not capture the high rates of ozone production and net production (~2 ppbv/d) in the upper troposphere above 8 km. In the China-Coast region, the model well simulates profiles of $P(O_y)$ and $P(O_y)$-$L(O_y)$, calculating high net ozone production rates (~2 ppbv/d) in the upper troposphere. The BMC data shows higher production rates (20–25 ppbv/d) near the surface (below 1 km) than CHASER (10–15 ppbv/d). In the Philippine Sea region, the net ozone production appears to be underestimated by 1–2 ppbv/d, though the calculated ozone production $P(O_y)$ is well consistent with the BMC (1–2 ppbv/d). This may indicate the overestimation of water vapor leading to overestimation of ozone loss over this region. Over the source regions of biomass burning (E-Brazil and the S-Africa), the high production rates (3–5 ppbv/d) in the upper troposphere derived by the BMC are also reproduced by CHASER. The profiles of ozone production $P(O_y)$ show almost constant rates (3–5 ppbv/d) in the free troposphere above 3 km with high rates in the boundary layer (15–50 ppbv/d). Both the BMC and CHASER calculations display steep decrease in the net ozone production with altitude in the boundary layer and increase in the free troposphere, with showing slight negative rates above the top of boundary layer (3–5 km). Over the S-Atlantic region, ozone production rates calculated in the upper troposphere (~2 ppbv/d) are consistent with the BMC. The net ozone production rates in 2–6 km altitudes are, however, overestimated by CHASER by 1–2 ppbv/d, caused principally by the overestimation of ozone production in 2–4 km, and possibly by the underestimation of water vapor over the South Atlantic (not verified).

[47] In Table 5, the global annual budget of tropospheric ozone (O_y) calculated by the model is presented. The model calculates a global ozone chemical production of 4895 TgO_3/yr (62% in the Northern Hemisphere). The reactions of NO with HO_2 and CH_3O_2 are main production, contributing to the total ozone production for 63% and 23%, respectively. The remainder (14% of the total ozone production) is due to the reactions of NO with peroxy radicals formed by the

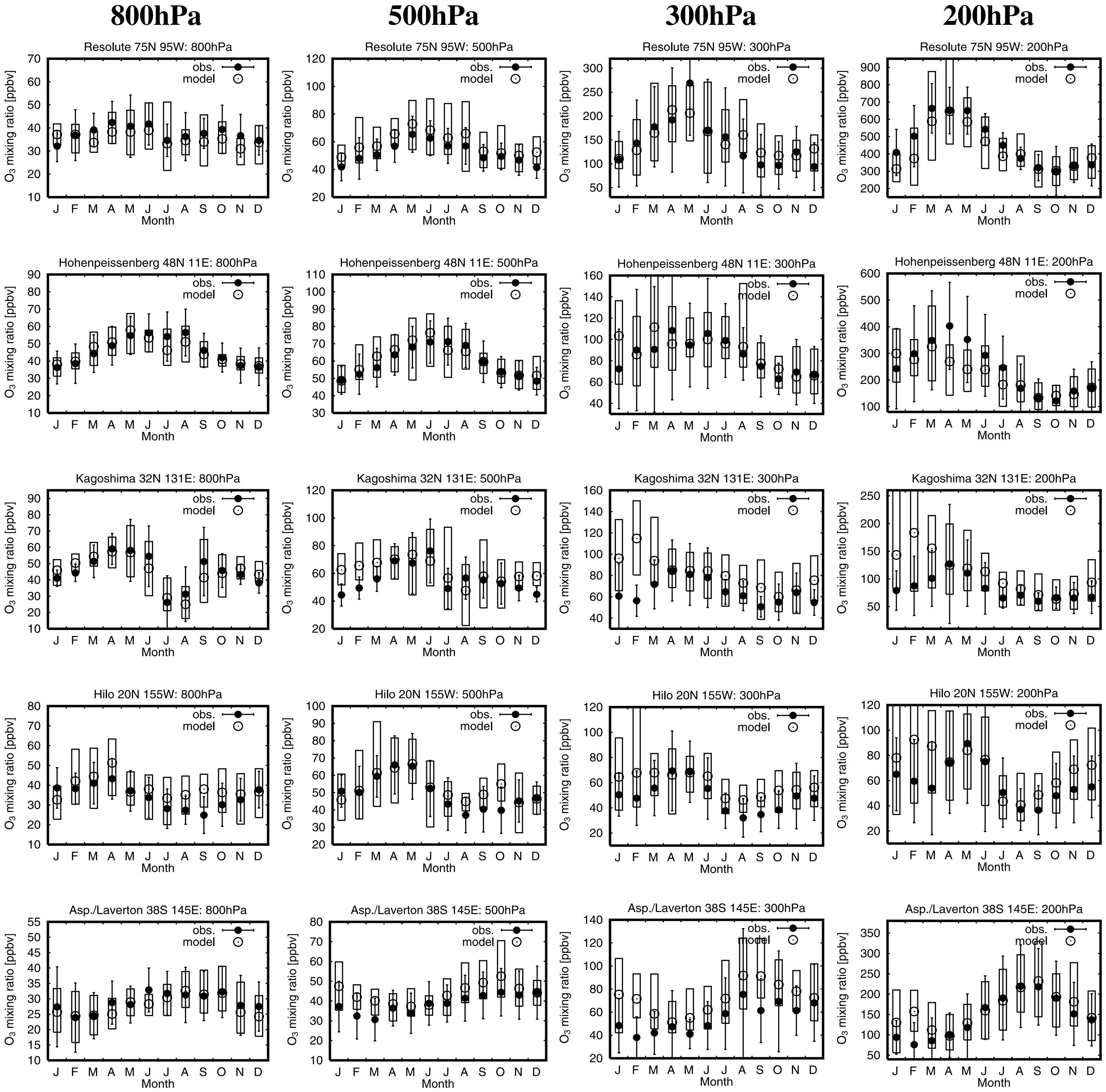

Figure 31. O_3 seasonal variations observed (solid circles) and calculated (open circles with boxes showing the range) at different elevations. Observations are taken from *Logan* [1999].

oxidation of NMHCs. The reaction of HO_2 with CH_3COO_2 also makes a contribution to the ozone production in the model, though slightly. The ozone production due to the reactions of NO with $MACRO_2$ (peroxy radical from the methacrolein oxidation) and with CH_3COO_2 (160 and 204 TgO_3/yr, respectively) might be overestimated, since the chemical scheme for the oxidation of isoprene and terpenes does not consider the heterogeneous reaction (loss) of methacrolein on aerosols as included by *Müller and Brasseur* [1995] and *Brasseur et al.* [1998]. In addition, heterogeneous reactions (uptake) of HO_2 and peroxy radicals (RO_2) formed by oxidation of isoprene and terpenes [e.g., *Walcek et al.*, 1997; *Horowitz et al.*, 1998; *Jacob*, 2000] may reduce the O_3 production in polluted areas and hence the global O_3 production. The ozone chemical production calculated in this simulation, 4895 TgO_3/yr, is on the higher side of the range suggested by previous modeling studies (4550 TgO_3/yr [*Müller and Brasseur*, 1995]; 3609 TgO_3/yr [*Lelieveld and van Dorland*, 1995]; 3206 TgO_3/yr [*Roelofs and Lelieveld*, 1995]; 3415 TgO_3/yr [*Roelofs et al.*, 1997]; 4300 TgO_3/yr [*Wang et al.*, 1998b]; 3018 TgO_3/yr [*Hauglustaine et al.*, 1998]; 4375 TgO_3/yr [*Roelofs and Lelieveld*, 2000]). The global chemical loss of tropospheric ozone is calculated as 4498 TgO_3/yr (59% in the Northern Hemisphere), contributing for 82% to the total ozone sink (5488 TgO_3/yr). The chemical loss of ozone is mainly by $O(^1D) + H_2O$ (55%), $O_3 + HO_2$ (28%), and $O_3 + OH$ (14%) in the model. The ozone loss by the reactions with NMHCs (as C_2H_4, C_3H_6, isoprene, and terpenes) is important for the ozone budget in the boundary layer over the tropical rain forest (especially in

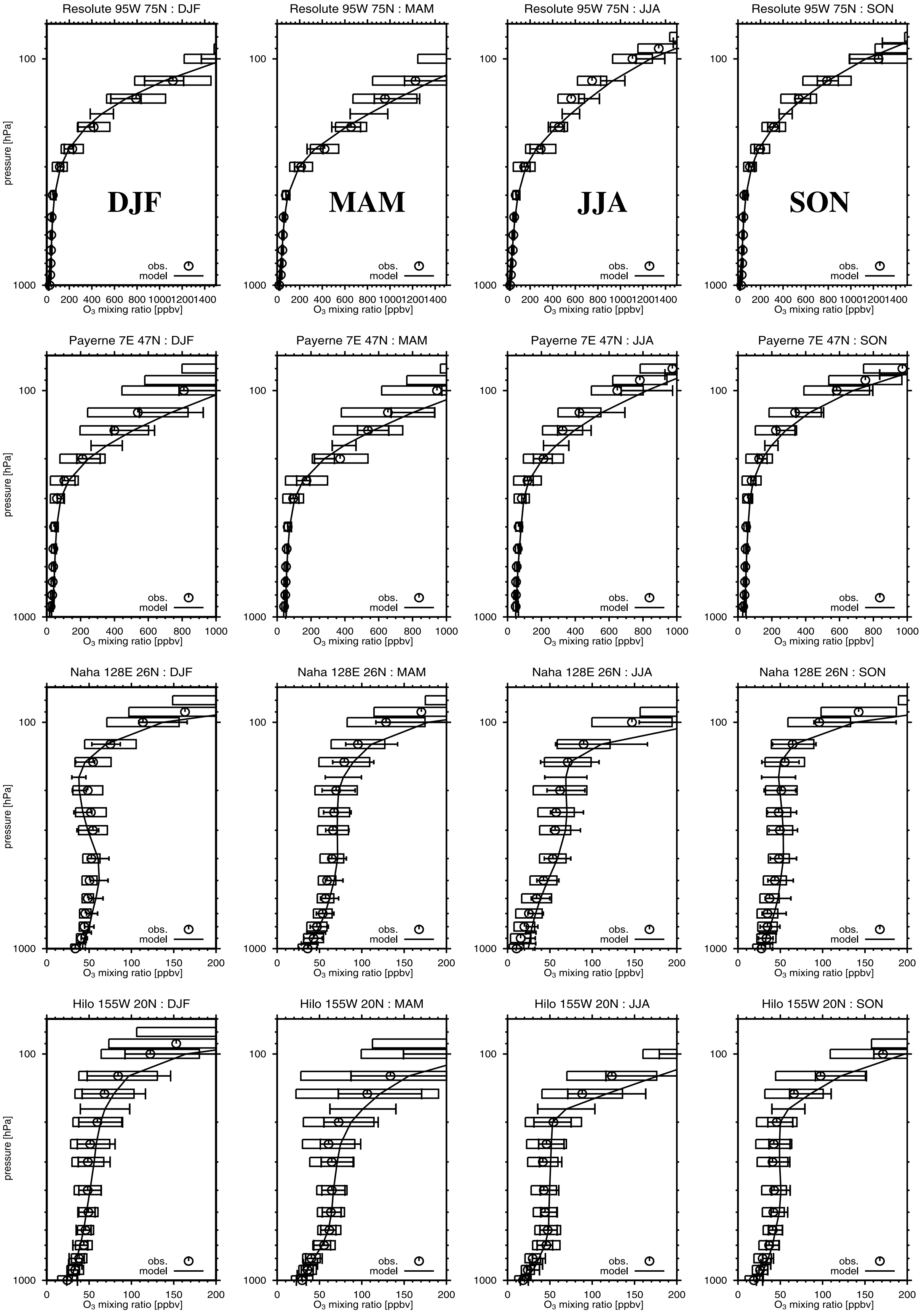

Figure 32. O_3 vertical profiles observed (open circles) and calculated (solid lines with ±σ bars) at several stations for 4 different seasons. Boxes show the standard deviations of observations. Observations are taken from *Logan* [1999].

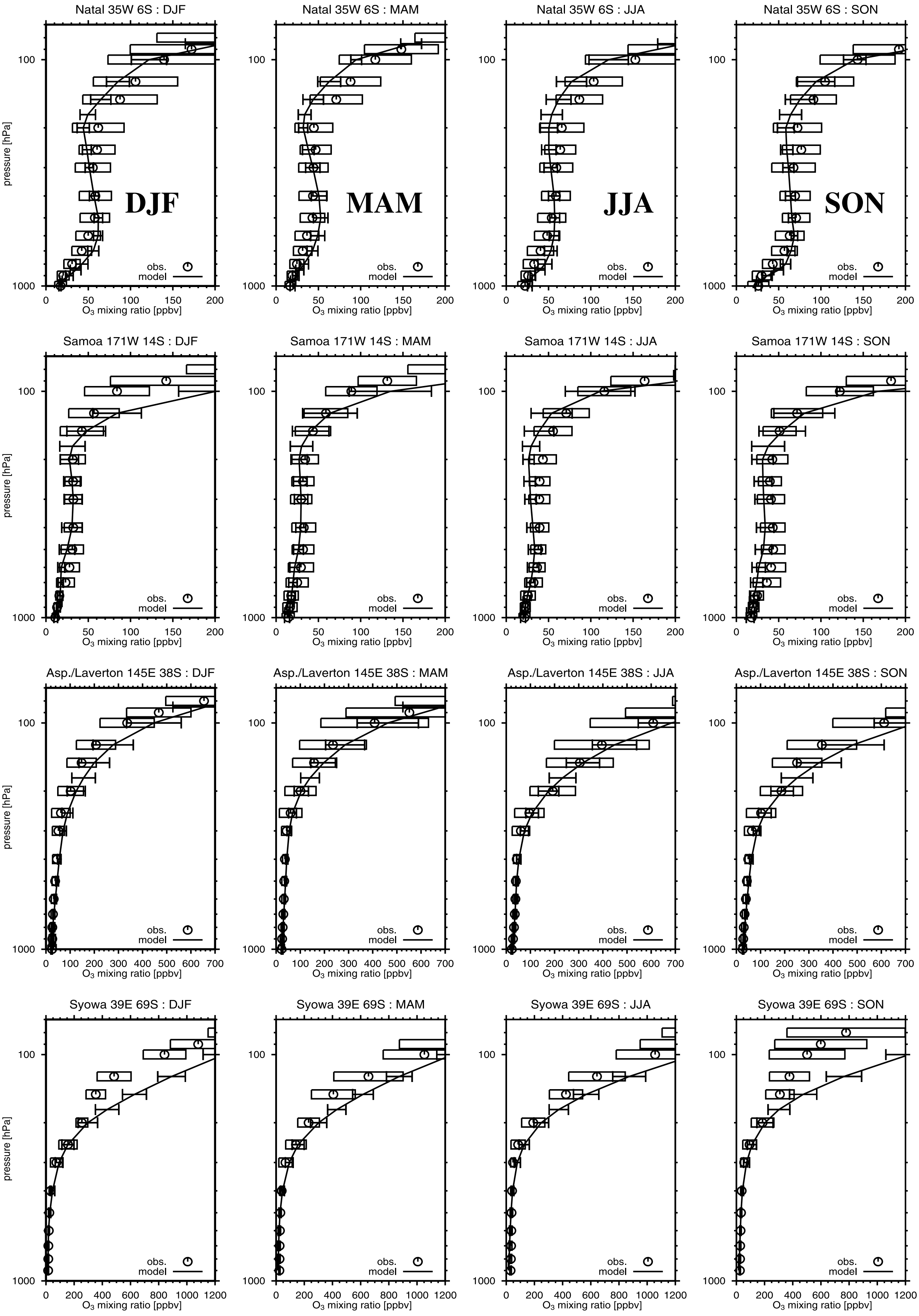

Figure 32. (continued)

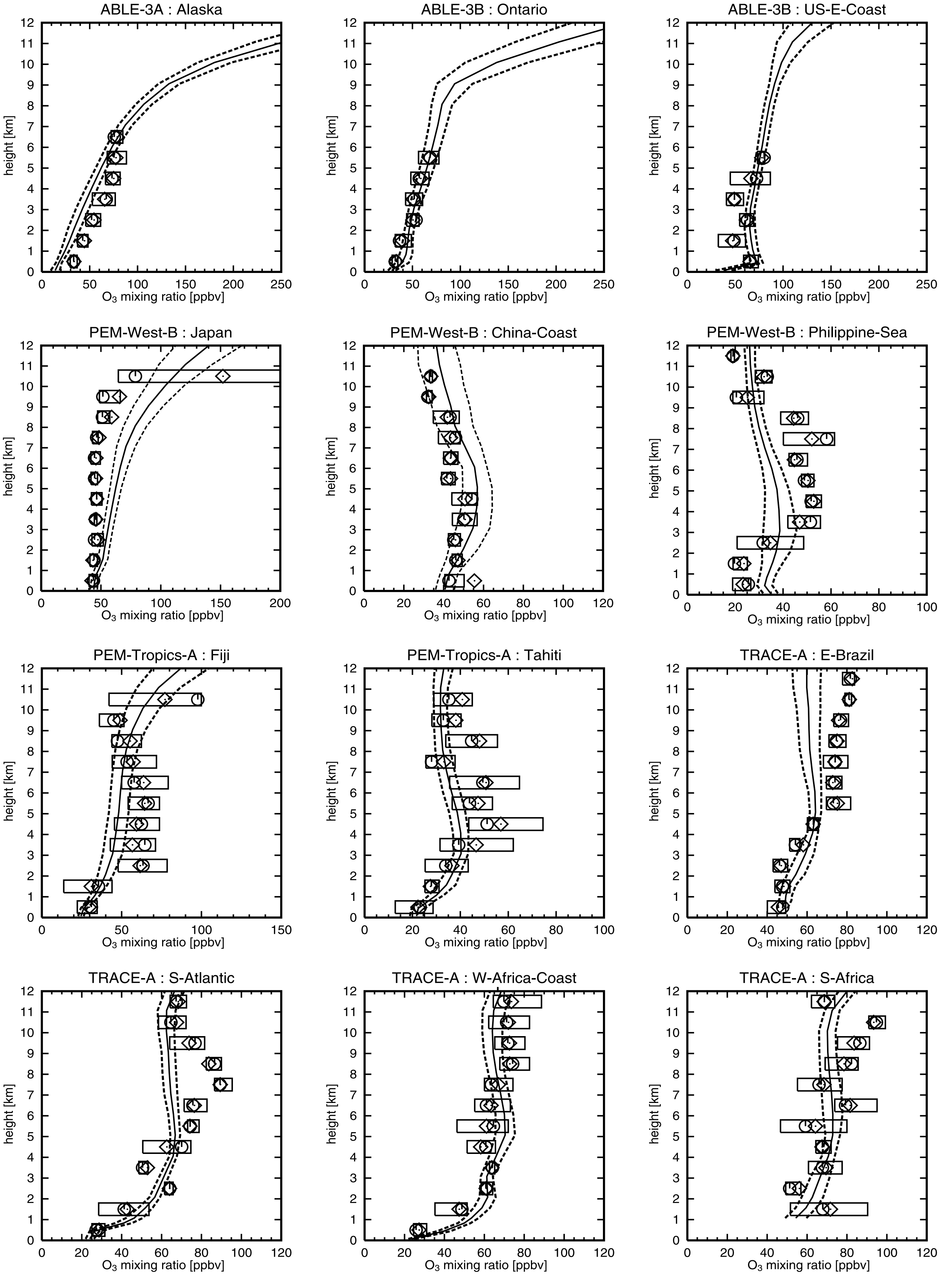

Figure 33. O_3 vertical profiles observed and calculated over the regions of GTE campaigns (listed in Table 1). Solid lines and dashed lines show temporal mean and ±1σ of the model calculation, respectively. The observations show mean (diamonds), median (circles), and inner 50% of the data (boxes).

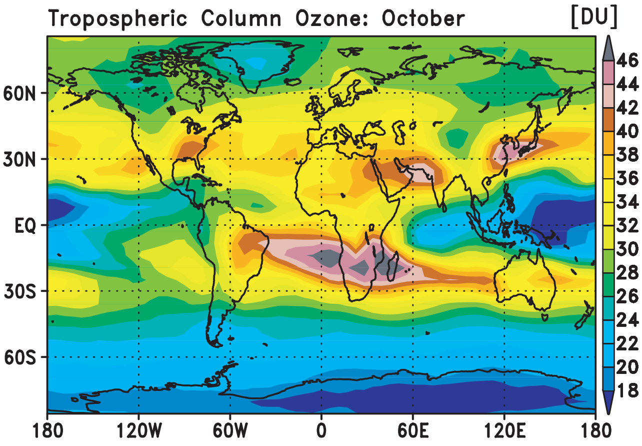

Figure 34. Tropospheric column ozone (DU) calculated for October.

Amazonia and Africa) where biogenic emissions of NMHCs are abundant. Consequently, the calculated net ozone chemical production (difference between the production and the loss) is 397.2 TgO_3/yr (93% in the Northern Hemisphere). The net ozone production is also highly variable according to individual studies, ranging from 73 TgO_3/yr [*Roelofs and Lelieveld*, 2000] to 550 TgO_3/yr [*Müller and Brasseur*, 1995]. Although the reason for this variability is unclear, it is attributed partly to the difference in the model domain (i.e., tropopause height) considered for the budget analysis in the models. The net ozone production calculated for the Northern Hemisphere shows two peaks in late spring (April–May, reaching 500 TgO_3/yr) and late summer (August–September, 400–500 TgO_3/yr). In the Southern Hemisphere, the calculated net ozone production is positive during the dry season including the biomass-burning season (June–October, 100–200 TgO_3/yr). Dry deposition at the surface is also a sink for tropospheric ozone and calculated as 990 TgO_3/yr (65% in the Northern Hemisphere) by the model. This value is somewhat higher than the values suggested by recent studies (890 TgO_3/yr [*Wang et al.*, 1998b], 898 TgO_3/yr [*Hauglustaine et al.*, 1998], 668 TgO_3/yr [*Roelofs and Lelieveld*, 2000]), probably resulting from the differences in the abundance of ozone. The net ozone flux associated with the Stratosphere-Troposphere Exchange (STE) is estimated at 593.2 TgO_3/yr in this simulation, contributing for 11% to the total ozone source. This value appears to be in the middle of the range of previous studies (ranging from 391 TgO_3/yr [*Hauglustaine et al.*, 1998] to 846 TgO_3/yr [*Berntsen and Isaksen*, 1997]). The tropospheric ozone burden is calculated as 322 TgO_3 (58% in the Northern Hemisphere). The photochemical lifetime of ozone is estimated at 25 days in the global and annual average. Slightly longer lifetime is found in the Southern Hemisphere (27 days), reflecting less abundant HO_x concentration in the Southern Hemisphere (see section 4). In both hemispheres, the averaged photochemical lifetime of ozone is about 40 days in winter and about 15 days in summer. The photochemical lifetime of ozone calculated in the tropical boundary layer is generally in the range of 6–15 days, with

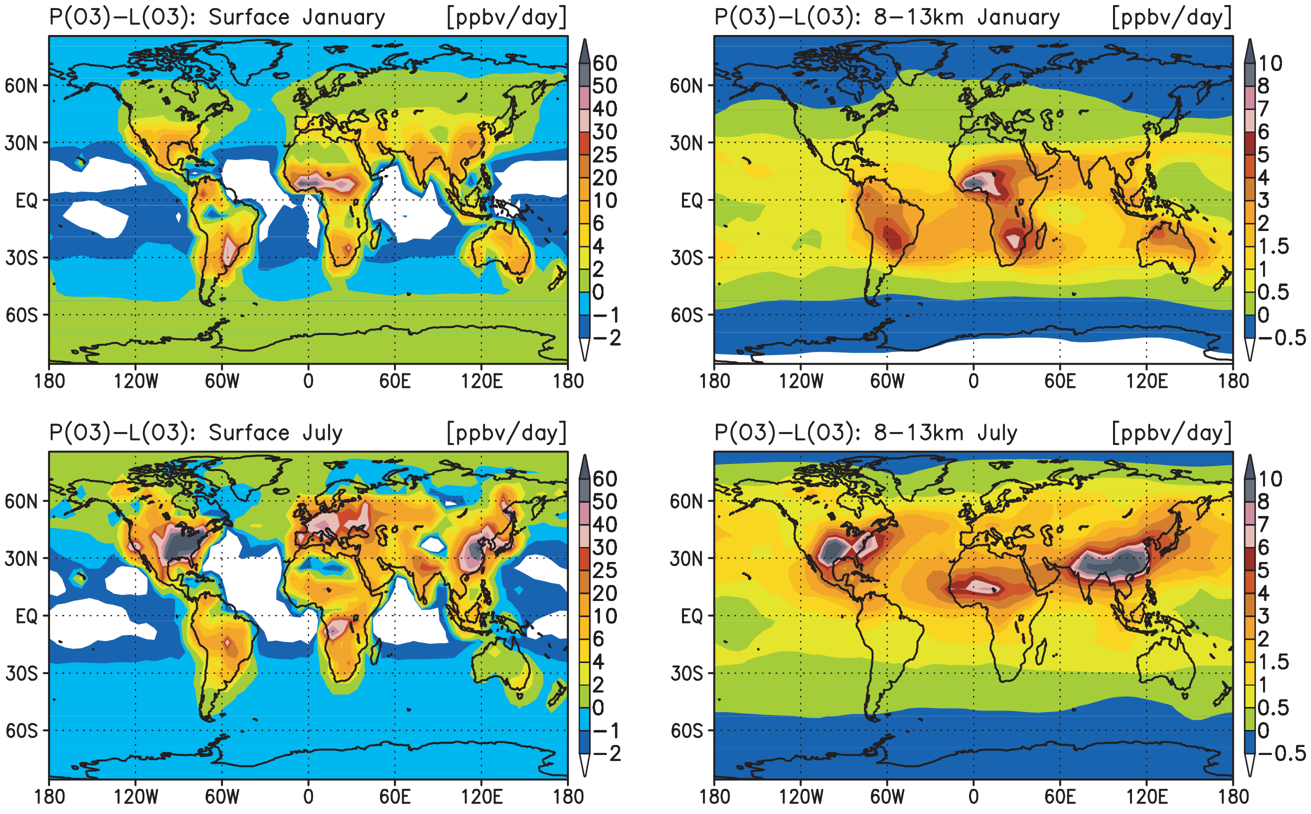

Figure 35. Calculated distributions of the net chemical production of ozone (ppbv/d) at the surface (left) and in the upper troposphere (8–13 km) (right) for January and July.

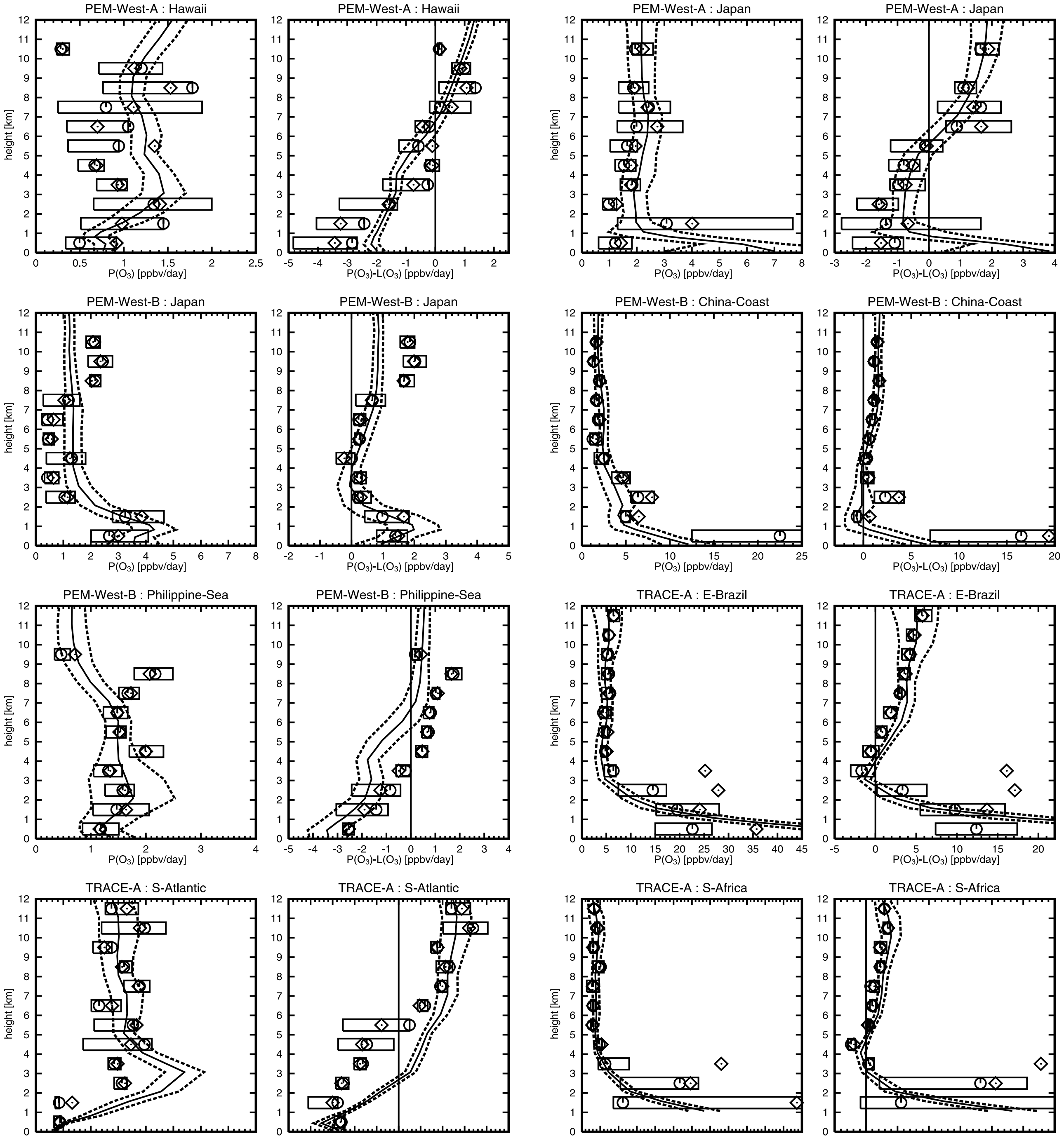

Figure 36. Vertical profiles of the ozone production $P(O_3)$ and the net production $P(O_3)$-$L(O_3)$ derived from observations and calculated by CHASER over the regions of GTE campaigns (listed in Table 1). Solid lines and dashed lines show temporal mean and $\pm 1\sigma$ of the model calculation, respectively. The observations show mean (diamonds), median (circles), and inner 50% of the data (boxes).

showing anomalously short lifetimes of 2–3 days over the tropical rain forests like Amazonia associated with the strong ozone destruction by the reactions with NMHCs.

6. Summary and Conclusions

[48] We have presented and evaluated results from a global chemical model CHASER. CHASER is driven online by the meteorological field generated by a atmospheric general circulation model (AGCM). The model simulates the major processes involving the tropospheric photochemistry such as large-scale and subgrid-scale transport, emissions, deposition, and chemical transformations. The chemical component of CHASER includes 25 photolytic reactions and 88 chemical reactions. Oxidations of ethane (C_2H_6), propane (C_3H_8), ethene (C_2H_4), propene (C_3H_6),

Table 5. Global Budget of Tropospheric O_y Calculated by CHASER[a]

	Global	NH	SH
Sources	5488.0		
Net STE[b]	593.2		
Chemical production	4894.8	3027.7	1867.1
$HO_2 + NO$	3080.2		
$CH_3O_2 + NO$	1147.9		
$C_2H_5O_2 + NO$	36.7		
$C_3H_7O_2 + NO$	6.2		
$CH_3COCH_2O_2 + NO$	18.4		
$HOC_2H_4O_2 + NO$	33.8		
$HOC_3H_6O_2 + NO$	11.7		
$CH_3COO_2 + NO$	204.2		
$CH_3COO_2 + HO_2$	55.1		
ISO_2[c] + NO	140.5		
$MACRO_2$[d] + NO	160.1		
Sinks	−5488.0	−3304.6	−2183.4
Dry deposition	−990.4	−646.9	−343.5
Chemical loss	−4497.6	−2657.7	−1839.9
$O(^1D) + H_2O$	−2478.0		
$O_3 + HO_2$	−1280.1		
$O_3 + OH$	−642.9		
$CH_4 + O(^1D)$	−1.0		
$C_2H_4 + O_3$	−5.6		
$C_3H_6 + O_3$	−5.4		
$C_5H_8 + O_3$	−42.2		
$MACR + O_3$	−20.1		
$C_{10}H_{16} + O_3$	−22.3		
Net chemical production	397.2	370.0	27.2
O_y chemical lifetime, days	25	24	27
Burden, TgO_3	322	187	135

[a] Values (in TgO_3/yr) are calculated for the region below the tropopause height in the model.

[b] Stratosphere-troposphere exchange (net O_3 flux from the stratosphere).

[c] Peroxy radicals from isoprene (C_5H_8) + OH.

[d] Peroxy radicals from methacrolein (MACR) + OH.

isoprene (C_5H_8), and terpenes ($C_{10}H_{16}$, etc.) are included explicitly. Degradation of other NMHCs is represented by the oxidation of a lumped species named other nonmethane volatile organic compounds (ONMV) as in the IMAGES model [*Müller and Brasseur*, 1995] and the MOZART model [*Brasseur et al.*, 1998]. The scheme for the isoprene oxidation we adopted is based on a condensed isoprene oxidation scheme of *Pöschl et al.* [2000] derived from the Master Chemical Mechanism (MCM, Version 2.0) [*Jenkin et al.*, 1997]. Terpenes oxidation is largely based on the work of *Brasseur et al.* [1998]. Heterogeneous reactions on aerosols (e.g., conversion of N_2O_5 to HNO_3) are not considered in this simulation. In this paper, we have presented results from a climatological simulation by CHASER.

[49] The model simulates the observed seasonal cycle of surface CO well, reproducing the spring maximum observed in remote sites. The seasonal variation of CO at Cuiaba (in the biomass-burning region of South America) is also reproduced well by simulating the seasonal cycle of biomass-burning emissions using hot spot (fire distribution) data derived from satellites. The calculated CO level in the northern high latitudes is, however, underestimated. The global budget of tropospheric CO calculated by CHASER shows a significant contribution by the oxidation of methane and NMHCs to the total source for CO (56% of 2801 TgCO/yr). The vertical distributions of CO and NMHCs as C_2H_6, C_3H_8, and acetone over the source regions of industry and biomass burning are well simulated. The model well captures the increase in CO and NMHCs in the upper troposphere over the eastern Brazil and the South Atlantic associated with convective transport as observed during the NASA GTE campaign (TRACE-A) [*Fishman et al.*, 1996].

[50] The vertical profiles of NO observed in the northern mid-high latitudes are well simulated by the model. An underestimation of NO by the model is, however, found in the upper troposphere over the biomass-burning regions (TRACE-A) and the tropical regions (PEM-Tropics). We conclude that the underestimation of NO over the biomass-burning regions (Brazil and Africa) is attributed principally to overestimation of PAN formation over these regions (the PAN/NO_x ratio is overestimated by a factor of 2–3 in the upper troposphere over these two regions). This indicates too much production of CH_3COO_2 radical by the chemical scheme for the oxidation of isoprene, terpenes, and the lumped NMHCs species [see *Sudo et al.*, 2002]. The overestimation of CH_3COO_2 and PAN found in the source regions of biomass burning (TRACE-A) could be reduced by heterogeneous loss of peroxy radicals (RO_2) produced by oxidation of NMHCs like isoprene. In the evaluation of the calculated HNO_3, an overestimation (by a factor of ∼2) is found in continental source regions in spite of our ignorance of the heterogeneous conversion of N_2O_5 to HNO_3 on aerosols. This may indicate the need of considering particulate (aerosol) nitrates (NO_3^-) [*Singh et al.*, 1996], or the backward (recycling) conversion of HNO_3 to NO_x on aerosols like soot [e.g., *Hauglustaine et al.*, 1996; *Aumont et al.*, 1999; *Velders and Granier*, 2001].

[51] The calculated global mean OH concentrations lead to a global mean CH_4 lifetime of 7.9 years and a global CH_3CCl_3 lifetime of 4.7 years, in agreement with the estimation by *Prinn et al.* [1995]. The calculated vertical profiles of HO_x species (OH and HO_2) have been compared with the aircraft observations during the PEM-Tropics-B expedition. We found that the calculated OH and HO_2 concentrations are well within the range of the observations. However, we also found that the model tends to overestimate the HO_2/OH ratio (underestimate OH and overestimate HO_2) in the upper troposphere over the central Pacific (Fiji, Tahiti, Christmas Island during PEM-Tropics-B), due to the underestimation of NO in the tropical upper troposphere. The reservoir species for HO_x such as H_2O_2 and CH_3OOH are generally well simulated by the model as well as the precursors of HO_x (CH_2O and acetone). Relatively successful simulation of H_2O_2 may indicate proper representation of the HO_x chemistry and the wet deposition process by the model. However, our evaluation indicates also a slight overestimation of H_2O_2 and CH_3OOH in the upper troposphere in some instances (Figures 26 and 27), as well as the overestimation of CH_2O in the Atlantic and Africa (Figure 21). Such overestimations by the model may coincide with the overestimation of PAN as mentioned above and may be reduced by considering heterogeneous uptake of HO_2 and RO_2 on aerosols in the model.

[52] In the simulation of ozone, the model well captures the seasonal variations of tropospheric ozone in polluted and remote regions. The model also reproduces the vertical profiles of ozone (ozone enhancement of 70–80 ppbv in the free troposphere) over the biomass-burning regions as Brazil, Africa as observed during the aircraft campaign

(TRACE-A). The tropospheric column ozone calculated by the model reaches 45–50 DU over the South Atlantic and Africa in October, in agreement with satellite-based observations [e.g., *Kim et al.*, 1996; *Ziemke et al.*, 1998; *Thompson and Hudson*, 1999]. However, ozone in the upper troposphere in the midlatitudes tends to be overestimated by the model in winter-spring, probably caused by the relatively coarse horizontal resolution of the model adopted in this simulation (T21, approximately 5.6° × 5.6°). The global budget of ozone calculated by the model shows a primary importance of the photochemical production of ozone in the troposphere as previous modeling studies (photochemical production contributes for about 90% to the total source of tropospheric ozone).

[53] In summary, the present version of CHASER is capable of simulating the gas-phase tropospheric chemistry, providing consistent distributions of ozone and OH as well as ozone production and destruction, though some shortcomings in the model. The evaluation of PAN, however, appears to indicate the need of improving the parameterizations for oxidation of NMHCs such as isoprene and a lumped NMHCs species (ONMV) considered in this study. For the next version of the CHASER model, we are implementing heterogeneous reactions of N_2O_5, HNO_3, HO_2, and some peroxy radicals RO_2 on aerosols involving sulfate (SO_4^{2-}) [e.g., *Dentener and Crutzen*, 1993] and soot [*Hauglustaine et al.*, 1996; *Aumont et al.*, 1999; *Velders and Granier*, 2001] for a better representation of the budget of nitrogen species and HO_x, as well as more detailed wet deposition parameterizations. In the future version of the model, aqueous-phase aerosol chemistry (e.g., sea-salt particles) is also being included.

[54] **Acknowledgments.** We are grateful to L.K. Emmons for providing a compiled data set of the NASA GTE aircraft campaigns. We wish to thank M. Capouet for discussing the chemical scheme in the model. We dedicate this study to the memory of Atusi Numaguti. This work has been supported by Center for Climate System Research of the University of Tokyo and Frontier Research System for Global Change. Comments on the manuscript by two anonymous reviewers are greatly appreciated.

References

Arnold, F., V. Burger, B. Droste-Franke, F. Grimm, A. Krieger, J. Schneider, and T. Stilp, Acetone in the upper troposphere and lower stratosphere: Impact on trace gases and aerosols, *Geophys. Res. Lett.*, *24*, 3017–3020, 1997.

Atlas, E., and B. A. Ridley, The Mauna Loa Observatory Photochemistry Experiment: An introduction, *J. Geophys. Res.*, *101*, 14,531–14,541, 1996.

Aumont, B., S. Madronich, M. Ammann, M. Kalberer, U. Baltensperger, D. Hauglustaine, and F. Brocheton, On the NO_2 + soot reaction in the atmosphere, *J. Geophys. Res.*, *104*, 1729–1736, 1999.

Berntsen, T. K., and I. S. A. Isaksen, A global three-dimensional chemical transport model for the troposphere, *J. Geophys. Res.*, *102*, 21,239–21,280, 1997.

Bottenheim, J. W., S. Sirois, K. A. Brice, and A. J. Gallant, Five years of continuous observations of PAN and ozone at a rural location in eastern Canada, *J. Geophys. Res.*, *99*, 5333–5352, 1994.

Brasseur, G. P., D. A. Hauglustaine, S. Walters, and P. J. Rasch, MOZART, a global chemical transport model for ozone and related chemical tracers, 1, Model description, *J. Geophys. Res.*, *103*, 28,265–28,289, 1998.

Cohan, D. S., M. G. Schultz, D. J. Jacob, B. G. Heikes, and D. R. Blake, Convective injection and photochemical decay of peroxides in the tropical upper troposphere: Methyl iodide as a tracer of marine convection, *J. Geophys. Res.*, *104*, 5717–5724, 1999.

Crawford, J., et al., Photochemistry state analysis of the NO_2-NO system based on airborne observations from the western and central North Pacific, *J. Geophys. Res.*, *101*, 2053–2072, 1996.

Crawford, J., et al., An assessment of ozone photochemistry in the extratropical western North Pacific: Impact of continental outflow during the late winter/early spring, *J. Geophys. Res.*, *102*, 28,469–28,487, 1997.

Dentener, F. J., and P. J. Crutzen, Reaction of N_2O_5 on tropospheric aerosols: Impact on the global distributions of NO_x, O_3, and OH, *J. Geophys. Res.*, *98*, 7149–7163, 1993.

Emmons, L. K., D. A. Hauglustaine, J.-F. Müller, M. A. Carroll, G. P. Brasseur, D. Brunner, J. Staehelin, V. Thouret, and A. Marenco, Data composites of airborne observations of tropospheric ozone and its precursors, *J. Geophys. Res.*, *105*, 20,497–20,538, 2000.

Fan, S.-M., D. J. Jacob, D. L. Mauzerall, J. D. Bradshaw, S. T. Sandholm, D. R. Blake, R. W. T. H. B. Singh, G. L. Gregory, and G. W. Sachse, Photochemistry of reactive nitrogen in the sub Arctic troposphere in summer 1990: Observation and modeling, *J. Geophys. Res.*, *99*, 16,867–16,878, 1994.

Fishman, J., and J. C. Larsen, Distribution of total ozone and stratospheric ozone in the tropics: Implications for the distribution of tropospheric ozone, *J. Geophys. Res.*, *92*, 6627–6634, 1987.

Fishman, J., J. M. Hoell Jr., R. D. Bendura, R. J. McNeal Jr., and V. W. J. H. Kirchhoff, The NASA GTE TRACE A Experiment (September–October 1992): Overview, *J. Geophys. Res.*, *101*, 23,865–23,879, 1996.

Folkins, I., R. Chatfield, H. Singh, Y. Chen, and B. Heikes, Ozone production efficiencies of acetone and peroxides in the upper troposphere, *Geophys. Res. Lett.*, *25*, 1305–1308, 1998.

Greenberg, J. P., D. Helmig, and P. Zimmmerman, Seasonal measurements of nonmethane hydrocarbons and carbon monoxide at Mauna Loa Observatory during the Mauna Loa Observatory, *J. Geophys. Res.*, *101*, 14,581–14,598, 1996.

Gregory, G. L., H. E. Fuelberg, S. P. Longmore, B. E. Anderson, J. E. Collins, and D. R. Blake, Chemical characteristics of tropospheric air over the tropical South Atlantic Ocean: Relationship to trajectory history, *J. Geophys. Res.*, *101*, 23,957–23,972, 1996.

Hauglustaine, D. A., B. A. Ridley, S. Solomon, P. G. Hess, and S. Madronich, HNO_3/NO_x ratio in the remote troposphere during MLOPEX2: Evidence for nitric acid reduction on carbonaceous aerosols?, *Geophys. Res. Lett.*, *23*, 2609–2612, 1996.

Hauglustaine, D. A., G. P. Brasseur, S. Walters, P. J. Rasch, J.-F. Müller, L. K. Emmons, and M. A. Carroll, MOZART, a global chemical transport model for ozone and related chemical tracers, 2, Model results and evaluation, *J. Geophys. Res.*, *103*, 28,291–28,335, 1998.

Heikes, B., et al., Ozone, hydroperoxides, oxides of nitrogen, and hydrocarbon budget in the marine boundary layer over the South Atlantic, *J. Geophys. Res.*, *101*, 24,221–24,234, 1996.

Horowitz, L. W., J. Liang, G. M. Gardner, and D. J. Jacob, Export of reactive nitrogen from North America during summertime: Sensitivity to hydrocarbon chemistry, *J. Geophys. Res.*, *103*, 13,451–13,476, 1998.

Houweling, S., F. Dentener, and J. Lelieveld, Impact of nonmethane hydrocarbon compounds on tropospheric photochemistry, *J. Geophys. Res.*, *103*, 10,673–10,696, 1998.

Jacob, D. J., Heterogeneous chemistry and tropospheric ozone, *Atmos. Environ.*, *34*, 2131–2159, 2000.

Jaeglé, L., et al., Observed OH and HO_2 in the upper troposphere suggest a major source from convective injection of peroxides, *Geophys. Res. Lett.*, *24*, 3181–3184, 1997.

Jenkin, M. E., S. M. Saunders, and M. J. Pilling, The tropospheric degradation of volatile organic compounds: A protocol for mechanism development, *Atmos. Environ.*, *31*, 81–104, 1997.

Kim, J. H., R. D. Hudson, and A. M. Thompson, A new method of deriving time-averaged tropospheric column ozone over the tropics using total ozone mapping spectrometer (TOMS) radiances: Intercomparison and analysis using TRACE-A data, *J. Geophys. Res.*, *101*, 24,317–24,330, 1996.

Kirchhoff, V. W. J. H., A. W. Setzer, and M. C. Pereira, Biomass burning in Amazonia: Seasonal effects on atmospheric, *Geophys. Res. Lett.*, *16*, 469–472, 1989.

Lawrence, M. G., P. J. Crutzen, P. J. Rasch, B. E. Eaton, and N. M. Mahowald, A model for studies of tropospheric photochemistry: Description, global distributions, and evaluation, *J. Geophys. Res.*, *104*, 26,245–26,277, 1999.

Lelieveld, J., and R. van Dorland, Ozone chemistry changes in the troposphere and consequent radiative forcing of climate, in *Atmospheric Ozone As a Climate Gas*, edited by W.-C. Wang and I. S. A. Isaksen, pp. 227–258, Springer-Verlag, New York, 1995.

Levy, H., II, Normal atmosphere: Large radical and formaldehyde concentrations predicted, *Science*, *173*, 141–143, 1971.

Logan, J. A., An analysis of ozonesonde data for the troposphere: Recommendations for testing 3-D models and development of a gridded climatology for tropospheric ozone, *J. Geophys. Res.*, *104*, 16,115–16,149, 1999.

Mari, C., et al., Sources of upper tropospheric HOx over the South Pacific

Convergence Zone: A case study, *J. Geophys. Res.*, *107*, doi:10.1029/2001JD001466, in press, 2002.

Martin, R. S., H. Westberg, E. Allwine, L. Ashman, J. C. Farmer, and B. Lamb, Measurement of isoprene and its atmospheric oxidation products in a central Pennsylvania deciduous forest, *J. Atmos. Chem.*, *13*, 1–32, 1991.

McKeen, S. A., et al., The photochemistry of acetone in the upper troposphere: A source of odd-hydrogen radicals, *Geophys. Res. Lett.*, *24*, 3177–3180, 1997.

Montzka, S. A., M. Trainer, W. M. Angevine, and F. C. Fehsenfeld, Measurements of 3-methyl furan, methyl vinyl ketone, and methacrolein at a rural forested site in the southeastern United States, *J. Geophys. Res.*, *100*, 11,393–11,401, 1995.

Moxim, W. J., H. Levy II, and P. S. Kashibhatla, Simulated global tropospheric PAN: Its transport and impact on NO_x, *J. Geophys. Res.*, *101*, 12,621–12,638, 1996.

Müller, J.-F., and G. P. Brasseur, IMAGES: A three-dimensional chemical transport model of the global troposphere, *J. Geophys. Res.*, *100*, 16,445–16,490, 1995.

Müller, J.-F., and G. P. Brasseur, Sources of upper tropospheric HO_x: A three-dimensional study, *J. Geophys. Res.*, *104*, 1705–1715, 1999.

Novelli, P. C., L. P. Steele, and P. P. Tans, Mixing ratios of carbon monoxide in the troposphere, *J. Geophys. Res.*, *97*, 20,731–20,750, 1992.

Novelli, P. C., J. E. Collins Jr., R. C. Myers, G. W. Sachsem, and H. E. Scheel, Reevaluation of the NOAA/CMDL carbon monoxide reference scale and comparisons to CO reference gases at NASA-Langley and the Fraunhofer Institute, *J. Geophys. Res.*, *99*, 12,833–12,839, 1994.

Numaguti, A., Dynamics and energy balance of the Hadley circulation and the tropical precipitation zones: Significance of the distribution of evaporation, *J. Atmos. Sci.*, *50*, 1874–1887, 1993.

Numaguti, A., M. Takahashi, T. Nakajima, and A. Sumi, Development of an atmospheric general circulation model, in *Reports of a New Program for Creative Basic Research Studies, Studies of Global Environment Change With Special Reference to Asia and Pacific Regions*, *Rep., I-3*, pp. 1–27, CCSR, Tokyo, 1995.

Oltmans, S. J., and H. Levy II, Surface ozone measurements from a global network, *Atmos. Environ.*, *28*, 9–24, 1994.

Parrish, D. D., et al., The total reactive oxidized nitrogen levels and the partitioning between the individual species at six rural sites in eastern North America, *J. Geophys. Res.*, *98*, 2927–2939, 1993.

Pöschl, U., R. von Kuhlmann, N. Poisson, and P. J. Crutzen, Development and intercomparison of condensed isoprene oxidation mechanisms for global atmospheric modeling, *J. Atmos. Chem.*, *37*, 29–52, 2000.

Prinn, R. G., R. F. Weiss, B. R. Miller, J. Huang, F. N. Alyea, D. M. Cunnold, P. J. Fraser, D. E. Hartley, and P. G. Simmonds, Atmospheric trends and lifetime of CH_3CCl_3 and global OH concentrations, *Science*, *269*, 187–192, 1995.

Ridley, B. A., and E. Robinson, The Mauna Loa Observatory Photochemistry Experiment, *J. Geophys. Res.*, *97*, 10,285–10,290, 1992.

Ridley, B. A., et al., Measurements of NO_x and PAN and estimates of O_3 production over the seasons during Mauna Loa Observatory Photochemistry Experiment 2, *J. Geophys. Res.*, *103*, 8323–8339, 1998.

Roelofs, G.-J., and J. Lelieveld, Distribution and budget of O_3 in the troposphere calculated with a chemistry general circulation model, *J. Geophys. Res.*, *100*, 20,983–20,998, 1995.

Roelofs, G.-J., and J. Lelieveld, Tropospheric ozone simulation with a chemistry-general circulation model: Influence of higher hydrocarbon chemistry, *J. Geophys. Res.*, *105*, 22,697–22,712, 2000.

Roelofs, G.-J., J. Lelieveld, and R. van Dorland, A three-dimensional chemistry/general circulation model simulation of anthropogenically derived ozone in the troposphere and its radiative climate forcing, *J. Geophys. Res.*, *102*, 23,389–23,401, 1997.

Schultz, M., et al., On the origin of tropospheric ozone and NO_x over the tropical South Pacific, *J. Geophys. Res.*, *104*, 5829–5843, 1999.

Singh, H. B., M. Kanakidou, P. J. Crutzen, and D. J. Jacob, High concentrations and photochemical fate of oxygenated hydrocarbons in the global troposphere, *Nature*, *378*, 50–54, 1995.

Singh, H. B., et al., Reactive nitrogen and ozone over the western Pacific: Distribution, partitioning, and sources, *J. Geophys. Res.*, *101*, 1793–1808, 1996.

Solberg, S., C. Dye, N. Schmidbauer, A. Herzog, and R. Gehrig, Carbonyls and nonmethane hydrocarbons at rural European sites from the Mediterranean to the Arctic, *J. Atmos. Chem.*, *25*, 33–66, 1996.

Spivakovsky, C. M., et al., Three-dimensional climatological distribution of tropospheric OH: Update and evaluation, *J. Geophys. Res.*, *105*, 8931–8980, 2000.

Sudo, K., and M. Takahashi, Simulation of tropospheric ozone changes during 1997–1998 El Niño: Meteorological impact on tropospheric photochemistry, *Geophys. Res. Lett.*, *28*, 4091–4094, 2001.

Sudo, K., M. Takahashi, J. Kurokawa, and H. Akimoto, CHASER: A global chemical model of the troposphere, 1, Model description, *J. Geophys. Res.*, *107*, doi:10.1029/2001JD001113, in press, 2002.

Talbot, R. W., et al., Chemical characteristics of continental outflow over the tropical South Atlantic Ocean from Brazil and Africa, *J. Geophys. Res.*, *101*, 24,287–24,202, 1996.

Thompson, A. M., The oxidizing capacity of the Earth's atmosphere: Probable past and future changes, *Science*, *256*, 1157–1165, 1992.

Thompson, A. M., and R. D. Hudson, Tropical tropospheric ozone (TTO) maps from Nimbus 7 and Earth Probe TOMS by the modified-residual method: Evaluation with sondes, ENSO signals, and trends from Atlantic regional time series, *J. Geophys. Res.*, *104*, 26,961–26,975, 1999.

Thompson, A. M., K. E. Pickering, D. P. McNamara, M. R. Schoeberl, R. D. Hudson, J. H. Kim, E. V. Browell, V. W. J. H. Kirchhoff, and D. Nganga, Where did tropospheric ozone over southern Africa and the tropical Atlantic come from in October 1992? Insights from TOMS, GTE/TRACE-A and SAFARI-92, *J. Geophys. Res.*, *101*, 24,251–24,278, 1996.

Velders, J. M., and C. Granier, Sensitivity of washout on HNO_3/NO_x ratio in atmospheric chemistry transport models, *J. Geophys. Res.*, *106*, 3125–3132, 2001.

Walcek, C. J., H.-H. Yuan, and W. R. Stockwell, The influence of aqueous-phase chemical reactions on ozone formation in polluted and nonpolluted cloud, *Atmos. Environ.*, *31*, 1221–1237, 1997.

Wang, Y., D. J. Jacob, and J. A. Logan, Global simulation of tropospheric O_3-NO_x-hydrocarbon chemistry, 1, Model formulation, *J. Geophys. Res.*, *103*, 10,713–10,725, 1998a.

Wang, Y., J. A. Logan, and D. J. Jacob, Global simulation of tropospheric O_3-NO_x-hydrocarbon chemistry, 2, Model evaluation and global ozone budget, *J. Geophys. Res.*, *103*, 10,727–10,755, 1998b.

Wang, Y., D. J. Jacob, and J. A. Logan, Global simulation of tropospheric O_3-NO_x-hydrocarbon chemistry, 3, origin of tropospheric ozone and effects of nonmethane hydrocarbons, *J. Geophys. Res.*, *103*, 10,757–10,767, 1998c.

Wennberg, P. O., et al., Hydrogen radicals, nitrogen radicals and the production of O_3 in the upper troposphere, *Science*, *279*, 49–53, 1998.

Ziemke, J. R., S. Chandra, and P. K. Bhartia, Two new methods for deriving tropospheric column ozone from TOMS measurements: Assimilated UARS MLS/HALOE and convective-cloud differential techniques, *J. Geophys. Res.*, *103*, 22,115–22,127, 1998.

Zimmerman, P. R., J. P. Greenberg, and C. E. Westberg, Measurements of atmospheric hydrocarbons and biogenic emission fluxes on the Amazon boundary layer, *J. Geophys. Res.*, *93*, 1407–1416, 1988.

H. Akimoto, Institute for Global Change Research, Yokohama Campus, 3173-25 Showa-machi, Kanazawa-ku, Yokohama, Kanagawa, 236-0001, Japan. (akimoto@frontier.esto.or.jp)

K. Sudo and M. Takahashi, Center for Climate System Research, University of Tokyo, 4-6-1, Komaba, Meguro-ku, Tokyo, 153-8904, Japan. (kengo@ccsr.u-tokyo.ac.jp; masaaki@ccsr.u-tokyo.ac.jp)